

COMPUTATIONAL STUDY OF VORTEX INDUCED
VIBRATION PERFORMANCE WITH COUPLED
BLUFF SPLITTER BODY AND ELASTIC PLATE
MODEL

CHIN WEI KEN

DISSERTATION SUBMITTED IN FULFILMENT
OF THE REQUIREMENTS FOR THE DEGREE OF
MASTER OF ENGINEERING SCIENCE

MECHANICAL ENGINEERING
FACULTY OF ENGINEERING
UNIVERSITY OF MALAYA
KUALA LUMPUR

2018

UNIVERSITI MALAYA

PERAKUAN KEASLIAN PENULISAN

Nama: CHIN WEI KEN

No. Pendaftaran/Matrik: KGA 140061

Nama Ijazah: MASTER OF ENGINEERING SCIENCE

Tajuk Kertas Projek/Laporan Penyelidikan/Disertasi/Tesis("Hasil Kerja ini")

COMPUTATIONAL STUDY OF VORTEX INDUCED VIBRATION PERFORMANCE WITH COUPLED
BLUFF SPLITTER BODY AND ELASTIC PLATE MODEL

Bidang Penyelidikan: VIBRATION

Saya dengan sesungguhnya dan sebenarnya mengaku bahawa:

- (1) Saya adalah satu-satunya pengarang/penulis Hasil Kerja ini;
- (2) Hasil Kerja ini adalah asli;
- (3) Apa-apa penggunaan mana-mana hasil kerja yang mengandungi hakcipta telah dilakukan secara urusan yang wajar dan bagi maksud yang dibenarkan dan apa-apa petikan, ekstrak, rujukan atau pengeluaran semula daripada atau kepada mana-mana hasil kerja yang mengandungi hakcipta telah dinyatakan dengan sejelasnya dan secukupnya dan satu pengiktirafan tajuk hasil kerja tersebut dan pengarang/penulisnya telah dilakukan di dalam Hasil Kerja ini;
- (4) Saya tidak mempunyai apa-apa pengetahuan sebenar atau patut semunasabahnya tahu bahawa penghasilan Hasil Kerja ini melanggar suatu hak cipta hasil kerja yang lain
- (5) Saya dengan ini menyerahkan kesemua dan tiap-tiap hak yang terkandung di dalam hakcipta Hasil Kerja ini kepada Universiti Malaya ("UM") yang seterusnya mula dari sekarang adalah tuan punya kepada hakcipta di dalam Hasil Kerja ini dan apa-apa pengeluaran semula atau penggunaan dalam apa jua bentuk atau dengan apa jua cara sekalipun adalah dilarang tanpa terlebih dahulu mendapat kebenaran bertulis dari UM;
- (6) Saya sedar sepenuhnya sekiranya dalam masa penghasilan Hasil Kerja ini saya telah melanggar suatu hakcipta hasil kerja yang lain sama ada dengan niat atau sebaliknya, saya boleh dikenakan tindakan undang-undang atau apa-apa tindakan lain sebagainya yang diputuskan oleh UM.

Tandatangan Calon

Tarikh:

Diperbuat dan sesungguhnya diakui di hadapan

Tandatangan Saksi

Tarikh:

Nama:

Jawatan:

UNIVERSITI MALAYA

ORIGINAL LITERARY WORK DECLARATION

Name of Candidate: CHIN WEI KEN

Registration/Matric No: KGA 140061

Name of Degree: MASTER OF ENGINEERING SCIENCE

Title of Project Paper/Research Report/Dissertation/Thesis ("this Work")

COMPUTATIONAL STUDY OF VORTEX INDUCED VIBRATION PERFORMANCE WITH COUPLED
BLUFF SPLITTER BODY AND ELASTIC PLATE MODEL

Field of Study: VIBRATION

I do solemnly sincerely declare that:

- (1) I am the sole author/writer of this work;
- (2) This Work is original;
- (3) Any use of any work in which copyright exists was done by way of fair dealing and for permitted purposes and any excerpt or extract form, or reference to or reproduction of any copyright work has been disclosed expressly and sufficiently and the title of the Work and its authorship have been acknowledged in this Work;
- (4) I do not have any actual knowledge nor do I ought reasonably to know that the making of this work constitutes an infringement of any copyright work;
- (5) I hereby assign all and every rights in the copyright to this Work to the University of Malaya ("UM"), who henceforth shall be owner of the copyright in this Work and that any reproduction or use in any form or by any means whatsoever is prohibited without the written consent of UM having been first had and obtained;
- (6) I am fully aware that if in the course of making this Work I have infringed any copyright whether intentionally or otherwise, I may be subjected to legal action or any other action as may be determined by UM.

Candidate's Signature:

Date:

Subscribed and solemnly declared before,

Witness's Signature

Date:

Name:

Designation:

ABSTRACT

Vortex-induced vibration (VIV) had been known as an engineering problem that causes damages and destructions to structures, such as buildings, bridges, stacks and pipelines in the past few decades. With the rapid development of piezoelectric harvester in recent years, vortex induced vibration had been the staple of research as a new form of energy harvesting. This research investigates and enhances the performance of a vortex induced vibration harvester in three aspects, i.e. change in wind speed, difference in structural aspect ratio and difference in bluff splitter body design, in order to. All of the studies were conducted with a T-shaped coupled bluff splitter body and elastic plate model through Fluid Structure Interaction (FSI) Method.

In the first part of the first objective, a coupled thin rectangular bluff splitter body and PVEH plate undergoes different wind speeds at 7 m/s, 18 m/s, 19 m/s, 20 m/s, 22 m/s and 25 m/s. Results showed that at 19 m/s flow produced highest vibrational amplitude of 2 mm because the vortex frequency of 75.758 Hz resonates with the model's natural frequency of 76.955 Hz. In the second part, a coupled 1 cm cube bluff splitter body and 4 cm long elastic plate is tested with wind speed range from 0.3 m/s, 0.4 m/s, 0.513 m/s, 0.6 m/s, 0.7 m/s, 1.0 m/s dan 1.5 m/s. Results showed that 0.7 m/s with closeness of vortex frequency 3.94 Hz to the structural natural frequency of 3.087 Hz together with decent fluctuating lift force value is able to generate largest displacement value of 0.0149 m.

Second objective is aimed at finding out the effects of bluff splitter body width to elastic plate length ratio or known as aspect ratio of the model on VIV performance. The first part of this section involves a 0.04 m elastic plate coupled with bluff splitter body of 0.01 m length and different width including 0.005 m, 0.01 m, 0.02 m, 0.03 m, 0.04 m, 0.06 m and 0.08 m. The second part involves coupled 0.03 m wide bluff splitter

body and different elastic plate length 0.02 m, 0.03 m, 0.04 m, 0.05 m, and 0.06 m. Under 0.513 m/s wind speed, the results from both sections showed that vibration is amplified to the amplitude of 0.0153 m with a coupled 0.03m wide bluff splitter body and 0.04 m elastic plate through closeness of vortex frequency of 3.182 Hz to the structures natural frequency of 3.087 Hz.

The last objective investigates the enhancement of VIV through bluff splitter body design. In the first part, different shapes of bluff splitter body including circular, rectangular, triangle, trapezoidal, curve, diffuser and semicircle with concave or convex arrangement were tested. It is proven concave shape is able to generate higher lift force and vortex frequency compared to convex shape. However, rectangular together with convex shaped trapezoidal and semicircle shape which generate closer vortex frequency to the structures' natural frequency produced higher tip displacement compared to other shapes. The second part involves the change of edge angles between 34.22°, 45°, 60°, 75°, 90°, 120°, and 146.31°. It is shown that trapezoidal shape of 60° edge angle with the closest vortex frequency of 3.03 Hz compared to structure's natural frequency is the best performing shape, inducing 0.0159 m displacement value 4.605% higher than the rectangular bluff splitter body above.

In conclusion, these overall results displayed the importance of matching vortex frequency to the natural frequency of the structure undergoing VIV in the effort of enhancing the performance. This thesis will significantly improve the knowledge in enhancing VIV performance and further encourage VIV harvester development.

ABSTRAK

Getaran disebabkan vortex (VIV) sudah biasa dikenali sebagai satu masalah kejuruteraan yang banyak membawa kerosakkan dan kemusnahan kepada struktur seperti bangunan, jambatan, cerobong, laluan paip dan lain-lain sejak beberapa dekad dahulu. Kebelakangan tahun dengan kemajuan teknologi penuai tenaga piezo, VIV menjadi fokus penyelidikan sebagai sejenis penuai tenaga. Penyelidikan ini dibahagikan kepada 3 seksyen iaitu mengubah kelajuan angin, nisbah aspek struktur dan reka bentuk badan membelah angin untuk menyelidik dan meningkatkan prestasi penuai tenaga VIV. Kesemua penyelidikan dikendalikan dengan struktur berbentuk T yang merupakan kombinasi badan membelah angin dan plat anjal melalui kaedah Fluid Structure Interaction (FSI).

Dalam bahagian 1 objektif 1, struktur kombinasi badan membelah angin segi empat dan plat PVEH diuji dengan kelajuan angin berbeza dengan nilai 7 m/s, 18 m/s, 19 m/s, 20 m/s, 22 m/s, dan 25 m/s. Keputusan menunjukkan 19 m/s menghasilkan amplitud getaran tertinggi dengan 2 mm, sebab kelajuan tersebut menghasilkan frekuensi vortex 75.758 Hz yang dekat dengan frekuensi semulajadi struktur 76.955 Hz. Dalam bahagian 2, kombinasi 0.01 m badan membelah angin segi empat tepat dan plat anjal 0.04 m diuji dengan kelajuan angin 0.3 m/s, 0.4 m/s, 0.513 m/s, 0.6 m/s, 0.7 m/s, 1.0 m/s dan 1.5 m/s. Keputusan menunjukkan 0.7 m/s menghasilkan amplitud getaran paling tinggi kerana mempunyai kelebihan kedekatan nilai frekuensi vortex 3.74 Hz dengan frekuensi semulajadi struktur nilai 3.087 Hz dan juga daya angkat yang baik.

Objektif 2 bertujuan untuk mengetahui kesan nisbah aspek struktur iaitu nisbah kelebaran badan membelah angin dan kepanjangan plat anjal kepada prestasi VIV. Bahagian 1 melibatkan gabungan badan membelah angin berbeza kelebaran bernilai 0.005 m, 0.01 m, 0.02 m, 0.03 m, 0.04 m, 0.06 m dan 0.08m dan plat anjal 0.04 m.

Bahagian 2 terlibat gabungan badan membelah angin 0.03 m lebar dan plat anjal dengan kepanjangan berbeza bernilai 0.02 m, 0.03 m, 0.04 m, 0.05 m, and 0.06 m. Dengan kelajuan angin 0.513 m/s, keputusan menunjukkan bahawa amplitud tertinggi merupakan 0.0153 m daripada struktur gabungan badan membelah angin 0.03 m lebar dan plat anjal 0.04 m panjang. Kesan daripada kedekatan frekuensi vortex iaitu 3.182 Hz ke frekuensi semulajadi struktur 3.087 Hz adalah sebab utama penghasilan amplitud VIV yang tinggi.

Objektif terakhir menyelidik penambahbaikan prestasi VIV melalui rekabentuk badan membelah angin. Bahagian 1 menguji kesan badan membelah angin berbentuk bulat, segi empat, segi tiga, trapezoid, separuh bulat, lengkungan, penyebar dalam konfigurasi concave dan convex. Didapati daripada keputusan bahawa bentuk concave mengenakan daya angkat dan frekuensi vortex yang tinggi. Walau bagaimanapun, dengan kedekatan frekuensi vortex bernilai 3.03 Hz dengan frekuensi semulajadi struktur bernilai 3.087 Hz, bentuk segi empat, segi tiga convex dan trapezoid convex menandakan amplitud anjakan paling tinggi. Bahagian 2 melibatkan perubahan sudut pinggir dengan nilai 34.22° , 45° , 60° , 75° , 90° , 120° , dan 146.31° . Trapezoid bersudut 60° adalah bentuk yang berprestasi paling bagus dengan 0.0159 m amplitud anjakan atau 4.605 % tinggi daripada segi empat, ini disebabkan kedekatan frekuensi vortex dengan frekuensi struktur.

Kesimpulannya, penyelidikan ini mempersembahkan faktor paling penting untuk menandakan amplitud anjakan VIV yang efektif adalah menandingi frekuensi vortex dengan frekuensi semulajadi sebuah struktur. Thesis ini akan menambah ilmu dalam bidang VIV ini dan juga menggalakkan kemajuann penuai tenaga vortex.

ACKNOWLEDGEMENT

In order to complete this postgraduate study, I had received many help from different parties of people. Hereby, I would like to take this opportunity to express the heartfelt gratitude towards the people whom had given a helping hand along the journey in completing this research report.

First and foremost, I would like to express my sincere appreciation towards my supervisor Dr. Ong Zhi Chao and Dr. Chong Wen Tong from University of Malaya for their continuous guidance and support along this time of research. The patience, motivation and also immense knowledge given by them had been the main cause that this thesis and my post-graduate study is able to be completed. I could not have imagine doing postgraduate studies with any other supervisors.

I would also like to take this opportunity to acknowledge Dr. Khoo Shin Yee and Mr. Kong Keen Kuan from University of Malaya. Their knowledge in this field had taught me a lot from basic knowledge to widening my perspective toward the field of study.

I would also thank my colleagues and labmates. The discussions and all the working moments had been unforgettable. I would also like to acknowledge the financial support and advice given by Postgraduate Research Grant (PG005-2015A), University of Malaya Grant Scheme (RP022D-13AET), and High Impact Research Grant under UM.C/HIR/MOHE/ENG/06 (D000006-16001).

Last but not least I would like to express my profound gratitude towards my parents, girlfriend and friends for giving me unlimited amounts of support and encouragement throughout my years of study, without them it is impossible for me to make it this far. Finally to all, Thank You once again.

TABLE OF CONTENTS

ABSTRACT.....	iv
ABSTRAK.....	vi
ACKNOWLEDGEMENT	viii
TABLE OF CONTENTS	ix
LIST OF FIGURES	xv
LIST OF TABLES	xxi
LIST OF APPENDIX	xxii
NOMENCLATURE.....	xxiii
CHAPTER 1: INTRODUCTION	1
1.1 Energy rating	1
1.2 Vortex-Induced Vibration Overview.....	3
1.3 Problem Statement	4
1.4 Objectives	7
1.5 Research Flow	7
1.6 Organization of Thesis	9
CHAPTER 2: LITERATURE REVIEW	10
2.1 Vortex Flow Formation	10
2.2 Vortex Induced Vibration.....	11
2.2.1 Critical Velocity	12
2.2.2 Strouhal Number, St	13
2.2.3 Scruton Number, Sc	13

2.2.4	Reynolds number, Re	14
2.3	Vortex Induced Vibration in Energy Harvesting.....	15
2.3.1	Cylindrical Cross-Flow Vortex induced Vibration.....	16
2.3.2	Tandem Cylinder Configuration Vortex Induced Vibration.....	18
2.3.3	Multi-Cylinder Vortex Induced Vibration	20
2.3.4	Cantilever Configuration with Bluff Splitter Body.....	21
2.3.5	Summary of Past Research.....	23
2.4	Piezoelectric Harvester Design.....	24
2.5	Structural Mechanics	25
2.6	Fluid Mechanics	26
2.6.1	Fluid Forces over Bluff Splitter Body.....	27
2.6.2	The Navier-Stokes Equation	28
2.7	Numerical Simulation.....	30
2.7.1	Computational Fluid Dynamics Methods Approach.....	31
2.7.2	Grid Generation/Meshing.....	32
2.7.3	Turbulent CFD Calculations	33
2.7.4	Turbulence Model	34
2.7.4.1	Reynolds Averaging of Navier-Stokes Equations (RANS).....	35
2.7.4.2	Large Eddy Simulation (LES)	36
2.7.4.3	Algebraic Model	37
2.7.4.4	One Equation Turbulence Model.....	37
2.7.4.5	$k-\varepsilon$ Turbulence Model	38

2.7.4.6	Standard $k-\omega$ Turbulence Model.....	39
2.7.4.7	SST $k-\omega$ Turbulence Model.....	39
2.7.4.8	Reynolds Stress Turbulence Model	40
2.7.5	Fluid-Structure Interaction	42
CHAPTER 3: METHODOLOGY		44
3.1	Introduction	44
3.2	Methodology Overview.....	45
3.2.1	CAD Modelling.....	45
3.2.2	Meshing.....	46
3.2.3	Fluid-Structure Interaction Analysis.....	46
3.3	CAD Model Design of Structural Model and Domain.....	47
3.3.1	Coupled Thin Bluff Splitter Body and PVEH plate model.....	47
3.3.2	Coupled Bluff Splitter Body and Elastic Plate Model	49
3.3.2.1	Coupled Bluff Splitter Body and Elastic Plate Aspect Ratio Modifications	50
3.3.2.2	Bluff Splitter Body Design Modifications.....	52
3.3.2.3	Fluid Domain Design.....	57
3.4	Meshing Parameters	58
3.4.1	Coupled Bluff Splitter Body and PVEH Plate	59
3.4.1.1	Structural Model Mesh	59
3.4.1.2	Computational Fluid Domain Mesh	59
3.4.2	Coupled Bluff Splitter Body and Elastic Plate Model	61
3.4.2.1	Structural Model mesh.....	61

3.4.2.2	Computational Fluid Domain Mesh	63
3.5	Fluid-Structure Interaction Simulation Settings	66
3.5.1	Coupled Bluff Splitter Body and PVEH Plate Model.....	67
3.5.2	Coupled Bluff Splitter Body and Elastic Plate Model	68
3.6	Modal Analysis and Structural Validation	70
CHAPTER 4: RESULTS AND DISCUSSION		73
4.1	Effect of Flow Speed on Vortex Induced Vibration Enhancement.....	73
4.1.1	Coupled PVEH Plate and Thin Bluff Splitter Body Model	73
4.1.1.1	Grid Independence Study.....	73
4.1.1.2	Structural Model Validation	74
4.1.1.3	Vortex Formation with Different Wind Speed (PVEH Plate)	76
4.1.1.4	Fluctuating Lift Force with Different Wind Speed (PVEH Plate).....	78
4.1.1.5	Vortex Induced Vibration with Different Wind Speed (PVEH Plate).....	80
4.1.2	Coupled Elastic Plate and Bluff Splitter Body Model	83
4.1.2.1	Grid Independence Study.....	83
4.1.2.2	Numerical Model Validation	84
4.1.2.3	Structural Modal Analysis	85
4.1.2.4	Vortex Formation with Different Wind Speed (Elastic Plate).....	86
4.1.2.5	Fluctuating Lift with Different Wind Speed (Elastic Plate)	88
4.1.2.6	Vortex Induced Vibration with Different Wind Speed (Elastic Plate).....	90
4.1.3	Summary (Wind Speed Variance)	93

4.2	Effect of Coupled Elastic Plate and Bluff Splitter Body Aspect Ratio on Vortex Induced Vibration Enhancement	93
4.2.1	Bluff Splitter Body Width Difference	93
4.2.1.1	Modal Characteristic Analysis of Model with Different Bluff Splitter Body Size	94
4.2.1.2	Vortex Street Formation of Different Bluff Splitter Body Sizes	94
4.2.1.3	Fluctuating Lift of Different Bluff Splitter Body Sizes	97
4.2.1.4	Vortex Induced Vibrations of Different Bluff Body Sizes	99
4.2.2	Elastic Plate Length Difference	102
4.2.2.1	Structural Modal Analysis	102
4.2.2.2	Vortex Formation with Different Elastic Plate Length	103
4.2.2.3	Fluctuating Lift Force with Different Elastic Plate Length	105
4.2.2.4	Vortex Induced Vibration with Different Elastic Plate Length	106
4.2.3	Summary (Aspect Ratio Difference)	109
4.3	Effect of Bluff Splitter Body Design Modification on Vortex Induced Vibration Enhancement	110
4.3.1	Bluff Splitter Body Cross-Sectional Shapes Difference	110
4.3.1.1	Structural Modal Analysis	110
4.3.1.2	Vortex Formation Length of Different Bluff Splitter Body Shapes	110
4.3.1.3	Fluctuating Lift Force of Different Bluff Splitter Body Shapes	114
4.3.1.4	Vortex Induced Vibration of Different Bluff Splitter Body Shapes	116
4.3.2	Bluff Splitter Body Edge Angle Difference	120

4.3.2.1	Vortex Formation of Different Angle of Trapezoidal Bluff Splitter Body.....	120
4.3.2.2	Fluctuating Lift Force of Different Angles of Trapezoidal Bluff Splitter Body	122
4.3.2.3	Vortex Induced Vibration of Different Edge Angles of Bluff Splitter Body.....	124
4.3.3	Summary (Bluff Splitter Body Design)	127
CHAPTER 5: CONCLUSION.....		128
5.1	Conclusion.....	128
5.2	Future Recommendations.....	130
REFERENCES.....		131
APPENDIX A.....		139
APPENDIX B.....		140
APPENDIX C.....		141
APPENDIX D.....		148

LIST OF FIGURES

Figure 1.1: Research Flow Chart	8
Figure 2.1: Different Flow Undergoes Separation When Encountering Bluff Splitter Body (Source: https://www.grc.nasa.gov/)	11
Figure 2.2: Vortex (Separation Region) and Wake (Source: GDTEch Belgium)	11
Figure 2.3: Von Karman Vortex Street behind Bluff Splitter Body When Flow Passes Through (Source: web.mit.edu)	12
Figure 2.4: Vortex Flow Pattern under Different Reynolds Number Flow. (Source: Thermopedia)	15
Figure 2.5: Square Arrangement of VIV Harvester Cylinder (Source: Zhaolong Han et al.).....	21
Figure 2.6: Force Components Acting on a Body When Flow Passes Through (Source: www.aerospaceweb.org)	27
Figure 2.7: Schematic Flow Diagram of 1-way and 2-way FSI Coupling	43
Figure 3.1: CAD Design of Bluff Splitter Body-PVEH Plate Coupled Model (All units shown in mm).....	47
Figure 3.2: Computational Domain Size (PVEH Model Coupled with Bluff Splitter Body).....	48
Figure 3.3: Side View Illustration of Fluid Domain Dimensions and Model Placement	49
Figure 3.4: Coupled Bluff Splitter Body and Elastic Plate Model by Dettmer (All units shown in mm).....	50
Figure 3.5: Coupled Bluff Splitter Body and Elastic Plate Model with Different Bluff Splitter Body Width (a) 0.005m (b) 0.02m (c) 0.03m (d) 0.04m (e) 0.06m (f) 0.08m (All units shown in mm).....	51
Figure 3.6: Coupled Bluff Splitter Body and Elastic Plate Model with Different Elastic Plate Length (a) 0.02m (b) 0.03m (c) 0.05m (d) 0.06m (All units shown in mm)	52

Figure 3.7: Bluff Splitter Body's Trailing Edge and Leading Edge.....	54
Figure 3.8: Coupled Bluff Splitter Body and Elastic Plate Model with Different Bluff Splitter Body Shape (a) Curve I (b) Curve II (c) Diffuser I (d) Diffuser II (e) Semicircle I (f) Semicircle II (g) Trapezoidal I (h) Trapezoidal II (i) Triangle I (j) Triangle II (k) Circular (All units shown in mm)	56
Figure 3.9: Coupled Bluff Splitter Body and Elastic Plate Model with Different Side Edge Angle of (a) 45° and (b) 60° (All units shown in mm).....	57
Figure 3.10: CFD Fluid Domain for all Coupled Bluff Splitter Body and Elastic Plate Model	58
Figure 3.11: Fluid Domain Dimension Illustration (D = Bluff Body Width & L = Elastic Plate Length).....	58
Figure 3.12: 0.001m Coupled Bluff Splitter Body and PVEH Plate Model Structured Prism Mesh	59
Figure 3.13: 0.001m to 0.2m size CFD Domain Mesh of Coupled Bluff Splitter Body and PVEH Plate Model	60
Figure 3.14: Magnified CFD Domain Mesh of Coupled Bluff Splitter Body and PVEH Plate Model with Display of 10 Layer Inflation Layer	61
Figure 3.15: 0.001m Coupled Bluff Splitter Body and Elastic Plate Model Structural Mesh.....	62
Figure 3.16: 0.00025m to 0.005m size CFD Domain Mesh of Coupled Bluff Splitter Body and PVEH Plate Model	65
Figure 3.17: 0.00025m Mesh Size for Contact Wall Surface of Coupled Bluff Splitter Body and Elastic Plate Model in CFD Domain	65
Figure 3.18: Magnified CFD Domain Mesh of Coupled Bluff Splitter Body and PVEH Plate Model with Display of 10 Layer Inflation Layer	66
Figure 3.19: Sweep Method Layers across Thickness of Fluid Domain	66

Figure 3.20: Simulation Setup of Bluff Splitter Body-PVEH Plate Coupled Model in 3D Fluid Domain with Wind Direction towards Model ($D = 30\text{mm}$)	68
Figure 3.21: Symmetrical Boundary for Coupled Bluff Splitter Body and Elastic Plate CFD Domain (Top View)	70
Figure 3.22: Schematic Setup of Output Voltage under Different Vibrating Frequency	71
Figure 3.23: Schematic Diagram of ESPI.....	72
Figure 4.1: Graph of Mesh Independence Study	74
Figure 4.2: Simulated Harmonic Response of PVEH Plate Model	75
Figure 4.3: Dynamic Characteristic of Piezoelectric Plate Using ESPI	76
Figure 4.4: Velocity Contour Showcasing Vortex Formation at 0.3s at wind speed of (a) 7 m/s (b) 10 m/s (c) 12 m/s (d) 14 m/s (e) 16 m/s (f) 18 m/s (g) 19 m/s (h) 20 m/s (i) 22.5 m/s (j) 25 m/s	78
Figure 4.5: Graph of Lift Force Acting on PVEH plate (N) Under Different Wind Speed (m/s)	79
Figure 4.6: Time Domain Graph of Lift Force Acting on PVEH Plate under Wind Speed = 19m/s.....	80
Figure 4.7: Graph of Vibrational Amplitude of the PVEH Plate (m) under Certain Excitation Vortex Frequency (Hz)	82
Figure 4.8: Deflection contour of model (a) 19 m/s isometric (b) 25 m/s isometric (c) 19 m/s top (d) 25 m/s top	83
Figure 4.9: Mesh Independence Graph of RMS Lift Force against Number of Elements	84
Figure 4.10: Elastic Plate Flow Induced Vibrations Validation: Time Domain Vibrational Displacement of the Tip of the Structure. (a) Different Time Step Sizes (Dettmer et al.) (b) Current Research FSI Simulation	85

Figure 4.11: Modal Analysis of 1cm Coupled Bluff Splitter Body and Elastic Plate (a) Fundamental Natural Frequency = 3.087 Hz (b) Second Natural Frequency = 19.287 Hz	86
Figure 4.12: Velocity Contour of Vortex Formation under Wind Speed (a) 0.3 m/s (b) 0.4 m/s (c) 0.513 m/s (d) 0.6 m/s (e) 0.7 m/s (f) 1.0 m/s (g) 1.5 m/s	88
Figure 4.13: Graph of Lift Force against Wind Speed of Coupled Elastic Plate and Bluff Splitter Body Model	90
Figure 4.14: Graph of RMS Tip Mesh Displacement against Wind Speed with Coupled Elastic Plate and Bluff Splitter Body Model	92
Figure 4.15: Deflection Contour of Structural Model at 1.5 m/s wind speed	93
Figure 4.16: First Bending Mode of Coupled Bluff Splitter Body and Elastic Plate Model at 3.087 Hz with Bluff Splitter Body Width of (a) 1cm (Top View) (b) 1cm (Side View) (c) 8cm (Top View) (d) 8cm (Side View)	94
Figure 4.17: Vortex Street Formation of Coupled Bluff Splitter Body and Elastic Plate Model with Different Bluff Splitter Body Width of (a) 0.005m (b) 0.01 m (c) 0.02 m (d) 0.03 m (e) 0.04 m (f) 0.06 m (g) 0.08 m	97
Figure 4.18: R.M.S. Coefficient of Lift Value against Different Aspect Ratio of Bluff Splitter Body-Elastic Plate Couple Model	99
Figure 4.19: RMS Tip Mesh Displacement with Different Bluff Splitter Body Width.	102
Figure 4.20: Velocity Contour of Vortex Formation with Different Elastic Plate Length (a) 0.02 m (b) 0.03m (c) 0.04m (d) 0.05m (e) 0.06m	105
Figure 4.21: RMS Lift Force of Difference Elastic Plate Length	106
Figure 4.22: Graph of RMS Tip Mesh Displacement against Elastic Plate Length	108
Figure 4.23: Graph of Displacement to Length Ratio against Elastic Plate Length	109

Figure 4.24: Modal Analysis of Coupled Semicircle Bluff Splitter Body and Elastic Plate Model (a) Top View (b) Side View	110
Figure 4.25: Velocity Contour of Different Cross Section of Bluff Splitter Body Shape	114
Figure 4.26: Graph of RMS Lift Force with Different Bluff Splitter Body Shape	116
Figure 4.27: Graph of RMS Tip Mesh Displacement with Different Bluff Splitter Body Shape	120
Figure 4.28: Vortex Formation with Different Angle Bluff Splitter Body of (a) 34.22°(b) 45° (c) 60° (d) 75° (e) 90° (f) 120° and (g) 146.31°	122
Figure 4.29: Graph of RMS Lift Force against Angle of Trapezoidal Bluff Splitter Body	124
Figure 4.30: Graph of RMS Tip Displacement against Different Angle of Trapezoidal Bluff Splitter Body	127
Figure C.1: Fluctuating Lift Force of different Wind Speeds (PVEH Plate)	141
Figure C.2: Fluctuating Lift Force of different Wind Speeds (Elastic Plate).....	142
Figure C.3: Fluctuating Lift Force of different Bluff Splitter Body Widths.....	143
Figure C 4: Fluctuating Lift Force of different Elastic Plate Lengths.....	144
Figure C 5: Fluctuating Lift Force of different Bluff Splitter Body Shapes.....	146
Figure C 6: Fluctuating Lift Force of different Bluff Splitter Body Edge Angles.....	147

Figure D.1: Tip Mesh Displacement of different Wind Speeds (PVEH Plate).....	148
Figure D.2: Tip Mesh Displacement of different Wind Speeds (Elastic Plate).....	149
Figure D.3: Tip Mesh Displacement of different Bluff Splitter Body Widths.....	150
Figure D.4: Tip Mesh Displacement of different Elastic Plate Lengths.....	151
Figure D.5: Tip Mesh Displacement of different Bluff Splitter Body Shapes.....	153
Figure D.6: Tip Mesh Displacement of different Bluff Splitter Body Angles.....	154

LIST OF TABLES

Table 1.1: Research Gap	6
Table 3.1: Material Properties and Dimensions of PVEH Plate and Bluff Splitter Body Model	49
Table 3.2: Material Properties of Coupled Bluff Splitter Body and Elastic Plate Model	50
Table 3.3: Structural Model Mesh of No. of Nodes, No. of Elements and Mesh Skewness of Different Coupled Bluff Splitter Body and Elastic Plate Model	62
Table 3.4: Fluid Domain Mesh of No. of Nodes, No. of Elements and Mesh Skewness of Different Coupled Bluff Splitter Body and Elastic Plate Model	63
Table 4.1: Difference Result between Harmonic Response Simulation and LDV Experimental Frequency of PVEH Plate.....	75
Table 4.2: Difference between Resultant Vibrational Frequency (Hz) of PVEH Plate and Natural Frequency (Hz).....	82
Table 4.3: Reynolds Number of Vortex Shedding with Different Wind Speed.	89
Table 4.4: Table of Resultant Vibrational Frequency to Natural Frequency of Coupled Elastic Plate and Bluff Splitter Body Model.....	92
Table 4.5: Vortex and Vibrational Displacement Frequency with Respect to the Aspect Ratio	101
Table 4.6: Fundamental Natural Frequency of Different Elastic Plate Length	103
Table 4.7: Vortex Frequency and Difference with Natural Frequency on Different Elastic Plate Length.....	108
Table 4.8: Vortex Frequency Produced by Different Bluff Splitter Body Shape and Difference with Natural Frequency	119
Table 4.9: Vortex Frequency with Different Bluff Splitter Body Angle and the Difference with Natural Frequency.....	126

LIST OF APPENDIX

Appendix A: Strouhal Number of Different Bluff Splitter Body Shapes	139
Appendix B: List of Publications.....	140
Appendix C: Fluctuating Lift Force Graph in Time Domain.....	141
Appendix D: RMS Tip Displacement Graph in Time Domain	148

University of Malaya

NOMENCLATURE

Symbols

$[C]$	Damping Matrix
$[F]$	Force Excitation Vector
$[\bar{I}]$	Identity Matrix
$[K]$	Stiffness Matrix
$[M]$	Mass Matrix
$[d]$	Piezoelectric Matrix Relating Strain/Electric Field
$[s^E]$	Compliance Matrix
$[\sigma_r]$	Damping Ratio
$[\omega_{or}]$	Eigenvalue of Mode r
$\{D\}$	Electrical Displacement
$\{E\}$	Electric Field Vector
$\{S\}$	Strain Vector
$\{T\}$	Stress Vector
$\{y\}$	Forced Response
$\{y_p(t)\}$	Generalized Displacement Matrix

A	Chord Length (m)
a_{ij}	Anisotropy Tensor
C_D	Drag Coefficient
C_e	Electrical Damping
C_L	Lift Coefficient
C_P	Electrical Capacitance
$\cos(\omega t)$	Harmonic Function
D	Bluff splitter Body Width (m)
E	Internal Energy (kJ)
f	Vortex Frequency (Hz)
$F(t)$	Force Excitation
F_D	Drag Force (N)
F_L	Lift Force (N)
f_N	Natural Frequency (Hz)
G	Gap
g	Gravitational Force
K_e	Electrical Stiffness

k	Thermal Conductivity Constant (W/m K)
k	Turbulent Kinetic Energy
L	Length (m)
$m_{i,e}$	Mass per Length (kg/m)
N	Normal Force (N)
p	Pressure Force (N)
\bar{p}	Mean Pressure Component
p'	Fluctuating Pressure Term
P_B	Buoyancy Production Term
P_{ij}	Exact Production Term
$P_{ij,b}$	Exact Production Term due to Buoyancy
P_k	Production Term
Q_{EAS}	Mesh Skewness
Re	Reynolds Number
Sc	Scruton Number
S_E	Surface Energy (kJ)
S_{ij}	Mean Strain Rate Tensor

St	Strouhal Number
t	Time
T	Temperature (K)
U	Flow Velocity/Flow Variable (m/s)
\mathbf{u}	Velocity Vector
\bar{U}	Mean Flow Variable Component
U'	Fluctuating Flow Variable Term
u_{crit}	Critical Velocity (m/s)
u_m	Mean Velocity (m/s)
U_r	Reduced Velocity
$V(t)$	Electrode Voltage (V)
V	Volume (m ³)
ν	Kinematic Viscosity
ν_t	Turbulent Kinematic Viscosity
x	Directional Component
α	Angle (°)
β	Magnification Factor

β	Coefficient of Thermal Expansion
δ_s	Logarithmic Decrement Damping Ratio
ε	Turbulent Dissipation
θ	Coupling Coefficient
θ_{equal}	Equal Cell Angle ($^\circ$)
θ_{max}	Maximum Cell Angle ($^\circ$)
θ_{min}	Minimum Cell Angle ($^\circ$)
θ_r	Phase Angle ($^\circ$)
μ	Dynamic Viscosity (N s/m ²)
μ_t	Turbulent Dynamic Viscosity
ρ	Density (kg/m ³)
τ	Shear Force (N)
Φ	Mode Shape Matrix
Φ_{ij}	Pressure-Strain Term
Φ_r	Normalized Mode Shape
ω	Specific Rate of Dissipation
Ω_{ij}	Vortices Tensor

University of Malaya

Abbreviation

<i>2D</i>	Two Dimensional
<i>3D</i>	Three Dimensional
<i>ALE</i>	Arbitrary Lagrangian Eulerian
<i>CAD</i>	Computer Aided Design
<i>CAM</i>	Computer Aided Modelling
<i>CSD</i>	Computational Structural Dynamics
<i>CFD</i>	Computational Fluid Dynamics
<i>DNS</i>	Direct Numerical Simulation
<i>FEM</i>	Finite Element Method
<i>FFT</i>	Fast-Fourier Transform
<i>FSI</i>	Fluid-Structure Interaction
<i>LDV</i>	Laser Doppler Vibrometer
<i>LES</i>	Large Eddy Simulation
<i>PVEH</i>	Piezoelectric Energy Harvester
<i>RANS</i>	Reynolds Average Navier Stokes
<i>RMS</i>	Root Mean Square
<i>SGS</i>	Small Grid Scale
<i>SSG</i>	Speziale-Sarkar-Gatski
<i>SST</i>	Shear-Stress Transport
<i>VIV</i>	Vortex Induced Vibration
<i>VIVACE</i>	Vortex Induced Vibration Aquatic Clean Energy
<i>WALE</i>	Wall-Adapting Local Eddy-Viscosity

CHAPTER 1: INTRODUCTION

1.1 Energy rating

In the 21st century, electrical energy has been an essential element for everyday lives. In year 2012, according to the statistic done by BP review 2014, the total energy consumption around the world had reached 12,730.4 *Mtoe*, increased by 247.2 *Mtoe* which is around 2.3% from year 2012 and also increased by 2,786.6 *Mtoe* or it is around 28% increase for the past 10 years. With the rapid development of high technology and telecommunication industry, high demand of electricity is required and thus, a high demand of supply is needed to meet this demand (Energy Academy, 2014).

At the current state, fossil fuels such as petroleum, coal, and natural gas are still the main supply for the electrical energy generation industry all around the world. As fuels are non-renewable energy, it is depleting in a critical manner. It is predicted that fossil fuels can only last for another 50 years before reducing in half, as the growth of human population is high. In the year 2012, a total of 8,979 *Mtoe* is consumed every year. This shows that the percentage to the total energy consumption is around 73% whereby it occupies one third of the total (Agency, 2014). As fuels need to be conserved, renewable energy is an alternative option that can reduce the people relying on fossil fuels.

Renewable energy which are introduced and more popular in the current era are hydroelectric, solar energy, wind energy, biomass, and geothermal. The total renewable energy capacity in the world is now 1,560 *GW*. Hydroelectric generation has the highest capacity recording a 1000 *GW* of power followed by wind power 318 *GW* and solar 139 *GW*. For the past 10 years, solar energy and wind energy has the fastest growth recording a rise of 98% and 87% respectively (REN21, 2014).

In Malaysia, the main energy supply comes from oil, natural gas, coal, hydro and renewables. The total energy supply in year 2012 is around 83,938 *ktoe* with natural gas being the main supply with a percentage of 46.0 % followed by oil 32.1 %. The highest renewable energy supply in Malaysia is hydroelectric which holds a figure of 2.9 %. The total demand of energy in the exact year is around 46,711 *ktoe*. This figure shows that in Malaysia, sustainable energy is still not a very popular method of energy generation (Energy Commission, 2014).

Malaysia's power generation sector is facing challenges with sustainability issues to ensure a safe and reliable energy is being continuously supplied. Green energy is the most important substitution to non-renewable energy such as oil, natural gas and coke in which is Malaysia's main energy supply field. In Malaysia, wind energy is not a popular alternative for energy generation with scarce of investigation towards it. This is because of the wind speed in Malaysia is relatively low and not suitable for large wind farm energy harvesting. Wind energy plant should be chosen wisely depend on the potential of wind power at the site (Oh, Pang, & Chua, 2010).

The mean wind speed in Malaysia urban areas are around 1 m/s - 2.65 m/s while the highest wind speed recorded is 5.4 m/s. It is also shown that when the height gets higher, the wind power increases and the larger the energy density (Irwanto, Gomesh, Mamat, & Yusoff, 2014). A study conducted by Siti et al. showed that the highest wind speed in Peninsular Malaysia is located mainly at the East Coast specifically Mersing followed by Kota Bahru and Kuala Terengganu (M.R.S Siti, 2011). A study conducted by Mudathir Funsho Akorede et al. learned the wind capacities and power generated on different wind turbine sites. The highest wind capacity factor recorded is at Mersing with the value only 4.39%.

1.2 Vortex-Induced Vibration Overview

Vortex-induced vibration (VIV) is a phenomenon caused by the interaction of structures with vortex flow formed from flow instabilities after separation by bluff splitter bodies. Vortex flow created from interception of fluid flow by bluff splitter body has a certain frequency and force depending on the flow speed and bluff splitter body shape and size. When vortex interacts with the structure, the structure reacts with vibrational frequency and amplitude relative towards the lift force and frequency of the vortex. VIV had significant impact in various engineering design aspect from buildings and bridge structures, chimney stacks, heat exchanger pipes to ocean risers and pipelines.

In past few decades, prevention of VIV problem had spurred many fundamental studies in this field and some comprehensive overview is provided by P. W. Bearman (1984); Khalak and Williamson (1999); Parkinson (1989); Sarpkaya (1979). In the past, vortex induced vibration had been causing many fatigue problems and destruction in many engineering fields such as buildings, bridges, pipelines, stacks and many more. The most significant incident involving vortex induced vibration is the breakdown of Tacoma Narrows Bridge. It is said that the bridge experiences vortex induced vibration when wind flow passes through it. The bridge vibrates at a frequency near to the structure's natural frequency thus it undergoes resonance vibration. Resonance occurs causing the bridge to sway chaotically causing fatigue damages overtime, thus the structure eventually breakdowns (Billah & Scanlan, 1991; Wyatt, 1992).

In recent years, with the rapid development of piezoelectric harvester, vortex induced vibration research had branched from prevention to energy harvesting. Huang (2013) states that piezoelectric materials able to convert electrical and mechanical energy with parallel or series piezoelectric bimorph connections. Parallel piezoelectric bimorph coupling will generate higher efficiency in electromechanical conversion, twice of series coupling (Huang & Ma, 2009). With special bimorph concept by Ma and

Huang, the piezoelectric can produce larger voltage through displacement (Ma, Lin, Huang, & Lin, 2007). It is because as stated with this configuration, when the plate vibrates at resonant frequency, electric impedance will drop to a local minimum maximizing voltage output (Krushynska, Meleshko, Ma, & Huang, 2011).

Vortex-induced vibration harvesters come in many forms and design. Most of the design of vortex induced vibration involves a cylinder bounded with spring vibrating freely aimed to be placed in location with water flow such as waves from sea and river current. The first official patented vortex induced vibration harvester was Vortex Induced Vibration Aquatic Clean Energy (VIVACE) by Bernitsas, Raghavan, Ben-Simon, and Garcia (2006). This device is aimed to harvest most water currents including waves, tides, dams and turbines as low as 2 mph. Following it, many different studies had been conducted focusing on enhancing the performance of the vortex induced vibration.

1.3 Problem Statement

Vortex induced vibration energy harvesting had become more popular throughout the years, there exists a need to look into different ways to improve the performance of the harvesting technique and making it easier to be implemented in more areas especially with lower air flow speed instead of mainly in places where water flow exists. Although cylindrical vortex induced vibration harvester concept had proven to be effective in harvesting, but it is comparably large in size and not suitable in atmospheric low air flow speed of 1 to 4 m/s due to its size and weight, it is viewed as a possible improvement with the further research.

Inspired by H. D. Akaydin, Elvin, and Andreopoulos (2012); De Nayer, Kalmbach, Breuer, Sicklinger, and Wüchner (2014); Kuhl and DesJardin (2012); Wen, Schulze, Billep, Otto, and Gessner (2014b), these researchers practiced the use of a

coupled bluff splitter body and elastic plate model. All the models from the studies listed above showed that when it is placed in a flow, vortex induced caused the flexible part to vibrate due to vortex generated. A piezoelectric plate or film was used to generate electricity from mechanical energy conversion. These models proposed above were all smaller in size while having decent energy generation ability which is also more robust on-site installation.

Previous researches had investigated many different designs or orientation of vortex induced vibration (VIV) energy harvesters. A VIV harvester with the presence of a bluff splitter body is believed to have high energy conversion efficiency. It is realized that the development in vortex induced vibration energy harvester have yet to look into enhancement through structural design modifications and surrounding wind speed of a single small harvester unit. In Table 1.1, the research gap is presented by comparing some past research and current research.

Table 1.1: Research Gap

Previous Research	Author	Gap	Current Research
Movement Induced Vortex Induced Vibration Harvester of VIVACE using large rigid cylinder, spring and generator system	M. Bernitsas et. al	The system is slightly complex and installation area focused in rivers or oceans with consistent flow	A less complex Instability Induced Vortex Induced Vibration (IIEVIV) energy harvesting system is an alternative VIV harvester system using a piezoelectric plate undergo flow instabilities
An elastic plate with PVDF patch placed in vortex flow with different mounting position creating VIV.	O. Goushcha et al.	A large aspect ratio bluff body installed upstream is found to be able to generate better flow shedding that excites VIV on the elastic plate	A T-shaped bluff splitter body and elastic plate is designed to improve the VIV performance through larger upstream flow shedding effect creating stronger vortex flow.
A heavy mass or another IIEVIV energy harvester is placed at the tip of the elastic plate to enhance vortex induced vibration by lowering the plate's natural frequency. Lower frequency needed for resonance.	H.D. Akaydin et al.	This system arrangement heavily depends on the movement of the tip mass under the effect of VIV. Besides, installing a heavy body at the tip of the cantilever plate will induce mass loading effect and caused damage to the elastic plate after a period of time.	Bluff splitter body is set as a fixed body, upstream of the flow. By using the design and size alteration, improvement in VIV also able to achieve. Furthermore, prolongs the life span of the PVEH plate attached without damage.
A thin film with high elasticity is used with PVDF patch placed on the surface. VIV occurred on the elastic film which induced electricity through the PVDF patch on it	J.J. Allen and A.J. Smiths	A PVDF patch is very dependent on the vibration characteristics of the host cantilever plate where only placing at the nodal point with highest strain is able to produce maximum power output	The use of a piezoelectric bimorph as elastic plate provides more control towards the effect of vibration and effective output produced

1.4 Objectives

This study is aimed to further enhance the existing design through the best configuration and parameters without affecting the energy harvesting purpose of the design in which:

- To investigate the vortex induced vibration performance enhancement of a coupled bluff splitter body and elastic plate model under different wind speeds.
- To investigate the vortex induced vibration performance enhancement of a coupled bluff splitter body and elastic plate model under different bluff splitter body sizes.
- To investigate the vortex induced vibration performance enhancement through shape design modifications and edge angle of coupled bluff splitter body.

1.5 Research Flow

The vortex induced vibration performance enhancement of the coupled bluff splitter body and elastic plate model will be investigated through the change in wind flow speed, change in aspect ratio and bluff splitter body model design. Next, the CAD model of different coupled bluff splitter body and elastic plate model design will be drawn and materials will be assigned. The model will then undergo modal analysis simulation from ANSYS and the result is validated with previous studies. Once the model is validated, Computational Fluid Dynamics (CFD) and Computational Structural Dynamics (CSD) simulation boundary condition and numerical parameter is defined. If the model is not validated CAD design and material assigning process is repeated. Following that, an initial CFD analysis will be performed to ensure the settings are correct while conducting mesh independence study. If the settings are correct, FSI coupling simulation is conducted and the results will be analyze, discuss and conclude. The research flow chart is shown in Figure 1.1.

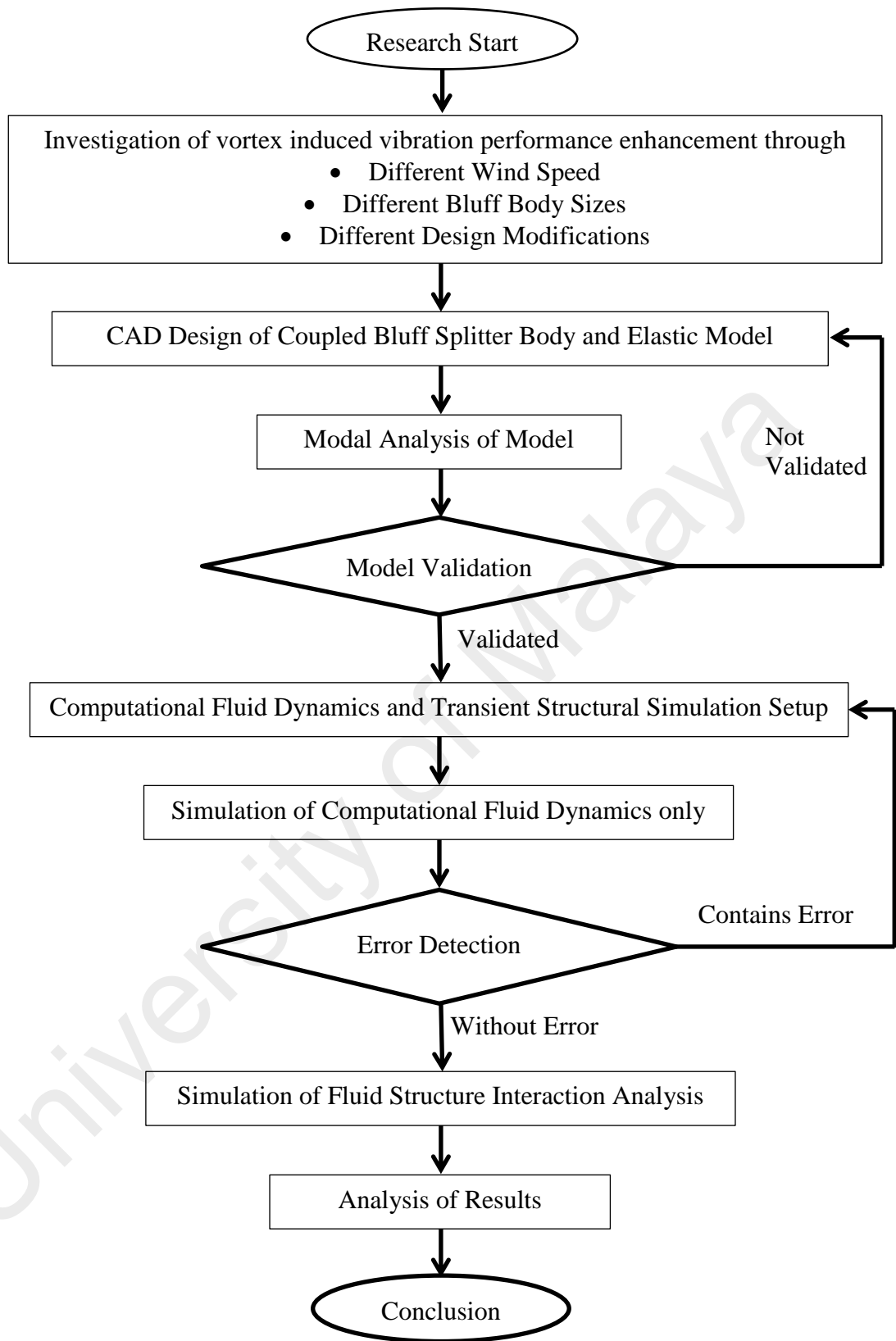


Figure 1.1: Research Flow Chart

1.6 Organization of Thesis

This dissertation showed how different parameters can impact the performance of vortex induced vibration of a coupled bluff splitter body and plate model. Chapter 2 introduced the theory of vortex induced vibration and all the concepts behind the occurrence of VIV. In this chapter also reviewed the other related investigation and showed the difference from the current work being carried out. In the last part of chapter 2, the methods used to carry out the investigation and the background theories were discussed.

Chapter 3 describes the methods used in conducting the investigation through simulation analysis which is from modeling of the structure to meshing of fluid domain and structural domain and lastly the settings of fluid structure interaction (FSI) simulation. Different model design and detailed FSI settings were introduced in this chapter covering different objectives to be achieved in this thesis.

Chapter 4 showcased all the results obtained through the methods used in Chapter 3. A few important parameters were being highlighted, mainly being vortex formation contour, lift force, vortex frequencies and resulting VIV performance. Analyses of results were also done in each sub-section.

The last chapter which is Chapter 5 shows the summary of the whole thesis and discussed the direction of future works.

CHAPTER 2: LITERATURE REVIEW

2.1 Vortex Flow Formation

Vortex flow generation is strictly associated with flow separation when encountering a bluff splitter body. In real life external flow frequently encounters solid bodies including automobiles, buildings, smoke stacks, pipelines, bridges, turbine blades, even the transportation of red blood cell in blood flow. Good understanding in flow over bodies helps in many engineering problems for example, reduction in drag and fuel consumption, maximizing airfoil lift efficiency, reduce noise and vibration of structures and in this study to maximize and extract vibration created from vortex flow (Munson, Young, & Okiishi, 2002).

When a free flow stream encounters these bluff splitter bodies, fluid boundary will separate from the surface of the body and form a separation region between the body and downstream flow. In the separated region, flow recirculation and backflow takes place due to pressure difference, creating a low pressure region called vortex. The larger the vortex region formed, the larger is the pressure value applied. Between different flow properties such as laminar, turbulent and ideal flow, the resulting vortex is different as shown in Figure 2.1. Vortex flow disrupts flow when propagating downstream, leaving an unstable trail of alternating velocity flow called wake. Vortex flow refers only to the unstable flow at the separation region, while wake on the other hand propagates downstream until the flow stabilizes as displayed in Figure 2.2.

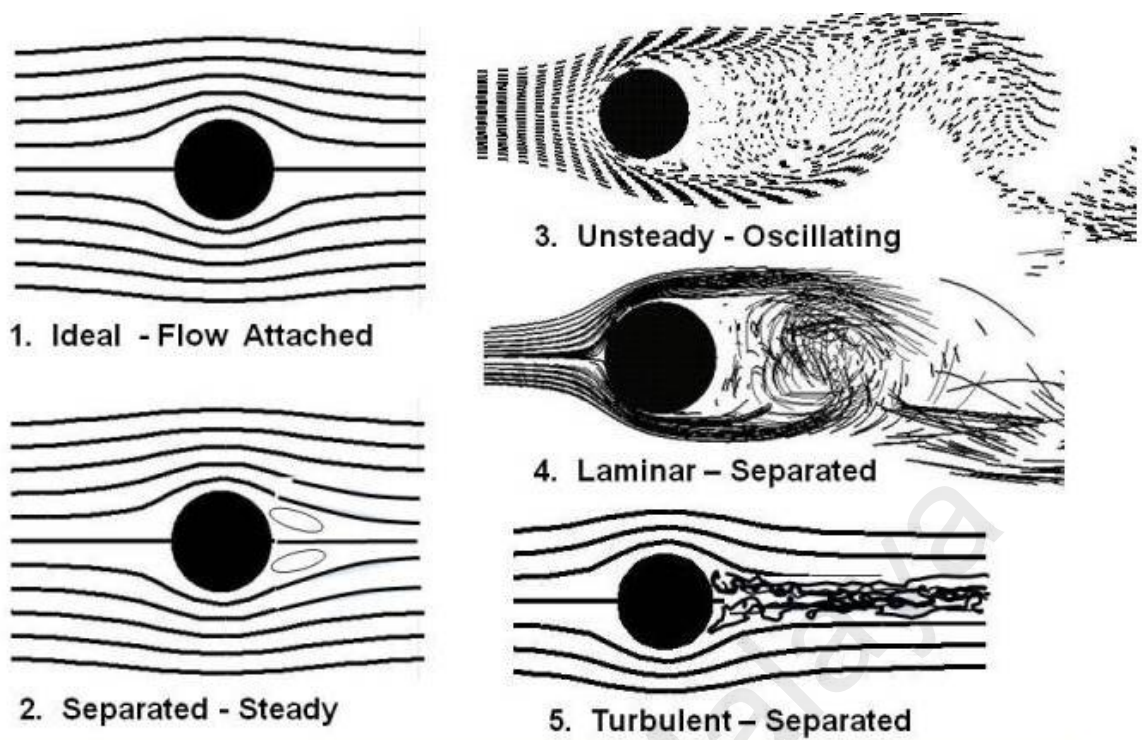


Figure 2.1: Different Flow Undergoes Separation When Encountering Bluff Splitter Body (Source: <https://www.grc.nasa.gov/>)

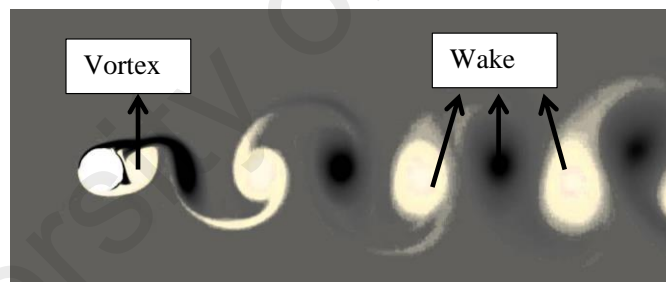


Figure 2.2: Vortex (Separation Region) and Wake (Source: GDTEch Belgium)

2.2 Vortex Induced Vibration

As mentioned in Section 2.1, flow shedding/separation by bluff splitter bodies generates unstable flow known as vortex. Vortex is the main cause for a natural phenomenon that happens commonly known as Vortex Induced Vibration (VIV). VIV is the result of interaction between structural dynamics and fluid mechanics. As shown in Figure 2.3, vortex forms when fluid flow encounters a bluff splitter body as it tends to shed and roll up behind the body, creating imbalance in pressure distribution and frequency.

Henceforth, this periodic imbalance force with certain frequency acting on the structure causes vibrational motion of the structure itself (Barrero-Gil, Pindado, & Avila, 2012).

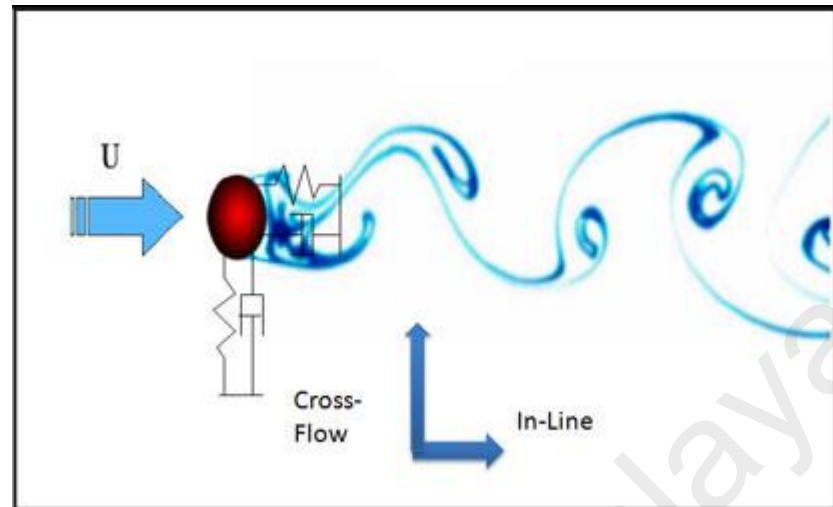


Figure 2.3: Von Karman Vortex Street behind Bluff Splitter Body When Flow Passes Through (Source: web.mit.edu)

In order for vibration induced by vortex to be successfully generated, a few criterias as listed below had to be fulfilled:

2.2.1 Critical Velocity

Vortex-induced vibration introduces a special phenomenon called “lock-in” or synchronization in the frequency response. Lock-in theory explains the phenomenon of a model’s vibrational frequency synchronizes well to the vortex frequency generated (Giosan & Eng, 2013). It will first vibrate at a random frequency and amplitude, but when it reaches steady lock-in condition, the vibration amplitude has a constant frequency near the vortex frequency. When the vortex frequency are close the system’s natureal frequency, the system will undergo resonance lock-in followed by very large amplitude of vibration generated by the system. For the system to undergo resonance lock-in, the wind speed must be near to the critical velocity for a certain mode i , the effect of critical velocity happens when the wind is in the range of $u_{crit,i} > 1.25 u_m$ (Breinlinger et al., 2011).

$$u_{crit} = \frac{D \cdot f_N}{St} \quad (2.1)$$

where u_{crit} is the critical velocity, u_m is the mean velocity, D is the bluff splitter body width where vortex shedding occurs, f_N is the natural frequency and St is the Strouhal number.

2.2.2 Strouhal Number, St

Strouhal number is a dimensionless number describing the oscillating flow mechanism introduced by Vincenc Strouhal. Strouhal number as described in Equation (2.1) has a certain value for each different shape of bluff body placed in the flow as shown in Appendix A (Gulvanessian, 2001).

2.2.3 Scruton Number, Sc

Scruton number also known as the mass damping ratio is also a parameter to realize vortex induced vibration although it is being suggested by Sarpkaya (1997) to not combine both mass ratio and damping together. It is a common practice currently to combine both mass and structural damping as a parameter to determine the vortex induced vibration. According to Khalak and Williamson (1999), there are 3 types of branches of vortex induced vibrations, upper branches which is the resonance lock-in, upper-lower branch which is the transition phase and lower branch with small vibration. Khalak and Williamson did a comparison with a low mass and structure damping value and a higher mass and structure damping value by Feng (1968), the lower mass damping ratio proven to have a much better vibrational performance.

Scruton number is a dimensional number that includes mass ratio, damping, fluid density and structural length shown in Equation (2.2) below. If Scruton number is high, vibrations will be suppressed because of the high mass and damping ratio thus no or small vibrational displacement will take place. Only if Scruton number is lower than 15 the structure will vibrate significantly under influence of vortex (Kärnä, 2009).

$$Sc = \frac{2 \cdot \delta_s \cdot m_{i,e}}{\rho \cdot D^2} \quad (2.2)$$

where Sc is the Scruton number, δ_s is the logarithmic decrement damping ratio, $m_{i,e}$ is the mass per length, and ρ is the density, D is the bluff splitter body width

2.2.4 Reynolds number, Re

Discovered by Osborne Reynolds, Reynolds number is used to describe the flow regime as the ratio of inertial force to the viscous force. The equation of Reynolds number passing through a channel is described in Equation (2.3) as below:

$$Re = \frac{\text{Inertial Force}}{\text{Viscous Force}} = \frac{\rho UL}{\mu} \quad (2.3)$$

where Re is the Reynolds Number, U is the flow velocity, L is the length of the model and μ is dynamic viscosity.

At large Reynolds number, the inertial force which is proportional to fluid velocity and density is largely related to the fluctuations while smaller viscous force is unable to suppress the random fluid movement, thus this fluid is known to be turbulent. In smaller Reynolds number flow, the relatively larger viscous force is able to suppress the rapid fluctuations of the fluid, hence keeping the fluid flow in an ordered straight-lined flow known as laminar flow.

When a fluid passes through a bluff splitter body, inertia and viscous effects played an important role in determining the flow characteristic downstream of the flow.

When flow passes through a body, boundary layer formed on the surface of the object with velocity near to zero due to viscous effects. As fluid flow velocity increases, the inertia forces increases causing Reynolds number to increase proportionally. Turbulent flow and transitional flow passing through a bluff body creates a separated region as per mentioned in Section 2.2. Only when the flow is turbulent the separated region is

evolved into a wake region that contains random irregularity in flows. Shown in Figure 2.4 is the flow pattern over a cylinder with different Reynolds number.

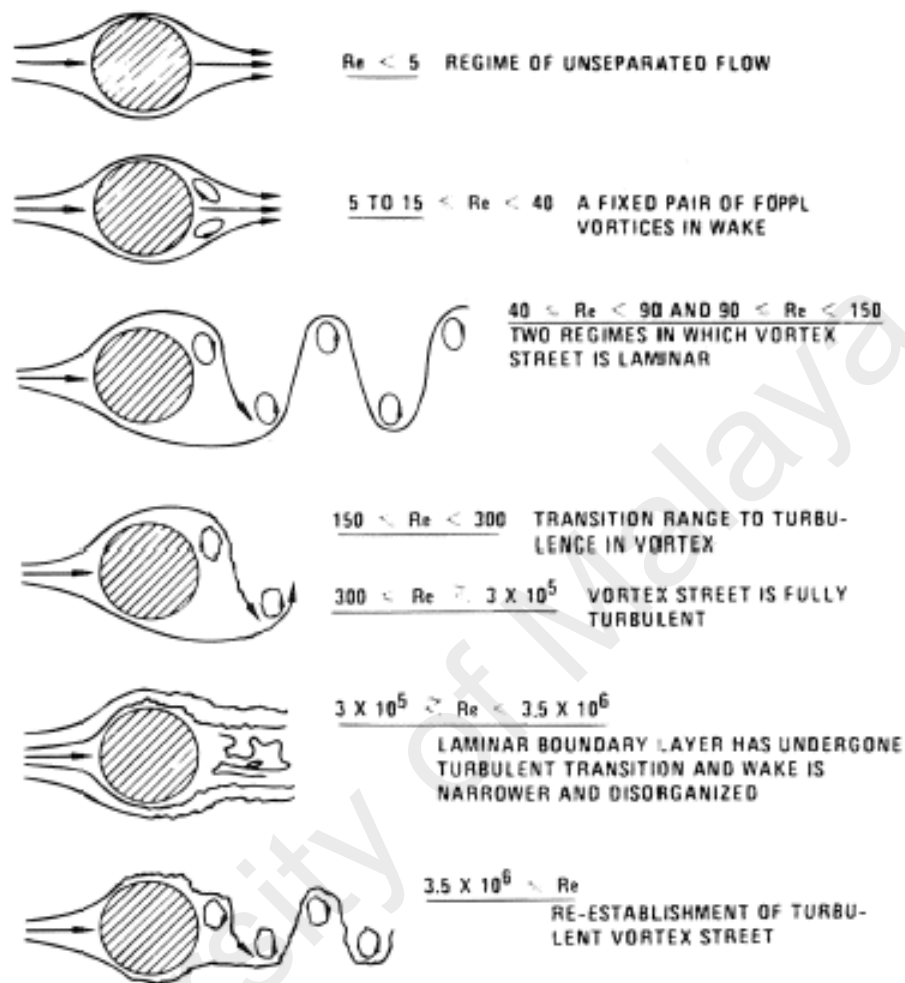


Figure 2.4: Vortex Flow Pattern under Different Reynolds Number Flow. (Source: Thermopedia)

2.3 Vortex Induced Vibration in Energy Harvesting

There are various fields of investigation regarding vortex induced vibration, including suppression, harvesting, structure deformation and many more. In this section, discussion mostly revolved around studies that had been conducted mainly on energy harvesting from vortex induced vibration are listed. These studies stretched from the 90s till today, had contributed a lot towards the knowledge of VIV harvesting. There are two main methods that had been explored in this field, which is cross-flow vibration of cylinder and vortex induced vibration of thin cantilevered plate, while many modified variations of the mentioned methods are studied.

2.3.1 Cylindrical Cross-Flow Vortex induced Vibration

Bluff body cross flow vortex induced vibration is the most common case that is being investigation in vortex induced vibration field especially with cylindrical model. Griffin (1995) looked into the vortex formation when it passes through a bluff body. Vortex strength depends heavily on the vortex formation length and it is mentioned in the Griffin's study that the maximum vortex strength is visible at the end region of vortex formation length. Norberg (1994, 2001) commented that fluctuating lift acting on a stationary cylinder depends on the Reynolds number and aspect ratio. Lift coefficient for the span wise length of the cylinder can be predicted in laminar flow but dramatic variation between sectional lift coefficients occurs in Reynolds number 0.3×10^3 – 2.2×10^5 .

Following the development in stationary cylinder vortex generator, some researchers pursued further to look into vortex induced vibration of a cylinder hanged freely with spring. S. Hiejima and T. Nomura, Chunning Ji et al., Mohd Asamudin A. Rahman et al., T.K. Prasanth and S. Mittal, M. J. Thorsen, Meng-Hsuan Chung and many more had been looking at different aspects of parameters that affect the vortex induced vibration of a single degree of freedom cylinder. Implementing finite element method based on Arbitrary Lagrangian Eulerian (ALE) formulation, Hiejima and Nomura (1999) investigated the oscillating cylinder caused by periodic velocity excitation. Computational mesh nodes can be moved with continuum in normal Lagrangian method or remained fixed in Eulerian manner, allowing rezoning and also able to calculate greater distortion problems (Donea, Giuliani, & Halleux, 1982).

Mentioned above in Section 2.4.4, Reynolds number is one of the important factors that determine the effectiveness of a vortex induced vibration of a cylinder. Ji, Xiao, Wang, and Wang (2011) had used the same boundary setup as S. Hiejima and T. Nomura but with different flow parameters to look into elastically supported cylinder

performance under low-Reynolds number. They discovered that by matching the natural frequency to the Strouhal frequency and vibrational frequency, the model can vibrate at higher amplitude with smaller reduced velocity of $U_r = 4$. Étienne and Pelletier (2012) also proven that vortex induced vibration can occur with Reynolds number as low as $Re = 47$. Prasanth and Mittal (2008) discovered that low mass oscillators enhanced the lock-in vibration regime of the cylinder.

Rahman, Leggoe, Thiagarajan, Mohd, and Paik (2016) explained that generally, with higher aspect ratio cylinder, the structure will experience higher amplitude of vibration whilst when $L/D = 1$, the vortex intensity is significantly lower and non-periodic pattern is observed. Chung (2016) placed the elastically supported cylinder by a certain gap between plane walls and determines the effect of the gap ratio towards vortex induced vibration. It is discovered that size of lock-in zone increases and the peak vibrational amplitude decreases with decreasing gap ratio while peak vibration amplitude happens at larger reduced velocity for smaller gap ratio.

Since the introduction of Vortex Induced Vibration Aquatic Clean Energy (VIVACE) by Bernitsas et al. (2006) the development of cylinder harvester and different improvement had been added to the system by different researchers. Under M. Bernitsas, some improvement had been made towards improving the system in general. Omar Kemal et al. changed the design to reduce the tip flow vortices where it is stated that vortices formed at the tip does not contribute towards model lift force and may cause more drag towards the model Kinaci, Lakka, Sun, and Bernitsas (2016). Reynolds number is one of the important factors in determining the performance of the VIVACE according to Raghavan and Bernitsas (2011). The obtained results showed that in the transition regime between laminar and turbulent region, the model undergoes high amplitude of oscillation and sustains even with high damping values, proven to be optimal for energy harnessing.

Some researchers utilize single cylinder VIV to harvest energy as mentioned below. Barrero-Gil et al. (2012) concluded that mass damping ratio plays a role in defining maximum efficiency and the reduced velocity is governed by the mass ratio. On the other hand, P. Meliga introduced an actuation procedure which analyzes the flow using Navier-Stoke equation and forced the vibration with unsteady jet flow successfully increasing the harvesting efficiency by 3.5 % (Meliga, Chomaz, & Gallaire, 2011). Ashwin Vinod (2013) looked into the surface roughness of the cylinder harvester and found out that zero roughness cylinder surfaces produces highest amplitude and being most optimum for vortex energy harvesting.

Instead of a rigid cylinder Grouthier, Michelin, Bourguet, Modarres-Sadeghi, and de Langre (2014) implement a novel harvester design using flexible cables instead of rigid cylinder. The optimal efficiency occurred during lock-in of the tensioned and hanging wire is almost same as the rigid cylinder. The cable design is able to have multiple modes of high efficiency regions for harvesting while rigid cylinder exhibits only one mode. Overall the tensioned cable produces more robustness and lower discontinuities which is better as compared with rigid cylinder. Ding, Zhang, Wu, Mao, and Jiang (2015) investigated on the effect of different shapes bars including cylinder, square, triangle and trapezoidal whereby cylinder and trapezoidal have better energy harvesting performance as the amplitude is larger under same Reynolds number of flow.

2.3.2 Tandem Cylinder Configuration Vortex Induced Vibration

Investigations had moved to dual and multi-cylinder where vortex-induced vibration efficiency is better compared to single cylinder. Dual cylinder arrangement had spurred creativity of researchers, some had the cylinder put side by side, some placed upstream and downstream while some were located separately where only one is exposed to fluid flow affecting the vibration of connected cylinder

Cylinders placed in an upstream and downstream configuration is the most common configuration used by researchers such as A. Sohankar, Norio Kondo, Yao Bao et al, Yoshiki Nishi, and D. Brika and A. Laneville. Ahmad Sohankar's study involved only looking at forces acting on both upstream and downstream stationary square cylinder with different Reynolds number (Sohankar, 2014). Norio Kondo treated upstream cylinder as two-degree of freedom while downstream cylinder as fixed Kondo (2014). D. Brika and A. Laneville had a configurations which is the opposite of Norio Kondo which fixed the upstream cylinder and the downstream cylinder is kept flexible in two-degrees of freedom Brika and Laneville (1999). In the three studies above, it is agreed that spacing between cylinders brings difference to the result obtained as the upstream cylinder creating wake that affects the vibration of downstream cylinder.

Norio mentioned that although with small spacing ratio, the model upstream is able to vibrate and achieves resonance with reduced velocity, $U_r = 1.5-4.4$. Reduced velocity is a dimensionless number where velocity is normalized with the natural frequency and width of the model shown in Equation 2.4 below.

$$U_r = \frac{U}{f_n D} \quad (2.4)$$

where U_r is the reduced velocity, f_n is the natural frequency and D is the width of the model.

The model by Brika and Laneville (1993) increased of spacing ratio from 7 to 25. At 7 and 8.5 spacing ratio the model has the highest amplitude due to wake galloping and decrease at other spacing ratio. Unlike Brika, Bao, Zhou, and Tu (2011) used the same configuration but with the change in the angle between 2 cylinders. With Large angle α , until the maximum of 34.22° the cylinder downstream locks-in with the vortex from the upstream cylinder. When $\alpha > 34.22^\circ$ it behaves like a distinct single cylinder oscillating with vortex created on that particular cylinder. Yoshiki Nishi, Ueno, Nishio,

Quadrante, and Kokubun (2014) developed a VIV power extraction device and tested out and compared the different configurations listed above having either one cylinder moves freely and the other fixed and both cylinders move. It is found that configuration with movable upstream and fixed downstream yielded the largest vibration.

There is also a side-by-side cylinder arrangement studied by Pang, Zong, Zou, and Wang (2016) at small pitch ratio, two cylinders behave like individual singular cylinder undergoes vortex induced vibration. When in asymmetric regime, the gap flow biases one cylinder over the other and finally in symmetric flow, three flow patterns was observed, i.e. in-phase flow pattern, anti-phase flow pattern and hybrid flow pattern. Zhao, Murphy, and Kwok (2016) compared the performance of the side-by-side arrangement and the tandem arrangement. For side-by-side arrangement it reaches the maximum amplitude twice of the single cylinder with gap, $G = 0.5D$ but the wake resembles a single cylinder due to merging of vortex. $G = 1D$ produces strong vortex interaction leading to irregular vibrations and lift coefficients. For $G > 1D$, the vortex is out of phase and cancels out each other producing zero amplitude. On the other hand, the tandem arrangement shows larger vibrational amplitude than single cylinder for all the gaps.

The last arrangement of tandem cylinder is dual mass system developed by Y. Nishi (2013). This arrangement involves only one cylinder to be in contact with fluid flow and undergoing vortex induced vibration. The other cylinder will vibrate at the frequency similar by the driving cylinder. This system shows enhancement through wide range of power coefficient and advantageous in variable frequencies.

2.3.3 Multi-Cylinder Vortex Induced Vibration

Multi-cylinder configuration involves multiple cylinders arranged in a certain arrangement undergoing vortex induced vibration. This literature will only cover two

main impactful configurations involving square and tandem arrangement of 4 cylinders. The model proposed by Zhaolong Han et al involved vortex induced vibration of 4 elastically supported cylinder placed in a square arrangement shown in Figure 2.5. The cylinders movement behaves symmetrically side by side for example between 1 and 4 and between 2 and 3. The movement in different Reynolds number usually resembles “8” and “O” and like other cylinder movement, it produces largest amplitude during lock-in (Han et al., 2015).

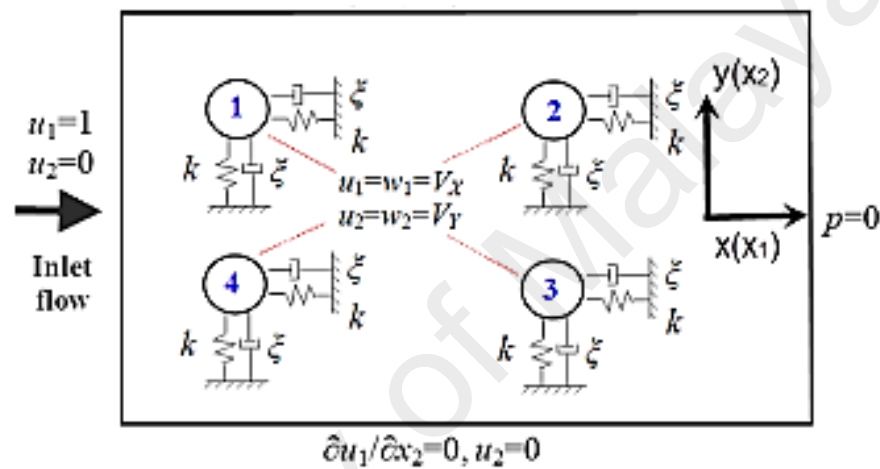


Figure 2.5: Square Arrangement of VIV Harvester Cylinder (Source: Zhaolong Han et al.)

The other arrangement in a straight tandem line is proposed by Hobbs and Hu (2012) where all cylinders are connected parallel in a straight line. Hobbs explained that when piezoelectric cylinders were grouped together, the vortex from upstream cylinder increases the power of downstream cylinder. But when the cylinders were grouped, the peak power vortex sways from a single cylinder and in this case the maximum power occurs when vortex frequency over structural model’s natural frequency ratio, $f/f_n = 1.6$.

2.3.4 Cantilever Configuration with Bluff Splitter Body

Bluff Splitter Body coupled with cantilever elastic plate is also another method implemented to harness the power of vortex induced vibration. Vortex induced vibration of a cantilever plate usually involves the use of bluff body commonly a

cylinder to separate the flow for vortex generation. Apelt and West (1975) discovered that elastic plate with different length attached behind the bluff body affects the flow characteristic. Very short elastic plate with length over width ratio, L/D less than 2 significantly modifies the characteristics of flow past cylinder, Short elastic plate L/D between 2 and 5 further modifies the drag and vortex characteristics of the flow and lastly for L/D more than 5 the flow reattaches downstream of the plate creating no difference at that region.

Cimbala and Garg (1991) and Gu, Wang, Qiao, and Huang (2012) model is a rigid plate free to rotate around an attached cylinder. From these two studies, it can be concluded that with the addition of splitter plate behind the cylinder bluff body, the root mean square drag and lift coefficient acting on the cylinder is greatly reduce up to 30% and 90% respectively by the downstream plate effectively preventing fatigue failure happening on the cylinder. Under the effect of vortex, the plate is vibrating periodically around the cylinder.

In recent years, studies focused more on a rigid cylinder coupled with a cantilevered flexible plate vibrating along with the vortex frequency from the upstream cylinder. Different variations of coupling had been introduced by researchers. G. De Nayer, Quan Wen and J.M. Kuhl implemented fixed cylinder coupled with flexible plate attached with cantilever boundary. From the studies, it was learned that flexible plate will vibrate with structural mode similar to the frequency of the vortex. The damping properties of the flexible plate had to be included in fluid-structure interaction (FSI) simulation in order to accurately predict the outcome (De Nayer et al., 2014). Kuhl and DesJardin (2012) mentioned periodic vibrations can be sustained with large bluff body at the upstream leading edge of flow. Wen, Schulze, Billep, Otto, and Gessner (2014a) investigated the difference between cylindrical and plate bluff body, proved cuboid bluff body is able to produce 4 times higher pressure acting on the

flexible plate downstream comparatively. Although it has higher pressure force, the existence of secondary wake by cuboid bluff body brings negative impact to the system.

Other more special variations VIV designs were proposed by Marco Demori and H. D. Akaydin. Demori, Ferrari, Ferrari, Farisè, and Poesio (2014) developed an energy harvesting system involving a detached cuboid bluff body with a gap to the cantilevered piezoelectric plate. H. D. Akaydin et al. (2012) reversed the design listed above, the cantilever plate with piezoelectric base is fixed at the end and a bluff body is fixed at the leading edge of the plate. The tip cylinder helped in increasing aero-elastic efficiency and reducing the flow velocity required to achieve the maximum power

Some researchers did not use a bluff body but only include a hyper-elastic design of plate, it is said that when the flow flows through the design, vortex is still be able to cause the model to vibrate. McCarthy, Watkins, Deivasigamani, John, and Coman (2015) uses a design inspired by a tree leaf, when the model bend, it creates surface that acts like a bluff body for vortex generation. Goushcha, Akaydin, Elvin, and Andreopoulos (2015) used only a thin flexible cantilever beam with piezoelectric patches to harness vortex induced vibration. In the study, it mentioned that the irregular turbulence of the flow when in contact with thin plate will generate vortex. Power output of the model depends on the velocity and closeness to the wall. Pitching angle is also a main factor in determining the power output, at small pitching angle lift force dominated while drag force dominated in larger angles.

2.3.5 Summary of Past Research

Vortex Induced Vibration started with a single cylinder system hanging onto a spring hooked to a generator. When it vibrates, the cylinder generates electricity through vibration induced by vortex wake. With this system, it is determined that with a large cross sectional and under optimum mass ratio the system can function at its maximum

efficiency. It is later found that tandem arrangement cylinders will have a better VIV performance compared to a single cylinder especially cylinders arranged in upstream and downstream with certain gap ratios, the wake complement each other creating wake galloping.

As the cylinder wake galloping method is too large and requires a lot of space in setting up the system, an elastic piezoelectric plate is used instead as VIV harvester. Due to the piezoelectric plate is only a thin plate, a large body is found to be effective in creating better vortex. A more elastic plate or a flexible model had been proved to encourage better vibration under the effect of vortex because of lower natural frequency needed. A mass installed at the tip of the cantilever plate also proved to have lowered the natural frequency of the model which lowered the vortex frequency needed to excite the model.

2.4 Piezoelectric Harvester Design

Piezoelectric plates usually have 3 independent elements within the piezoelectric coupling tensor terms, d . First, d_{15} relates towards the shear stress which is not related towards energy harvesting. On the other hand, d_{31} and d_{33} indicates types of piezoelectric plate material being used. The first subscript 3 describes that voltage is being generated along the z-axis, i.e. electrodes is being attached perpendicularly to the surface. The second subscript describes the direction of the stress being applied, 3 being parallel to the voltage line while 1 being perpendicular to the voltage direction. The piezoelectric plate type 31 is the most common cantilever types PVEH where a bend in PVEH plate creates voltage. The constitutive equations for electromechanical coupling piezoelectric materials are given by:

$$\{S\} = [s^E]\{T\} + [d]\{E\} \quad (2.5)$$

$$\{D\} = [d]^t\{T\} + [\epsilon^T]\{E\} \quad (2.6)$$

Or:

$$\{T\} = [c^E]\{S\} - [e]\{E\} \quad (2.7)$$

$$\{D\} = [e]^t\{S\} + [\varepsilon^S]\{E\} \quad (2.8)$$

where $\{T\}$ is stress vector in x, y, z, yz, xz, xy directions, $\{S\}$ is strain vector in x, y, z, yz, xz, xy directions, $\{D\}$ is electric displacement vector in x, y, z directions, $\{E\}$ is electric field vector in x, y, z directions, $[s^E]$ is compliance matrix evaluated at constant electric field, $[d]$ is piezoelectric matrix relating strain/electric field, $[\varepsilon^T] =$ dielectric matrix evaluated at constant stress, $[c^E] = [s^E]^{-1}$ is stiffness matrix evaluated at constant electric field, $[e] = [s^E]^{-1}[d]$ is piezoelectric matrix relating stress/ electric field, $[\varepsilon^S] = [\varepsilon^T] - [d]^t[s^E]^{-1}[d]$ is dielectric matrix evaluated at constant strain (Hehn & Manoli, 2014).

2.5 Structural Mechanics

Vortex induced vibration of a plate is a form of response from a forced harmonics excitation. In order to simplify the calculation, the plate is assumed to vibrate linearly in single degree of freedom. Considering the structure is an energy harvesting piezoelectric structure, a piezoelectric component should be considered (Huseyin Dogus Akaydin, Elvin, & Andreopoulos, 2010). Therefore, the general forced vibration response for a linear equation can be expressed as followed:

$$[M]\{\ddot{y}(t)\} + [C]\{\dot{y}(t)\} + [K]\{y(t)\} + [\theta]\{V(t)\} = \{F(t)\} \quad (2.9)$$

where y is the forced response, $[M]$ is the mass matrix, $[C] = \alpha[M] + \beta[K]$ is the proportional damping matrix, $[K]$ is the stiffness matrix, θ is the coupling coefficient and $V(t)$ is electrode voltage and $\{F(t)\}$ is the force excitation vector. The term $[\theta]\{V(t)\}$ is related to electrical damping and stiffness when the electrodes are connected to a resistive load, R . Eq. (2.10) shows the electromechanical output when a resistive load, R is connected.

$$-V = IR = R\theta\dot{y}(t) + RC\dot{V}(t) \quad (2.10)$$

Eq. (2.9) is re-written as:

$$[M]\{\dot{y}(t)\} + [C + C_e]\{\dot{y}(t)\} + [K + K_e]\{y(t)\} = \{F(t)\} \quad (2.11)$$

Noted that the coupling coefficient, θ and the electrical capacitance, C_p for a given dimension of piezoelectric plate, (i.e. L is length, W is width, and T is thickness T) are defined as:

$$\theta = \frac{3d_{31}LW}{4\varepsilon_{33}^T T} \quad (2.12)$$

$$C_p = \frac{\varepsilon_{33}^S LW}{T} \quad (2.13)$$

The electrical damping, C_e at frequency, ω could be expressed as:

$$C_e = \frac{RC_p \left(\frac{\theta^2}{C_p}\right)}{1 + (RC_p \omega)^2} \quad (2.14)$$

and electrical stiffness, K_e at frequency, ω could be expressed as:

$$K_e = \frac{(RC_p \omega)^2 \left(\frac{\theta^2}{C_p}\right)}{1 + (RC_p \omega)^2} \quad (2.15)$$

The flutter and lift force by vortex is undergoing harmonic excitation the force excitation matrix, $\{F(t)\}$ can be expressed in terms of excitation frequency, ω and time, t shown in Eq. (2.16).

$$\{F\} = \{P\}\cos(\omega t) \quad (2.16)$$

A solution in terms of location amplitude vector, $y(t)$ hence can be solved from Eq. (2.11) as:

$$\{y(t)\} = \frac{\{P\}\cos(\omega t)}{(K + K_e - \omega^2 M) + j\omega(C + C_e)} \quad (2.17)$$

2.6 Fluid Mechanics

Fluid mechanics is a field of study that is applied in a wide-range of applications, especially engineering field such as: heat exchanger and cooling technology, motor

vehicles' aerodynamic properties, pumps, turbines, valves and nozzles' optimization, air conditioning and ventilation of buildings, etc.

Although under different areas listed above, different fluid mechanics considerations and derivation is needed to complete the task, but fundamental fluid mechanics equations knowledge are essential in all the areas involved. The main concepts that can be diverted into solving specific areas' fluid problems are conservation law for mass, momentum, energy, forces and etc. (Durst, 2008).

2.6.1 Fluid Forces over Bluff Splitter Body

When fluid flow passes through a bluff body, the fluid tends to exert forces and moments onto the bluff body (Cengel & Cimbala, 2013). Lift and drag are the main forces exerted onto the model. Drag force consists of pressure, friction and shear that acted along the flow direction while pressure and shear force normal to the flow is lift force acting on the body. These forces will contribute towards the movement of the body in any direction with more dominant forces acting on it. The pressure and shear stress acting on the body are used to derive the drag and lift force which can be expressed with Figure 2.6 and the following Equations (2.18) and (2.19):

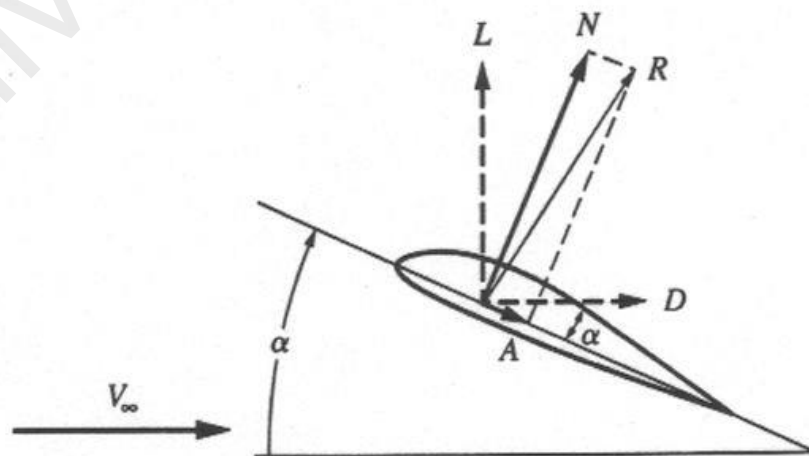


Figure 2.6: Force Components Acting on a Body When Flow Passes Through (Source: www.aerospaceweb.org)

$$F_D = \int (-N \cos \alpha + \tau \sin \alpha) dA \quad (2.18)$$

$$F_L = - \int (N \sin \alpha + \tau \cos \alpha) dA \quad (2.19)$$

where F_D is drag force, F_L is lift force, N is normal force, τ is the shear force, α is the angle to wind direction and A is the chord length

The drag and lift force strongly dependant on the velocity, fluid density, size, shape and orientation of a certain body. It is easier to show the relative of all these parameters with a non-dimensional number of drag and lift coefficient as shown in Equations (2.20) and (2.21) as shown below referring to the figure above:

$$C_D = \frac{F_D}{\frac{1}{2}\rho U^2 A} \quad (2.20)$$

$$C_L = \frac{F_L}{\frac{1}{2}\rho U^2 A} \quad (2.21)$$

where C_D is the coefficient of drag, C_L is the coefficient of lift, ρ is the density, U is the flow velocity and A is the chord length.

2.6.2 The Navier-Stokes Equation

The general derivation of conservation of mass, momentum and energy equation is used to simplified and solve into Navier-Stokes Equation each shown in Equation 2.22, 2.23 and 2.24 respectively.

$$\nabla \cdot \rho \mathbf{u} + \frac{\partial \rho}{\partial t} = 0 \quad (2.22)$$

$$\rho \left[\frac{\partial U}{\partial t} + \nabla \cdot (U \otimes U) \right] = -\nabla p - \nabla \cdot \tau + \rho g \quad (2.23)$$

$$\frac{\partial \rho E}{\partial t} + \nabla \cdot (\rho U E) - \frac{\partial p}{\partial t} = -\nabla \cdot (\tau \cdot U) + \rho U g + \nabla \cdot (k \nabla T) \delta V + S_E \quad (2.24)$$

where \mathbf{u} is the velocity vector, ρ is the density, t is the time, U is the flow velocity, p is the pressure force, τ is the shear force, g is the gravitational force, E is the internal

energy, k is the thermal conductivity constant, T is the temperature, V is the volume and S_E is the surface energy.

In conservation of momentum equation/ Cauchy equation of Equation 2.18, the shear force, τ is expressed as molecular stress tensor, τ_{ij} which is an unknown introduced as an input per unit area per unit time without knowing the specific values. The stress tensor consists of nine components but six are independent (τ_{11} , τ_{12} , τ_{13} , τ_{22} , τ_{23} , and τ_{33}) due to symmetry $|\tau_{ij}| = |\tau_{ji}|$. There is a total of 10 unknowns including the six stress tensor mentioned above, three velocity components U_1 , U_2 , and U_3 and pressure component, P . The total 4 equations consisting of 3 momentum equations and 1 continuity equation is not enough to solve the equation consisting of 10 unknowns.

In order to solve this equation, the viscous stress tensor needs to be converted into viscosity and velocity form after that solve in terms of direction component, x and time, t by assuming it to be flowing as Newtonian fluid and it is incompressible and isothermal yielding constant density, ρ , dynamic viscosity, μ , and kinematic viscosity, ν (Kundu, 1990).

$$\frac{\partial \tau}{\partial x_i} = -\mu \left(\frac{\partial^2 U_j}{\partial x_i^2} \right) \quad (2.25)$$

When viscosity, μ in Equation (2.25) is substitute into momentum equation (2.23), it yields:

$$\rho \left(\frac{\partial U_1}{\partial t} + U_1 \frac{\partial U_1}{\partial x_1} + U_2 \frac{\partial U_1}{\partial x_2} + U_3 \frac{\partial U_1}{\partial x_3} \right) = \rho g - \frac{\partial p}{\partial x_1} + \mu \left(\frac{\partial^2 U_1}{\partial x_1^2} + \frac{\partial^2 U_1}{\partial x_2^2} + \frac{\partial^2 U_1}{\partial x_3^2} \right) \quad (2.26)$$

$$\rho \left(\frac{\partial U_2}{\partial t} + U_1 \frac{\partial U_2}{\partial x_1} + U_2 \frac{\partial U_2}{\partial x_2} + U_3 \frac{\partial U_2}{\partial x_3} \right) = \rho g - \frac{\partial p}{\partial x_2} + \mu \left(\frac{\partial^2 U_2}{\partial x_1^2} + \frac{\partial^2 U_2}{\partial x_2^2} + \frac{\partial^2 U_2}{\partial x_3^2} \right) \quad (2.27)$$

$$\rho \left(\frac{\partial U_3}{\partial t} + U_1 \frac{\partial U_3}{\partial x_1} + U_2 \frac{\partial U_3}{\partial x_2} + U_3 \frac{\partial U_3}{\partial x_3} \right) = \rho g - \frac{\partial p}{\partial x_3} + \mu \left(\frac{\partial^2 U_3}{\partial x_1^2} + \frac{\partial^2 U_3}{\partial x_2^2} + \frac{\partial^2 U_3}{\partial x_3^2} \right) \quad (2.28)$$

Simplifying Cauchy's momentum equation into Navier-Stokes Equation reduces the amount of unknowns in the equation. By changing the variables, the equations have

only 4 unknowns which are the velocity component (U_1 , U_2 , and U_3) and pressure component, P . Navier-Stokes Equation is the basic equation used to derive turbulence model used in CFD solver of any numerical simulation mentioned in the following section.

2.7 Numerical Simulation

Numerical flow simulation had been the breakthrough for complex fluid engineering solutions in the past decade. Examples of flow simulation usage were flow over airfoil, vehicles, buildings, and stacks, heating and cooling of ventilation system, reservoir flow system and pipeline system. Rapid growth of computing technology allows implementation of numerical flow simulation from simple pipeline flow cases to complicated cases such as prediction of weather. Computational fluid simulations nowadays are able to grant user the access to study the interaction of fluid with other area of interests such as mechanical and chemical. The cases of dam wall breaking due to water pressure forces, vibrations due to flow separation, combustion process and many more can be simulated (Griebel, Dornseifer, & Neunhoeffler, 1997).

High computing capacity and fast computing speed had been the essential in the wide spread of Computational Fluid Dynamics (CFD) usage. With the use of computational fluid dynamics, engineers can access the effects of geometry on a flow, changes in flow when design changes or flow characteristic on a structure with lower engineering cost. In modern fluid problem solving involves both experimental and CFD analysis, global properties such as lift, drag pressure drop or power can be determined experimentally but specific values such as shear stress, velocity and pressure profile, surface pressure is obtained through CFD analyses. CFD advancement allows user to run simulation with smaller grids and faster computing time reducing design cycle phase through specific parametric control.

Although CFD analysis provides many advantages for solving many modern problems, it has also some shortcomings. CFD can predict laminar flows easily and accurately, but turbulent flow will be harder to solve due to its randomness nature. In order to solve turbulent flow, a turbulence model had to be implemented. Turbulence model implies extra assumptions and values to suit each case that is being solved. Some cases need special turbulence model but a general turbulence model such as $k-\varepsilon$, $k-\omega$ and SST is able to yield reasonable results.

2.7.1 Computational Fluid Dynamics Methods Approach

The computational fluid dynamics utilizes three main approaches namely finite difference method, finite element method and finite volume method each with its own discrete exponential equation (Ferziger & Peric, 2012).

Finite difference method uses a time-distance grid of node paired with a truncated Taylor series. This method predicts a particular node's condition at a time step by referring to the conditions of adjacent time step at previous time step.

Finite Element Method (FEM) which initially is developed for structural analysis is also used for fluid problem solving because it provides better solutions towards unstructured mesh solving. FEM has an advantage in solving complex boundary geometries, it also has a higher accuracy compare to finite difference method. But this comes with a cost of higher complexity of equations used. The current investigation involves the use of this solving method

Finite Volume Method (FVM) put together the best attributes of FDM and FEM whereby it can simulate complex boundary and accurately model governing equation for each cell while maintaining finite difference relationship to represent governing differential equations.

2.7.2 Grid Generation/Meshing

In CFD analysis, meshing is one of the most important steps to be carried out. A mesh or a grid determines the cell area in which the flow variables such as velocity and pressure are calculated throughout the computational domain. Meshing grid can be divided into two main types which is structured and unstructured grid. Nodes and elements are the basic quantification of a cell statistic that determines the computational time. Larger amount of nodes and elements will cost more time in calculation.

Structured grid is made up of 4 sided planar cells in 2-D model and volumetric cells in 3-D model. A cell may be slightly distorted but it still can be mapped onto (i, j, k) indices. On the other hand, unstructured grid referred as triangle or quadrilateral cells in 2-D domain while tetrahedrons and hexahedrons cells are presented in 3-D domain. Unstructured grid usually has an advantage in being easier in creating better mesh when it involves complex geometry, but structured grid produces fewer cells in the same area of model which helps in saving computational time. Structured grid with the same amount of cells compared to unstructured grid has a higher resolution (Ho-Le, 1988).

To determine the reliability of the mesh, there are different quantifications unit exists such as aspect ratio, orthogonality, mesh skewness and many more. Mesh skewness is the more general standard to judge the quality of a mesh. Cell quality will affect the solution convergence problem and accuracy in numerical simulation results. Skewness is defined as the rate of distortion away from symmetry. Skewness in 2-dimension can be determined with equiangular skewness equation as shown below:

$$Q_{EAS} = MAX \left(\frac{\theta_{max} - \theta_{equal}}{180^\circ - \theta_{equal}}, \frac{\theta_{equal} - \theta_{min}}{\theta_{equal}} \right) \quad (2.29)$$

where Q_{EAS} is the skewness, θ_{max} is the maximum cell angle, θ_{min} is the minimum cell angle, and θ_{equal} is the equal cell angle

Skewness of a model can be determined to be between $0 < Q_{EAS} < 1$. The skewness nearer to 0 is said to be better compared with nearer to 1. Mesh with skewness more than 0.95 will have a higher probability to face divergence and solution error (Wendt, 2008).

Meshing is undeniably the hardest part in conducting a CFD analysis as the quality of the mesh directly affects the accuracy of the solution. Structured grid and unstructured grid should be applied at the correct areas to maximize the quality of mesh as most CFD meshing software like Gambit and ICEM provides multi-block analysis. A model can be split into different regions known as blocks or zones. A hybrid grid is generated when structured mesh is applied in regions with straight edges without small angle sharp ends while the others will be meshed with unstructured mesh. The goal of this approach is to generate cells that are not highly skewed and it is necessary in complex geometry. A hybrid grid also can be applied when the flow near a wall boundary is important, therefore smaller size structured mesh needs to be placed near the wall.

2.7.3 Turbulent CFD Calculations

Simulations of turbulent flow are much complex compared to laminar flow. Turbulent flow field in real life contains 3-dimensional unsteady and random turbulent eddies such as swirling and vortices. Direct Numerical Simulation (DNS) is made to simplify the unsteady motion of all scales. The problem with DNS approach arises because the turbulent flow unsteadiness of size and time scales vary differently with the largest and the smallest turbulence eddies having very large value of difference in between changes according to Reynolds Number. In order for DNS to work accurately, the grid has to be extremely fine and 3-dimensional, coupled with large computational cost, i.e. with large computers and long computational time. Hence this method is not practical even with very good computers advancement in the future (Moin & Mahesh, 1998).

It is important to simplify the complex simulation of turbulent flow fields, some level of assumptions are introduced to simplify the equations used as mentioned below. Large Eddy Simulation (LES) is the simplified version of DNS. In LES simulation, the larger turbulent eddies are being solved while the smaller eddies are being modelled. The smaller turbulent eddies in these flows are assumed to be isotropic, i.e. the smaller turbulent eddies are independent of coordinate system and orientation and always behave statistically similar in every region of flow. LES significantly reduces the computational cost needed to solve an unsteady flow as small eddies are eliminated, but it still needs large amount of computational resources (Zhiyin, 2015).

To overcome the shortcomings of LES, turbulence model was introduced to improve the computational cost while maintaining decent result produced. In turbulence model, it does not resolve the turbulence eddies, instead a mathematical model is used to describe the enhanced mixing and diffusion caused by turbulent eddies. When solving with turbulence model, the case is considered to be steady incompressible flow by implying the steady Navier-Stokes Equation but enhanced by improving the equation to become Reynolds Averaged Navier-Stokes equation.

2.7.4 Turbulence Model

Turbulence model were mentioned to be the assumptions and approximation inserted into Reynolds Averaged Navier-Stokes equation. Depending on the degree of approximations involve, the equation system can be divided into the following: algebraic models, one equation models, two equation models and Reynold Stress Model. Algebraic model, one equation model and two equation model are included as Linear Eddy Viscosity Model. These turbulence models modelled the Reynolds Stress tensor from Reynolds Averaging of Navier Stokes equation by a linear constitutive relationship

2.7.4.1 Reynolds Averaging of Navier-Stokes Equations (RANS)

Reynolds Average Navier Stokes equation derives from the Navier Stokes Equation by separating the flow variable, such as U into mean component, \bar{U} and fluctuating term, U' .

$$U = U' + \bar{U} \quad (2.30)$$

Taking Navier-Stokes Equation (2.27), the density variable is removed from the equation:

$$\frac{\partial U_1}{\partial t} + \frac{\partial}{\partial x_2} (U_1 U_2) = g - \frac{1}{\rho} \frac{\partial p}{\partial x_1} + \nu \left(\frac{\partial^2 U_1}{\partial x_1^2} \right) \quad (2.31)$$

where U is the flow variable, t is the time component, x is the directional component, g is the gravitational force, and p is the pressure component

Replacing U with Equation (2.30) and take the time average of each variable yields:

$$\frac{\partial \overline{U_1 + U_1'}}{\partial t} + \frac{\partial}{\partial x_2} [\overline{(U_2 + U_2')(U_1 + U_1')}] = -\frac{1}{\rho} \frac{\partial \overline{p + p'}}{\partial x_1} + \nu \frac{\partial^2 \overline{U_1 + U_1'}}{\partial x_2^2} \quad (2.32)$$

$$\frac{\partial \bar{U}_1}{\partial t} + \frac{\partial}{\partial x_2} [\overline{U_1 U_2} + \overline{U_1 U_2'} + \overline{U_1' U_2} + \overline{U_1' U_2'}] = -\frac{1}{\rho} \frac{\partial \bar{p}}{\partial x_1} + \nu \frac{\partial^2 \bar{U}_1}{\partial x_2^2} \quad (2.33)$$

Since \bar{U} is a constant, time averaging of fluctuating term and time averaging term product will yield 0, creating Equation (2.34).

$$\frac{\partial \bar{U}_1}{\partial t} + \bar{U}_2 \frac{\partial \bar{U}_1}{\partial x_2} = -\frac{1}{\rho} \frac{\partial \bar{p}}{\partial x_1} + \nu \frac{\partial^2 \bar{U}_1}{\partial x_2^2} - \frac{\partial}{\partial x_2} \overline{U_1' U_2'} \quad (2.34)$$

$$\frac{\partial \bar{U}_1}{\partial t} + \bar{U}_2 \frac{\partial \bar{U}_1}{\partial x_2} = \frac{1}{\rho} \frac{\partial}{\partial x_2} (-\bar{p} \delta_{ij} + \mu S_{ij} - \rho \overline{U_1' U_2'}) \quad (2.35)$$

From Equation (2.30), the term $-\rho \overline{U_1' U_2'}$ represents the added stress on the fluid or called as Reynolds Stress tensor term. In Linear Eddy Viscosity model, the equation is modelled by linear constitutive relationship with mean flow straining field shown as:

$$-\rho \overline{U_1' U_2'} = 2\mu S_{ij} - \frac{2}{3}\rho k \delta_{ij} \quad (2.36)$$

2.7.4.2 Large Eddy Simulation (LES)

Large eddy simulation (LES) is a popular technique in solving turbulent flows. LES allows solving of large eddies explicitly while implicitly taking into consideration of small eddies in a single calculation by using subgrid-scale model (SGS). In RANS model above, flow variable in Equation 2.30 is solved separately where \bar{U} is the resolvable scale part and U' is the subgrid scale part. However in LES, the mesh grid is use as a filter (i.e. box filter) to perform non-explicit filtering. This model introduces decomposed of pressure variable $p = \bar{p} + p'$ and Equation 2.30 into Equation 2.31 yielding:

$$\frac{\partial \bar{U}_1}{\partial t} + \frac{\partial}{\partial x_2} (\bar{U}_1 \bar{U}_2) = -\frac{1}{\rho} \frac{\partial \bar{p}}{\partial x_1} + v \left(\frac{\partial^2 \bar{U}_1}{\partial x_1^2} \right) + \frac{1}{\rho} \frac{\partial \tau_{12}}{\partial x_2} \quad (2.37)$$

The term, $\frac{\partial \tau_{12}}{\partial x_2}$ due to non-linear advection term is then solved using SGS model using:

$$\tau_{12} - \frac{1}{3} \delta_{12} \tau_{33} = -2\mu_t S_{12} \quad (2.38)$$

Where μ_t is the resolved dynamic viscosity and S_{12} is the rate of strain tensor for the resolved scale which is defined as:

$$S_{12} = \frac{1}{2} \left(\frac{\partial \bar{U}_1}{\partial x_2} + \frac{\partial \bar{U}_2}{\partial x_1} \right) \quad (2.39)$$

Substituting back into Equation (2.37) yields the simplified filtered equation of:

$$\frac{\partial \bar{U}_1}{\partial t} + \frac{\partial}{\partial x_2} (\bar{U}_1 \bar{U}_2) = -\frac{1}{\rho} \frac{\partial \bar{p}}{\partial x_1} + \frac{\partial}{\partial x_2} \left([v + v_t] \frac{\partial \bar{U}_1}{\partial x_2} \right) \quad (2.40)$$

where v_t is the sub-grid scale turbulent viscosity.

In Wall-Adapting Local Eddy-Viscosity model, shear stress tensor and rotation tensor is taken into account based on the square of velocity gradient tensor (Weickert, Teike, Schmidt, & Sommerfeld, 2010). The turbulent dynamic viscosity is defined as:

$$\mu_t = \rho \Delta_s^2 \frac{(S_{12}^d S_{12}^d)^{3/2}}{(S_{12} S_{12})^{5/2} + (S_{12}^d S_{12}^d)^{5/4}} \quad (2.41)$$

$$\Delta_s = C_w V^{1/3} \quad (2.42)$$

$$S_{12}^d = \frac{1}{2}(\bar{g}_{12}^2 + \bar{g}_{21}^2) - \frac{1}{3}\delta_{12}\bar{g}_{33}^2 \quad (2.43)$$

$$\bar{g}_{12}^2 = \frac{\partial \bar{U}_1}{\partial x_2} \quad (2.44)$$

where V is the volume and wall constant, $C_w = 0.325$.

2.7.4.3 Algebraic Model

Algebraic model equation is also known as zero-equation model which is a model that does not require any solution of extra equations to be able to solve. This model equation calculates solution directly from flow variables. As this turbulence model does not take into account historical effects, the model only can calculate simple flow with simple geometry or can be used as startup initial calculations while more complicated flows, the turbulence model will have difficulties in calculating it.

2.7.4.4 One Equation Turbulence Model

One equation turbulence model solves only one turbulent equation which usually is the turbulent kinetic energy equation. The most common one equation model is the Prandtl One Equation model solving with kinematic eddy viscosity (D.C. Wilcox, 2004).

One equation model is an economic and accurate turbulence model to work with if the problem is not too complicated. This model is suitable especially for wall-

bounded flows and flow over wings. Problem with massive separated flow, shear flow and complex internal flow is proven unable to be handled accurately by the model.

2.7.4.5 k - ε Turbulence Model

Two equation models involve solving 2 equations, in this case equations for k and ε together with eddy-viscosity stress-strain relationship. The dissipation term, ε is derived from the Navier-Stokes equation, but the numbers of unknown terms are very large and involve double correlations of fluctuating velocities, and gradients of fluctuating velocities and pressure. Hence it is derived to include production terms that are similar to the derivation of k . The k - ε equation after including $\overline{U_1 U_2}$ and $\frac{\partial \overline{U_1}}{\partial x_2}$ terms is shown in Equation 2.45 below (Versteeg & Malalasekera, 2007).

$$\frac{\partial}{\partial t}(\rho k) + \frac{\partial}{\partial x_1}(\rho k U_1) = \frac{\partial}{\partial x_2} \left[\left(\mu + \frac{\mu_t}{\sigma_k} \right) \frac{\partial k}{\partial x_2} \right] + P_k - \rho \varepsilon + P_B \quad (2.45)$$

where k is the turbulent kinetic energy and ε is the turbulent dissipation.

$$\frac{\partial}{\partial t}(\rho \varepsilon) + \frac{\partial}{\partial x_1}(\rho \varepsilon U_1) = \frac{\partial}{\partial x_2} \left[\left(\mu + \frac{\mu_t}{\sigma_\varepsilon} \right) \frac{\partial \varepsilon}{\partial x_2} \right] + C_{1\varepsilon} \frac{\varepsilon}{k} (P_k + C_{3\varepsilon} P_B) - C_{2\varepsilon} \rho \frac{\varepsilon^2}{k} \quad (2.46)$$

$$\text{Production term, } P_k = -\rho \overline{U_1' U_2'} \frac{\partial U_2}{\partial x_1} \quad (2.47)$$

$$\text{Turbulent viscosity, } \mu_t = \rho C_\mu \frac{k^2}{\varepsilon} \quad (2.48)$$

$$\text{Buoyancy Production term, } P_B = \beta g_1 \frac{\mu_t}{Pr_t} \frac{\partial T}{\partial x_1} \quad (2.49)$$

$$\text{Coefficient of Thermal Expansion, } \beta = -\frac{1}{\rho} \left(\frac{\partial \rho}{\partial T} \right)_p \quad (2.50)$$

The coefficients displayed above each holds the value,

$$C_{1\varepsilon} = 1.44, C_{2\varepsilon} = 1.92, C_\mu = 0.09, \sigma_k = 1.0, \sigma_\varepsilon = 1.3$$

A $k-\varepsilon$ model is a simple model that can handle more complicated problem than one equation model. It converges easily and produces reasonable predictions in many flows, but it has poor performance in swirling, rotating, strong separation, asymmetric jets and many more. It also needs to be implemented only in fully turbulent flow with wall function.

2.7.4.6 Standard $k-\omega$ Turbulence Model

$k-\omega$ is one of the more robust and common turbulence model used in flow simulation where ω is the specific rate of dissipation. Similar to $k-\varepsilon$ turbulence model, the $k-\omega$ turbulence model also includes 2 transports equation including turbulent kinetic energy, k and specific dissipation, ω . Wilcox is the person that discovers this method as derived below (David C Wilcox, 1988).

$$\frac{\partial k}{\partial t} + U_j \frac{\partial k}{\partial x_j} = \tau_{ij} \frac{\partial U_i}{\partial x_j} - \beta^* k \omega + \frac{\partial}{\partial x_j} \left[(v + \sigma^* v_T) \frac{\partial k}{\partial x_j} \right] \quad (2.51)$$

$$\frac{\partial \omega}{\partial t} + U_j \frac{\partial \omega}{\partial x_j} = \alpha \frac{\omega}{k} \tau_{ij} \frac{\partial U_i}{\partial x_j} - \beta \omega^2 + \frac{\partial}{\partial x_j} \left[(v + \sigma v_T) \frac{\partial \omega}{\partial x_j} \right] \quad (2.52)$$

Closure Coefficients and Auxiliary Relations listed below:

$$\alpha = \frac{5}{9}; \beta = \frac{3}{40}; \beta^* = \frac{9}{100}; \sigma = \frac{1}{2} = \sigma^*; \varepsilon = \beta^* \omega k$$

A $k-\omega$ turbulence model provides better accuracy in computing low Reynolds number effects, compressibility and shear flow shedding due to its better near-wall predictions. Other than that, it suffers almost the same drawback as $k-\varepsilon$ turbulence model (Cable, 2009).

2.7.4.7 SST $k-\omega$ Turbulence Model

Shear Stress Transport (SST) equation is also a two equation eddy viscosity model that is most commonly used and considered to be the best turbulence model to decently predict most flows. In SST turbulence model, it combines the advantage displayed by

both $k-\varepsilon$ and $k-\omega$ turbulence models. The $k-\omega$ turbulence model is used when solving the inner parts of the boundary layer making the model directly usable all the way down to the wall through viscous sub-layer. A $k-\varepsilon$ turbulence is switched when the flow behaves like a free stream away from the boundary layer. Therefore, by using SST Turbulence model, it can calculate Low Reynolds number turbulence flow without any wall functions and prevent over-prediction of inlet free-stream turbulence properties (Menter, 1994).

2.7.4.8 Reynolds Stress Turbulence Model

Reynolds-Stress Turbulence Model is higher level and more complicated turbulence model compared to the other models listed above. In Reynolds Stress Turbulence model, the isotropic eddy viscosity assumption is not applied and each Reynold Stress is solved independently. The transport equations are obtained by deriving Reynolds averaging the product of momentum equations with fluctuating property (Launder, Reece, & Rodi, 1975).

In ANSYS CFX the Reynolds Stress model is based on ε -equation. The transport equation is solved as follows.

$$\begin{aligned} \frac{\partial \overline{\rho U_1' U_2'}}{\partial t} + \frac{\partial}{\partial x_3} (U_3 \overline{\rho U_1' U_2'}) = & - \frac{\partial}{\partial x_k} [\overline{\rho U_1' U_2' U_3'} + \overline{p'(\delta_{23} U_1' + \delta_{13} U_2')}] + \\ \frac{\partial}{\partial x_3} \left[\mu \frac{\partial}{\partial x_3} (\overline{U_1' U_2'}) \right] + P_{12} + P_{12,b} + \Phi_{ij} - \frac{2}{3} \delta_{ij} \rho \varepsilon - 2 \rho \Omega_3 (\overline{U_2' U_m'} \varepsilon_{13m} + \\ \overline{U_1' U_m'} \varepsilon_{23m}) \end{aligned} \quad (2.53)$$

The exact equation can be expressed alternatively as:

$$R_{12} = D_{T,12} + D_{L,12} + P_{12} + B_{12} + \Phi_{12} - \varepsilon_{12} + F_{12}$$

$$\text{Exact Production term is express as } P_{ij} = -\rho \overline{U_1 U_3} \frac{\partial u_2}{\partial x_3} - \rho \overline{u_j u_k} \frac{\partial u_1}{\partial x_3} \quad (2.54)$$

$$\text{Production due to buoyancy, } P_{ij,b} = B_{ij} - C_{buo} \left(B_{ij} - \frac{1}{3} B_{kk} \delta_{ij} \right) \quad (2.55)$$

$$B_{ij} = g_i b_j + g_j b_i \quad (2.56)$$

If Boussinesq buoyancy model is used, then

$$b_i = \frac{\mu_t}{\sigma_p} \beta \frac{\partial T}{\partial x_i} \quad (2.57)$$

Otherwise the model is treated as full buoyancy model based on density difference,

$$b_i = \frac{\mu_t}{\sigma_p} \beta \frac{\partial T}{\partial x_i} \quad (2.58)$$

One of the most important terms in Reynolds Stress model is Pressure-strain terms, Φ_{ij}

$$\Phi_{ij} = \Phi_{ij,1} + \Phi_{ij,2}, \quad \Phi_{ij,1} \text{ is slow term and } \Phi_{ij,2} \text{ is the fast term}$$

$\Phi_{ij,1}$ and $\Phi_{ij,2}$ is defined based on anisotropy tensor a_{ij} , mean strain rate tensor, S_{ij} and vorticity tensor, Ω_{ij} .

$$\Phi_{ij,1} = -\rho \varepsilon \left[C_{s1} a_{ij} + C_{s2} \left(a_{ik} a_{kj} - \frac{1}{3} a_{mn} a_{mn} \delta_{ij} \right) \right] \quad (2.59)$$

$$\begin{aligned} \Phi_{ij,2} = & -C_{r1} P a_{ij} + C_{r2} \rho k S_{ij} - C_{r3} \rho k S_{ij} \sqrt{a_{mn} a_{mn}} + C_{r4} \rho k \left(a_{ik} S_{jk} + a_{jk} S_{ik} - \right. \\ & \left. \frac{2}{3} a_{kl} S_{kl} \delta_{ij} \right) + C_{r5} \rho k \left(a_{ik} \Omega_{jk} + a_{jk} \Omega_{ik} \right) \end{aligned} \quad (2.60)$$

$$\text{Anisotropy tensor, } a_{ij} = \frac{\overline{u_i u_j}}{k} - \frac{2}{3} \delta_{ij} \quad (2.61)$$

$$\text{Mean Strain Rate tensor, } S_{ij} = \frac{1}{2} \left(\frac{\partial u_i}{\partial x_j} + \frac{\partial u_j}{\partial x_i} \right) \quad (2.62)$$

Reynolds Stress with the more complicated prediction is able to precisely predict most comp the large amount of equations, it is costly and inefficient into simulate simple flow. Speziale-Sarkar-Gatski (SSG) Reynolds Stress is an approach towards the normal Reynolds Stress model which makes it more accurate for homogeneous turbulence and

subsequently simulates most flows especially swirling flows more accurately (Tropea, Jakirlic, Heinemann, Henke, & Hönliger, 2007). The pressure strain term is similar to a conventional Reynolds Stress Model but the coefficient length scale is written by the standard transport equation for dissipation rate, ϵ as $C_{s1} = 0.9$; $C_{s2} = 0.65$; $C_{r1} = 1.7$; $C_{r2} = 1.05$; $C_{r3} = 0.8$; $C_{r4} = 0.625$; $C_{r5} = 0.2$

2.7.5 Fluid-Structure Interaction

Fluid-Structure Interaction (FSI) analysis is a robust approach that is widely used and applied in modern design analyses. This method is able to decently predict the motion of a certain structure under the influence of fluid flow or the effect of a structure to the fluid flow. FSI analysis is a multi-field simulation done with two separate solvers: Computational Fluid Dynamics (CFD) module for fluid and Finite Element Analysis (FEA) for structure (Schmucker, Flemming, & Coulson, 2010). The two modules will then exchange data through an effective boundary area connecting both fluid and structure.

Depending on the coupling approach, it will determine the data exchange between solvers. In one way coupling, fluid pressure induced is transferred to calculate the deformation of the structure. On the contrary, two way coupling sees the exchange of structure deformation back to the fluid solver in the same iteration. Two-way system coupling is more accurate, especially with large deformation of structure. There are mainly 2 types of two-way system coupling in FSI analysis, i.e. loosely coupled and strong coupled simulation. Within one time step strong couple situation, it will run until the solutions converged but weak couple situation will not take into account the convergence of the solution before moving on to the next time step (Benra, Dohmen, Pei, Schuster, & Wan, 2011). A schematic diagram showing 1-way and 2-way FSI coupling is presented below in Figure 2.7.

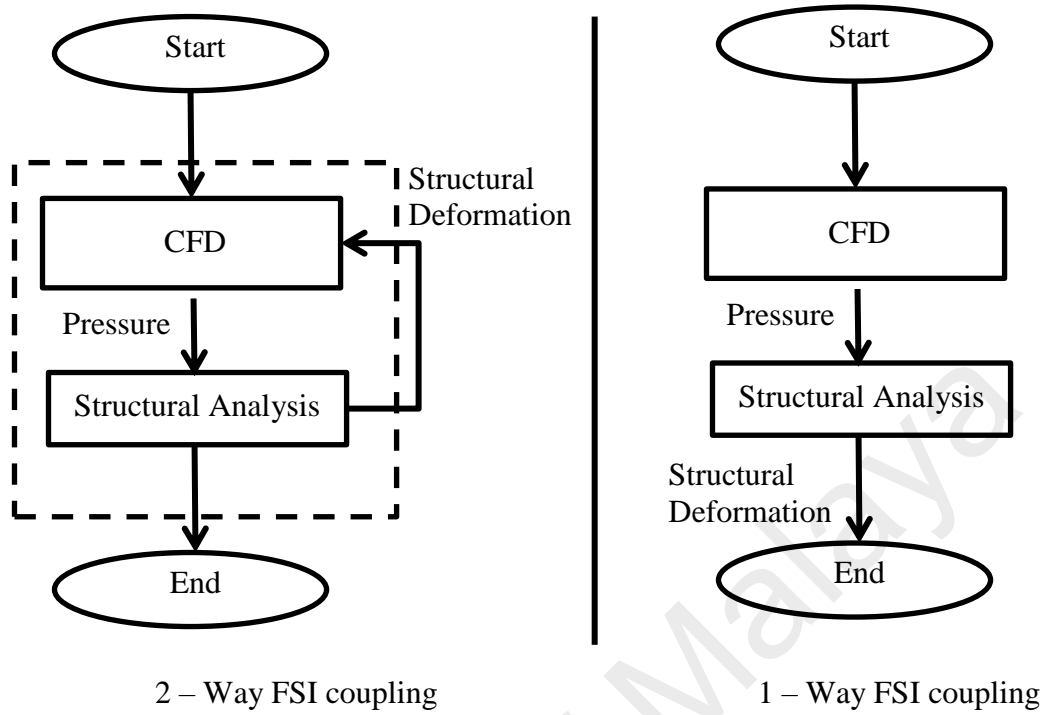


Figure 2.7: Schematic Flow Diagram of 1-way and 2-way FSI Coupling

CHAPTER 3: METHODOLOGY

3.1 Introduction

The research methods that were performed to obtain the desired objectives in Section 1.4 are discussed in this chapter. The main objective of this research is to understand the effect of parameters such as wind speed, size of the bluff splitter body or elastic plate and bluff splitter body design on vortex induced vibration. In addition, the enhancement of vibrational performance a coupled bluff splitter body and elastic plate model under the influence of vortex is investigated.

Computational method is the main procedure used in this research. After the model dimensions and simulation settings are used based on a thorough validation with the results of previous research. A validated computational method is able to provide decent predictions on the force applied, velocity, displacement, etc. Research cost can thus be reduced while maintaining the accuracy of the obtained results compared to any experimental work. Computational method reduces the engineering cost for multiple parameters and settings to be tested out in preliminary benchmark phase prior to the actual prototyping phase.

This research will be divided into six sections in order to achieve the three objectives set in Section 1.4 with two sections contributing to each objective. The first objective requires investigating the effect of wind speed on the VIV of the model. The first section used a model consists of a less flexible PVEH plate coupled with a bluff splitter body undergo a higher wind speed while the second section uses a more flexible elastic plate coupled with a bluff splitter body running at lower wind speed. The second objective is to investigate the effect on VIV with the change in structural model's aspect ratio. In this objective, the first section is by changing the width of the bluff splitter body while the second section is by changing the length of the elastic plate. The last

objective is to investigate the effect of VIV with the change in geometry of the bluff splitter body. In the first section, different shapes of bluff splitter body is applied with a fixed length of elastic plate whilst in the second section different angle of trapezoidal bluff splitter body is used with the same length of elastic plate. The overview of software used and methods are described in section 3.1 below while the detailed model design and characteristic, fluid structure interaction analysis parametric settings and procedure are listed in section 3.2.

3.2 Methodology Overview

Throughout this research, different methods were carried out in different phase to achieve different goals in order to obtain the desired results. The methods that were being practiced in this research were CAD modelling, mesh generation, numerical computational simulation analysis and data extraction and analysis.

3.2.1 CAD Modelling

Computational Aided Modelling software is used to draw all the structural models for these simulation analyses. The software used is SolidWorks 2012 as it is more robust in 3-dimensional computer aided design and modeling (CAD/CAM) compared to other competitors. CAD/CAM software had been widely used in different engineering fields ranging from research and development to industrial design, the robust functions enables user to execute different complex tasks while saving time and cost in design works.

Fluid domain that exists during CFD simulation was also designed using CAD software. ANSYS DesignModeler 15.0 is the program utilized in this research to draw the fluid domain region. During domain size determination for vortex problems, the distance of the domain wall and the inlet to the model should be more than 5 times the

width of the model. Outlet of the domain to the flow separation tip of the model should be at least 10 times the width of the model (Tominaga et al., 2008).

3.2.2 Meshing

Meshing or grid generation is an important step in dividing the geometrical domain into smaller elements in order to carry out finite element analysis or computational fluid dynamics analysis. ANSYS ICEM 15.0 meshing module is the program used to generate the mesh in this research. As the all the models involved are 3D, the grids generated consist mostly of tetrahedral and prisms mesh. The resolution of the generated mesh greatly affects the accuracy of the results generated.

3.2.3 Fluid-Structure Interaction Analysis

Fluid-structure interaction (FSI) is a computational method commonly used to solve coupled fluid and structure problems nowadays as per mentioned in Section 2.6. In this research, fluid-structure interaction (FSI) analysis is done with ANSYS 15.0 software modules. ANSYS 15.0 is chosen for the powerful solver engine it possess and user friendly interface. FSI analysis utilizes the combination of direct simulation analysis (DNS) or known as Computational Fluid Dynamics (CFD) simulation and structural dynamic analysis. ANSYS CFX 15.0 is the CFD module applied because it provides easier manipulation and settings control over 3-D model. ANSYS Mechanical APDL 15.0 is used to simulate the structural dynamics under the influence of fluid flow.

ANSYS 15.0 is also a powerful tool in post-processing actions. Result parameters such as velocity and pressure can be represented in streamlines and contour using ANSYS CFD-Post 15.0 module. Graphs could be plotted and analyzed by conducting Fast-Fourier Transform (FFT) if the frequency of a graph is important parameters to be considered.

3.3 CAD Model Design of Structural Model and Domain

The coupled bluff splitter body and plate structural CAD model was designed using SolidWorks program. The fluid domain used by CFD simulation was drawn using ANSYS integrated DesignModeler.

3.3.1 Coupled Thin Bluff Splitter Body and PVEH plate model

In the first section of first objective, the structural model applied was a Piezoelectric Energy Harvester (PVEH) coupled with a rectangular aluminum bluff splitter body as shown in Figure 3.1. The PVEH plate used in this research was the piezoelectric bimorph model proposed by Huang et al. which consists of 3 layers, where the top and bottom layer is made of PSI-5A4E, an industry type 5A (Navy Type II) piezoceramic while the middle layer is a brass shim layer served as a reinforcement layer. The layers are held together with glue but the thickness of the glue is ignored. Thus the PZT and brass model is bonded with fixed boundary condition. This PVEH plate was then mounted with a cantilever boundary condition onto the fixed boundary condition bluff splitter body. The detailed dimension and material properties of the structural model was displayed in Table 3.1.

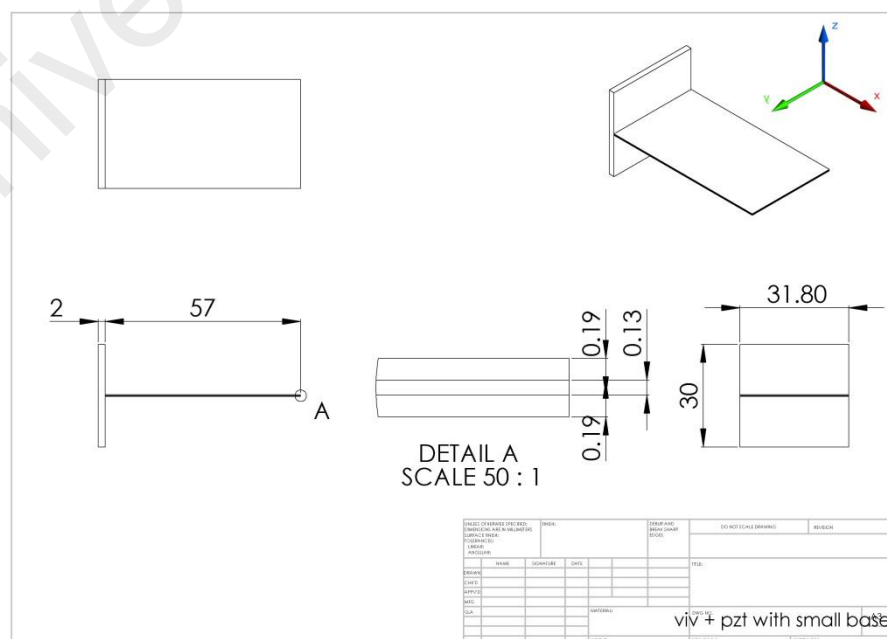


Figure 3.1: CAD Design of Bluff Splitter Body-PVEH Plate Coupled Model (All units shown in mm)

A rectangular fluid domain of 600 mm length, 400 mm width, and 400 mm thick was designed surrounding the main model as shown in Figure 3.2. The model was placed 150 mm from the inlet and was placed in the center equally spaced between top, bottom and side wall from the domain illustrated in Figure 3.3. The fluid domain had a 1.4 % blockage ratio which was lower than a standard maximum of 3 % when structural model was placed inside the fluid domain.

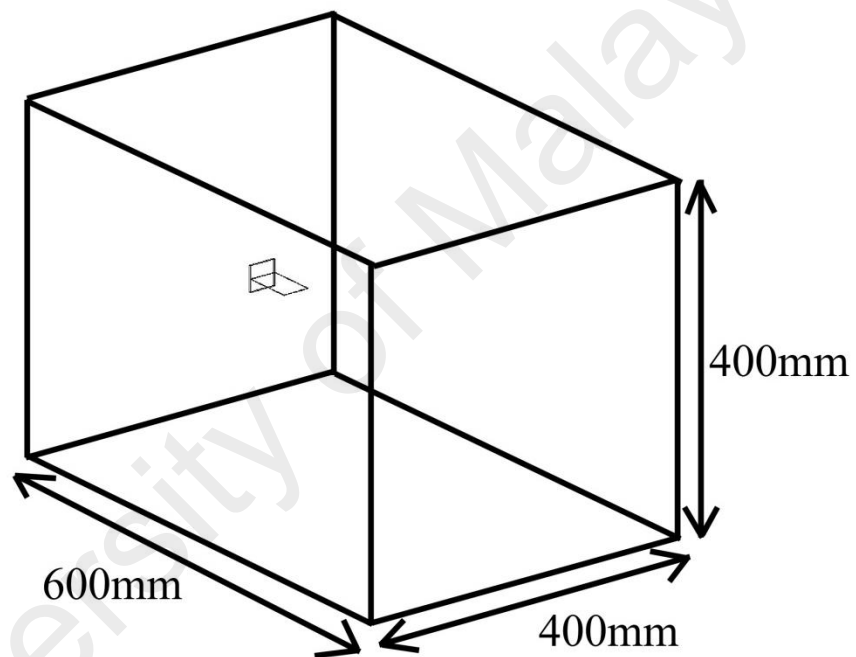


Figure 3.2: Computational Domain Size (PVEH Model Coupled with Bluff Splitter Body)

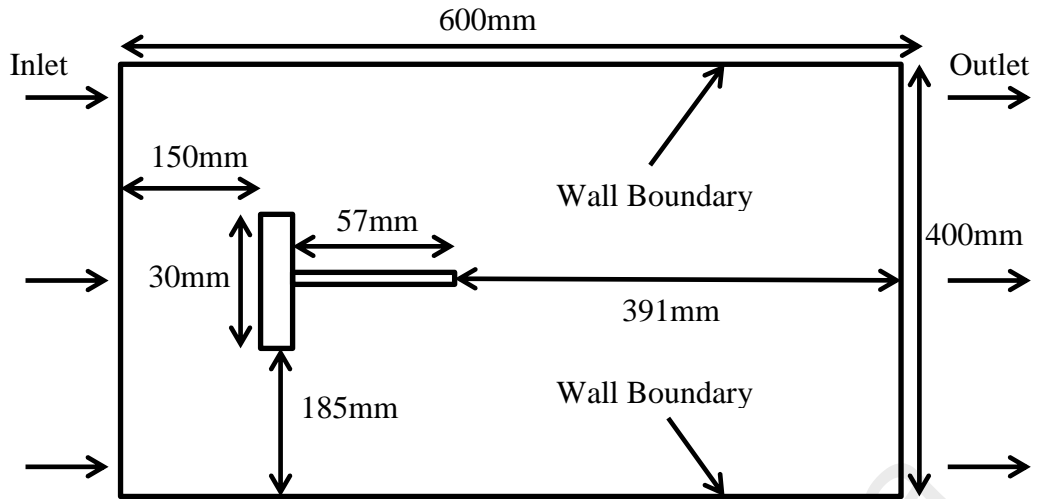


Figure 3.3: Side View Illustration of Fluid Domain Dimensions and Model Placement

Table 3.1: Material Properties and Dimensions of PVEH Plate and Bluff Splitter Body Model

Material	Piezoelectric plate (Brass)	Piezoelectric plate (PZT)	Aluminum Bluff Splitter Body
Model Dimensions	31.8mm × 57mm × 0.196mm thick	31.8mm × 57mm × 0.128mm thick	31.8mm × 30mm × 2mm thick
Density	8830 kg/m ³	7800 kg/m ³	2770 kg/m ³
Young's Modulus	1.03×10 ¹¹ Pa	x-direction- 6.6×10 ¹⁰ Pa y-direction- 6.6×10 ¹⁰ Pa z-direction- 5.2×10 ¹⁰ Pa	7.1×10 ¹⁰ Pa
Poisson's Ratio	0.34	x-direction- 0.31 y-direction- 0.242 z-direction- 0.242	0.33

3.3.2 Coupled Bluff Splitter Body and Elastic Plate Model

In all of the following research sections including the studies of VIV effect on different wind speeds, different bluff splitter body widths, different elastic plate lengths and different bluff splitter body shapes, an elastic plate was used as the flexible structure. The coupled bluff splitter body and elastic plate model designed as such in Figure 3.4 was a reference to the structure applied in the research done by Dettmer and Peric (2006) with similar material properties throughout the sections as listed in

Table 3.2.

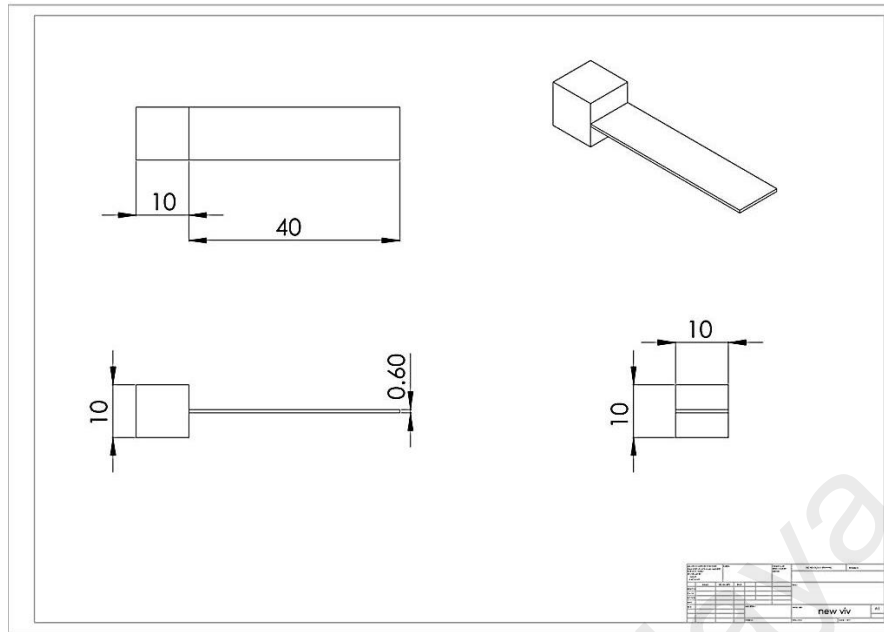


Figure 3.4: Coupled Bluff Splitter Body and Elastic Plate Model by Dettmer (All units shown in mm)

Table 3.2: Material Properties of Coupled Bluff Splitter Body and Elastic Plate Model

Material	Elastic plate	Bluff Splitter Body
Model Dimensions	0.04m × 0.0006m × 0.01m	0.01m × 0.01m × 0.01m
Density	0.001 kg/m ³	2770 kg/m ³
Young's Modulus	2.5 × 10 ⁵ Pa	7.1 × 10 ¹⁰ Pa
Poisson Ratio	0.35	0.33

Different modifications were done to the structural model in order to study VIV performance enhancement. In the first objective second section, the structural model remained the same as the original design. But modifications were done on either the bluff splitter body or elastic plate under the studies of aspect ratio and shape effects in VIV.

3.3.2.1 Coupled Bluff Splitter Body and Elastic Plate Aspect Ratio Modifications

This objective is to achieve VIV performance enhancement through structural model aspect ratio modifications. This section is divided into two parts which is bluff splitter body width variance and elastic plate length variance.

(a) Bluff Splitter Body Width Modifications

For this section of bluff splitter body width modification, the length and thickness of the bluff splitter body remained the same at 0.01 m while changing the width value between 0.005 m, 0.01 m, 0.02 m, 0.03 m, 0.04 m, 0.06 m and 0.08 m as shown in Figure 3.5(a) to (f). The dimensions of the elastic plate remained the same as shown in Table 3.2

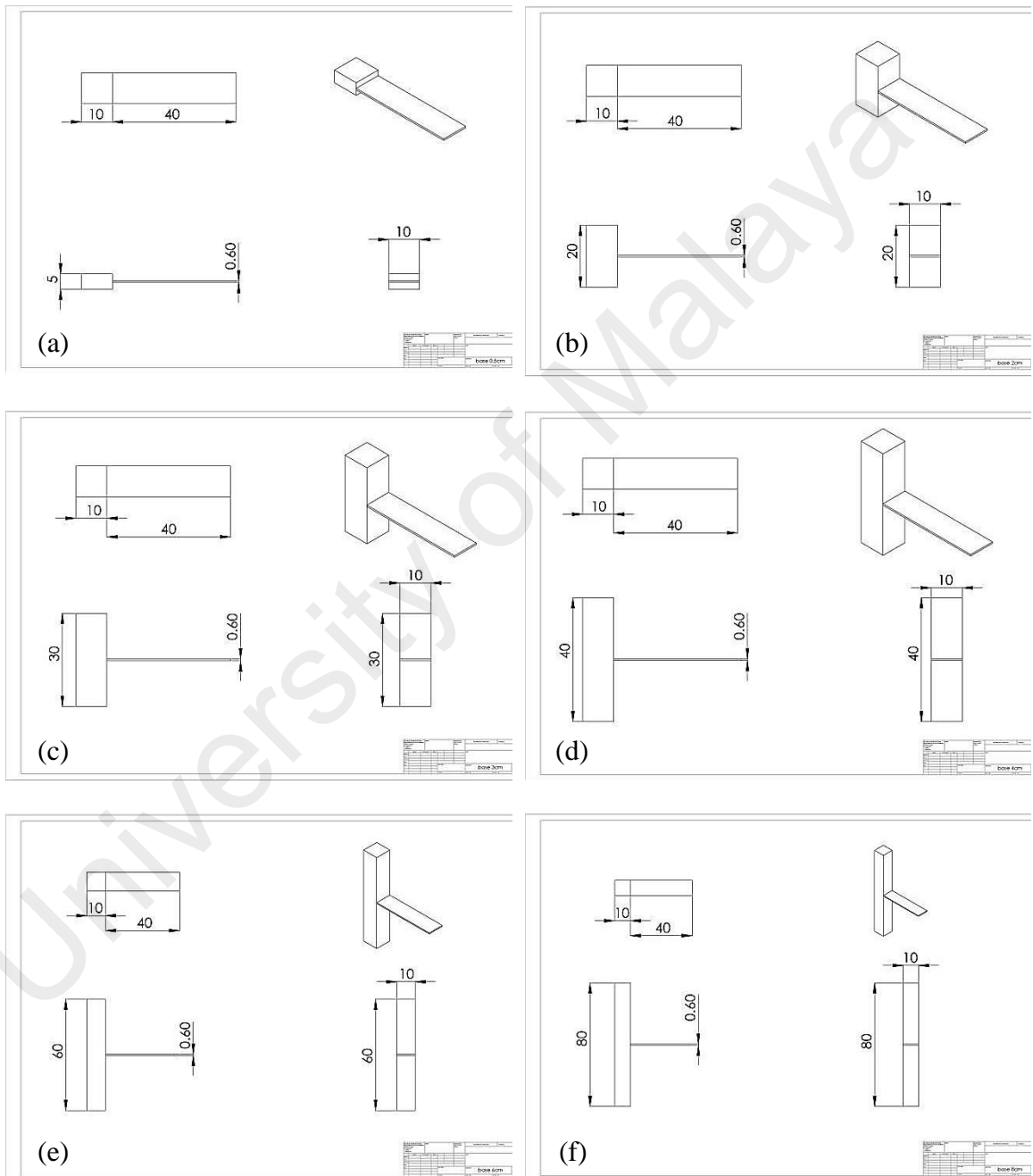


Figure 3.5: Coupled Bluff Splitter Body and Elastic Plate Model with Different Bluff Splitter Body Width (a) 0.005m (b) 0.02m (c) 0.03m (d) 0.04m (e) 0.06m (f) 0.08m (All units shown in mm)

(b) Elastic Plate Length Modifications

After the results of bluff splitter body width modifications were obtained in Section 4.2.1, it was discovered that 0.03 m wide bluff splitter body had a much better VIV performance compared to 0.01 m as proposed in Dettmer et al.'s research. The second part of the objective involved the coupling of bluff splitter body with different lengths of elastic plate. The elastic plate length tested were 0.02 m, 0.03 m, 0.04 m, 0.05 m and 0.06 m respectively while the width and thickness maintained at 0.0006 m and 0.01 m as shown in Figure 3.6(a) to (d).

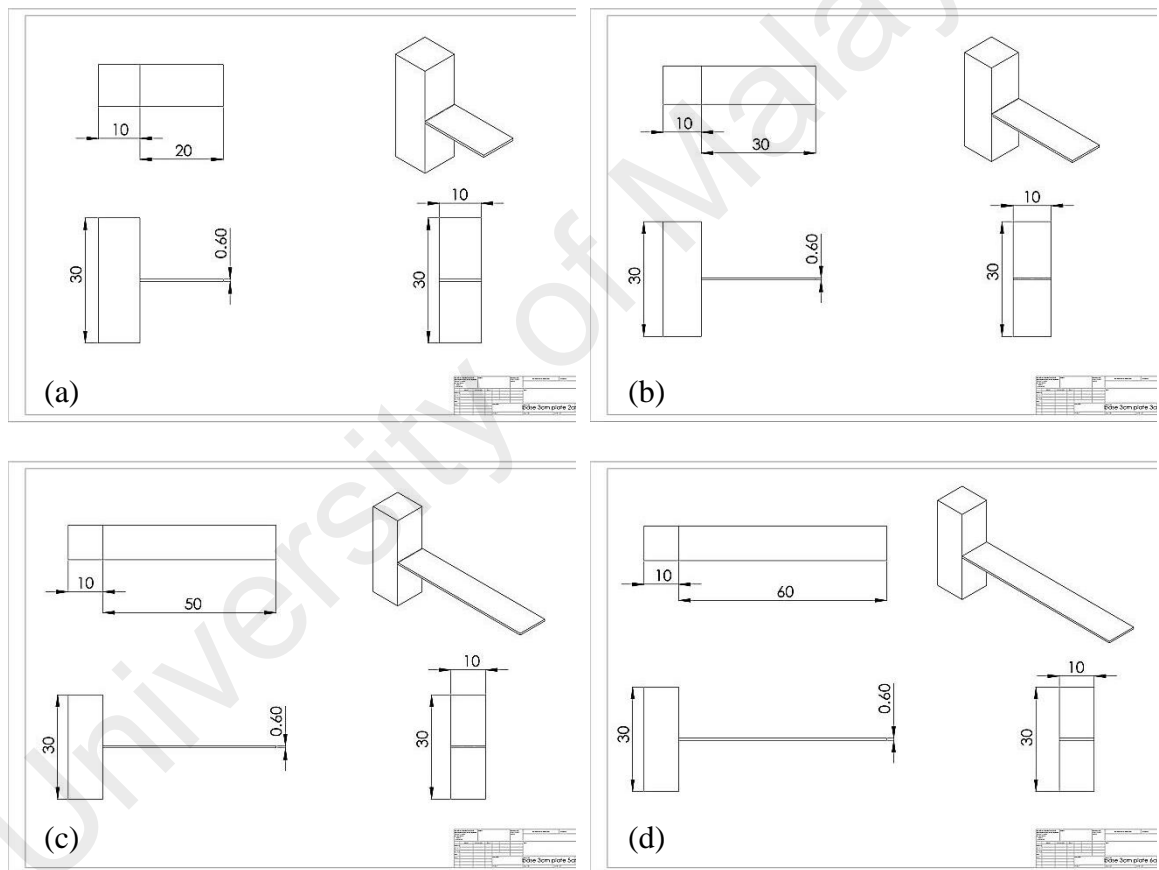


Figure 3.6: Coupled Bluff Splitter Body and Elastic Plate Model with Different Elastic Plate Length (a) 0.02m (b) 0.03m (c) 0.05m (d) 0.06m (All units shown in mm)

3.3.2.2 Bluff Splitter Body Design Modifications

The final objective is to investigate VIV performance enhancement with different bluff splitter body shape. All the bluff splitter body designs were set with the same dimension

of 0.01 m length x 0.03 m width x 0.01 m thickness but the principal shape of the bluff splitter body was varied.

(a) Bluff Splitter Body Cross-Sectional Shape Modifications

In the first section of the final objective, different bluff splitter body shapes were investigated, i.e. Curve I, Curve II, Diffuser I, Diffuser II, Semicircle I, Semicircle II, Trapezoidal I, Trapezoidal II, Triangle I, Triangle II Rectangular and Circular. Concave shape bluff splitter bodies include Curve I, Diffuser I, Semicircle I, Triangle I and Trapezoidal I had a diverging leading edge and straight trailing edge. Leading edge and trailing edge can be explained through Figure 3.7, whereby leading edge is the edge placed upstream while trailing edge is the edge downstream of the bluff splitter body. Convex shape bluff splitter bodies include Curve II, Diffuser II, Semicircle II, Trapezoidal II and Triangle II had a straight leading edge and converging trailing edge. Symmetrical shape designs include Circular and Rectangular shape bluff splitter body. Circular shape had a diameter of 0.03m was the only shape that did not follow the 0.01 m thickness criteria. For Curve and Diffuser shape, the overall shape followed the maximum width of 0.03 m and length of 0.01 m but the thickness of the plate was only 0.0025 m. All the structural models CAD drawings were displayed in Figure 3.8(a) to (k).

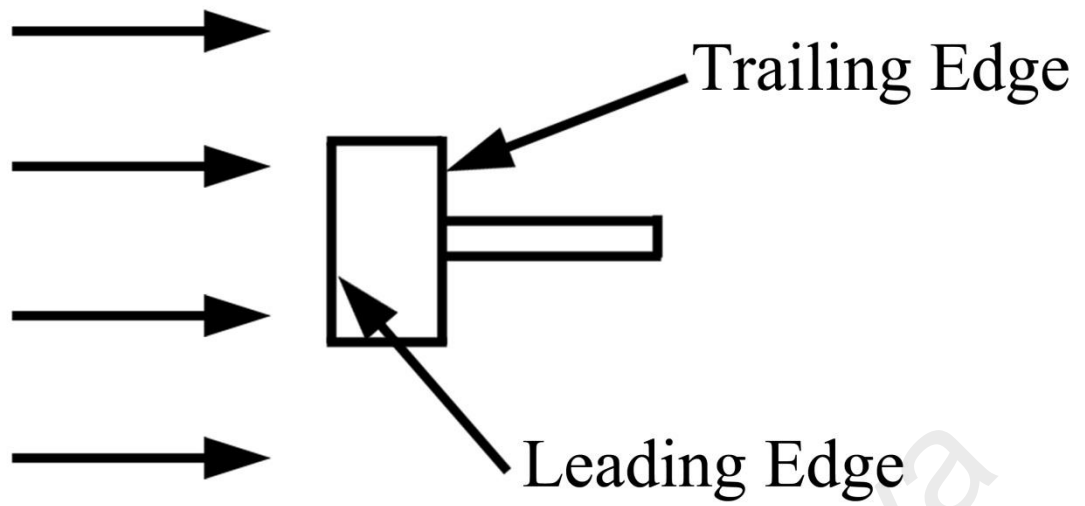
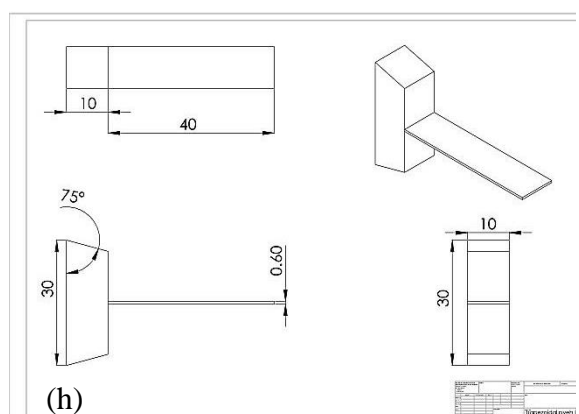
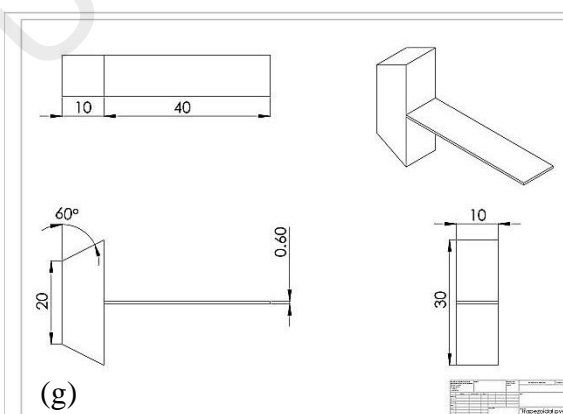
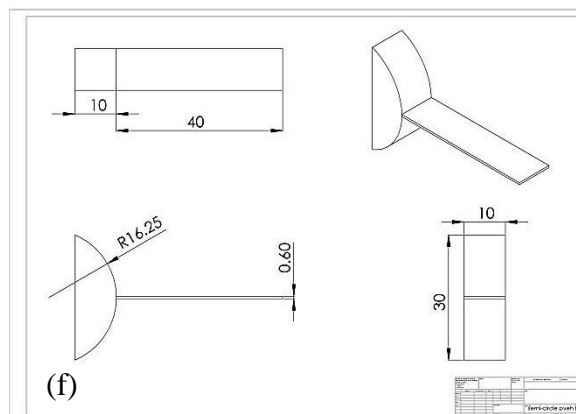
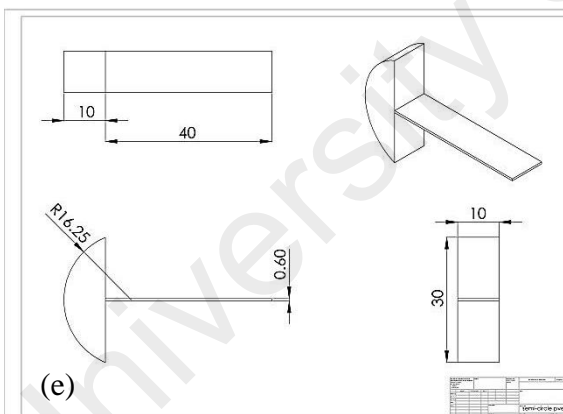
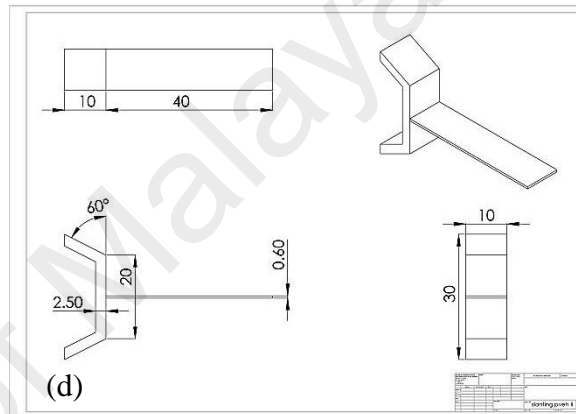
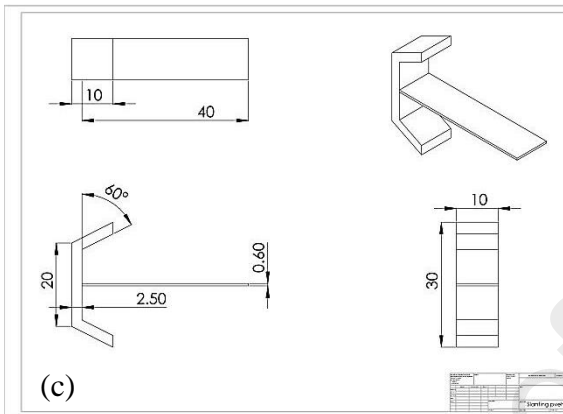
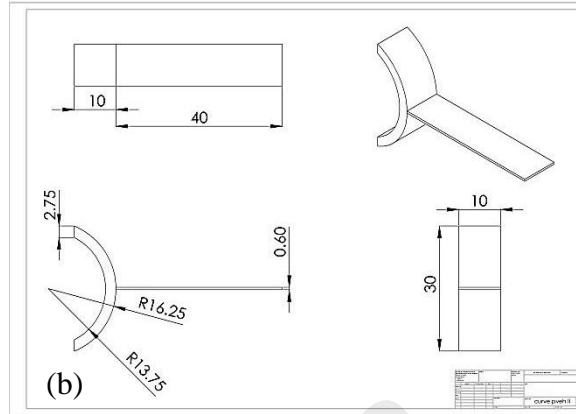
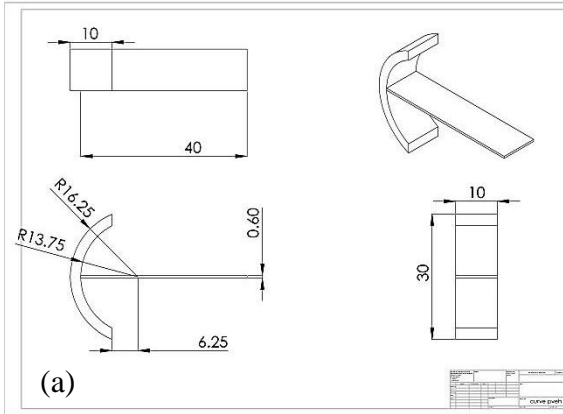


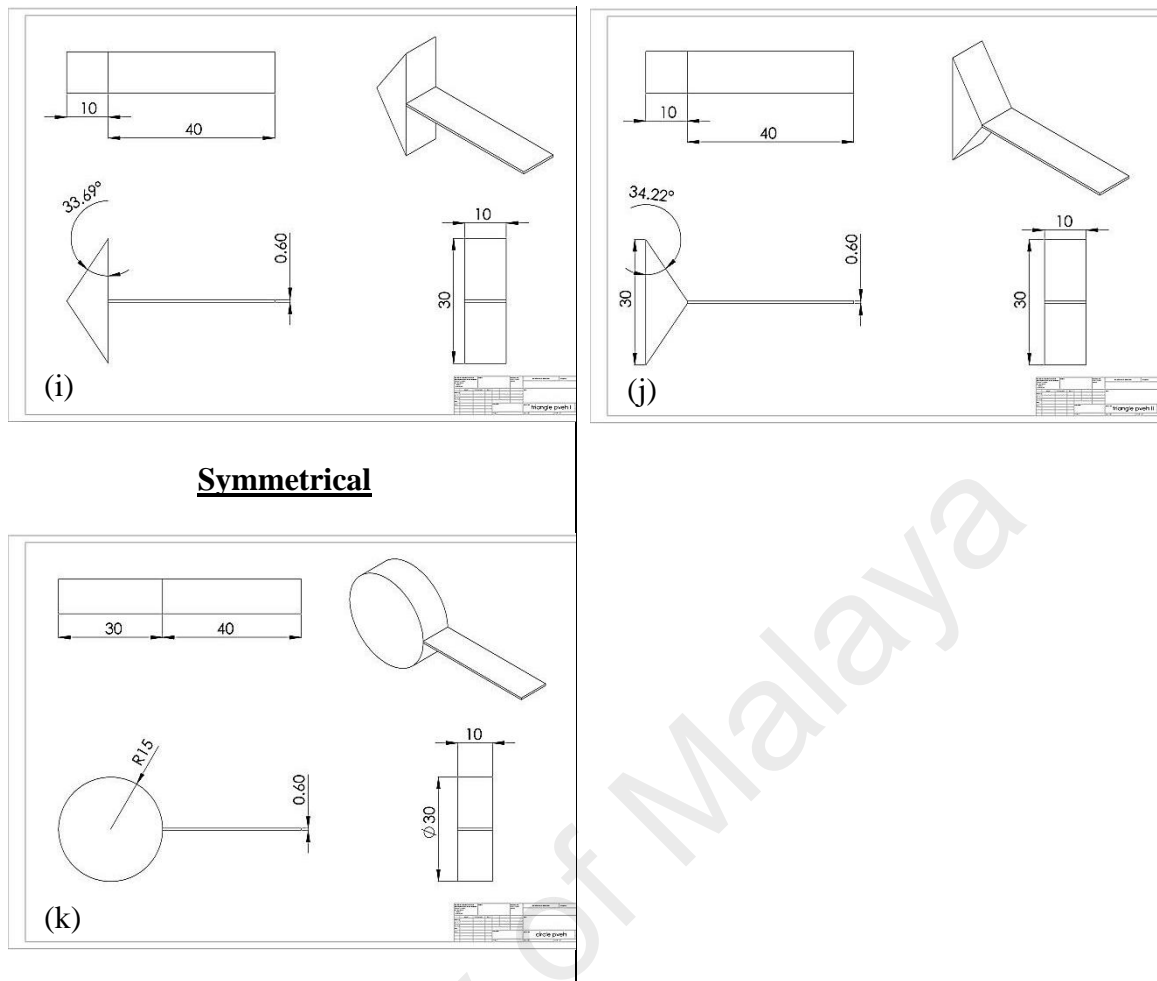
Figure 3.7: Bluff Splitter Body's Trailing Edge and Leading Edge

University of Malaya

Concave

Convex





Symmetrical

Figure 3.8: Coupled Bluff Splitter Body and Elastic Plate Model with Different Bluff Splitter Body Shape (a) Curve I (b) Curve II (c) Diffuser I (d) Diffuser II (e) Semicircle I (f) Semicircle II (g) Trapezoidal I (h) Trapezoidal II (i) Triangle I (j) Triangle II (k) Circular (All units shown in mm)

(b) Bluff Splitter Body Edge Angle Modifications

The second part of this section involved the investigation of different bluff splitter body edge angles to the VIV performance. From the first part of the objective, Triangle II, Trapezoidal II, Trapezoidal I and Triangle I had each represented four different bluff splitter body side edge angles of 34.22° , 75° , 120° and 146.31° displayed in Figure 3.8(j), (h), (g) and (i). Another two edge angles of 45° and 60° bluff splitter body shape was designed for this investigation as displayed in Figure 3.9 (a) and (b).

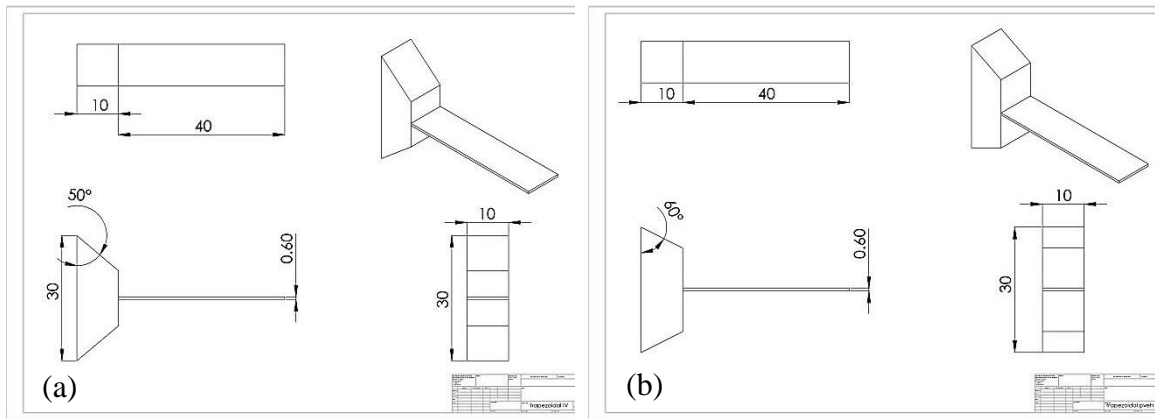


Figure 3.9: Coupled Bluff Splitter Body and Elastic Plate Model with Different Side Edge Angle of (a) 45° and (b) 60° (All units shown in mm)

3.3.2.3 Fluid Domain Design

The fluid domain applied in this coupled bluff splitter body and elastic plate model mentioned is designed differently with the one mentioned in the Section 3.3.1. A symmetrical 3D fluid domain with the same thickness as the structural model, applying symmetrical boundary condition on each side wall of the domain is designed. The dimension of the domain is 1.2 m length x 0.8 m width x 0.01 m thickness as illustrated in Figure 3.10. The model is being placed 0.3 m away from the inlet and centered between top and bottom walls illustrated in Figure 3.11. The same fluid domain dimension is applied in every section listed above that involves the application of coupled bluff splitter body and elastic plate model.

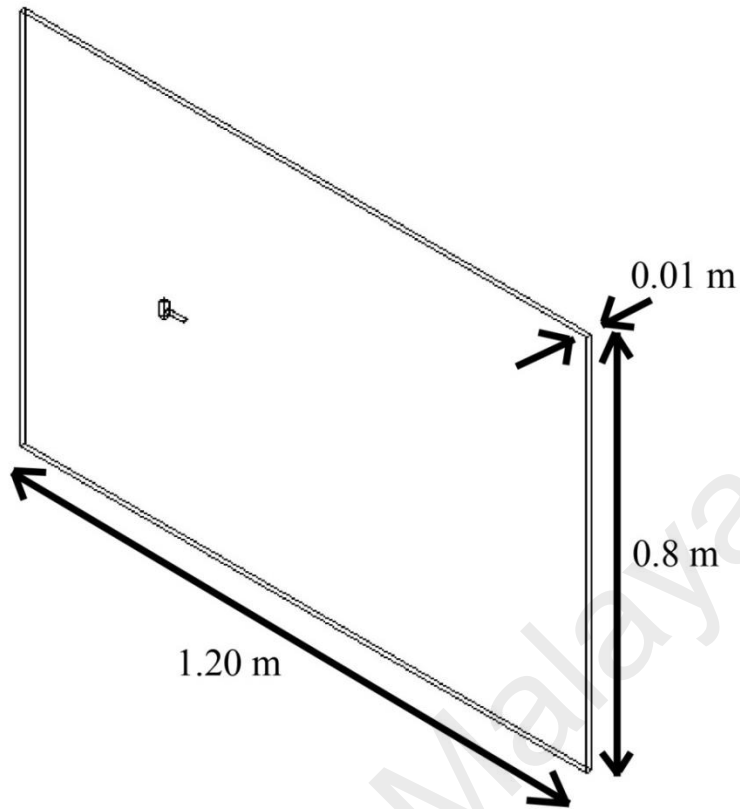


Figure 3.10: CFD Fluid Domain for all Coupled Bluff Splitter Body and Elastic Plate Model

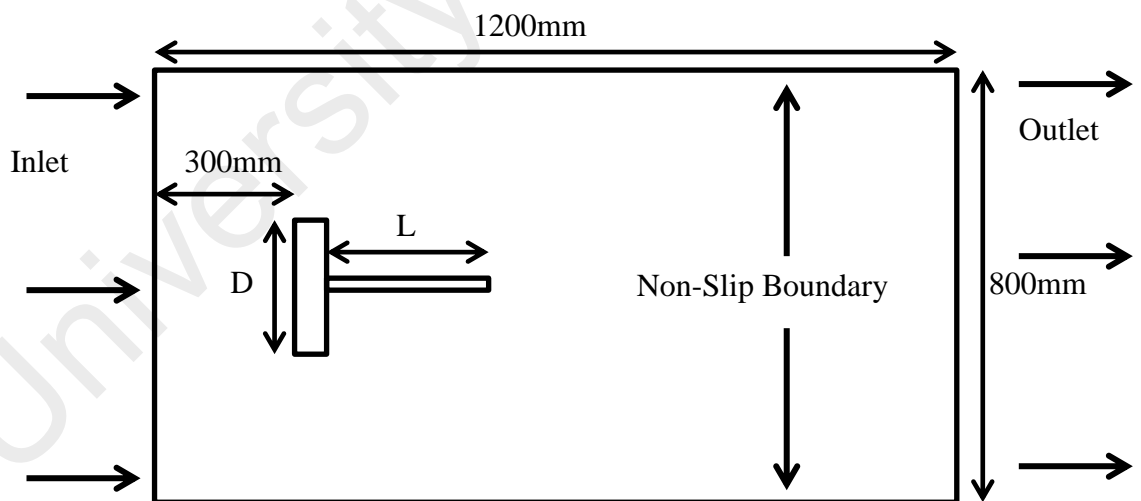


Figure 3.11: Fluid Domain Dimension Illustration (D = Bluff Body Width & L = Elastic Plate Length)

3.4 Meshing Parameters

This section will mention different mesh parameters applied onto different simulation conducted. The meshing was done using ICEM meshing module integrated in ANSYS software.

3.4.1 Coupled Bluff Splitter Body and PVEH Plate

Meshing done onto both the structural model and fluid domain will be explained. The fluid domain used was a full 3-dimensional domain, hence extra effort had to be done to refine the mesh to better accommodate the resolution needed.

3.4.1.1 Structural Model Mesh

For Coupled Bluff Splitter Body and PVEH Plate model, the structural model mesh was done uniformly with 0.001 m x 0.001 m structured quadrilateral prism mesh. The mesh generated on the structural part shown in Figure 3.12 owned a total of 50,709 nodes and 7,392 elements with mesh skewness near zero.

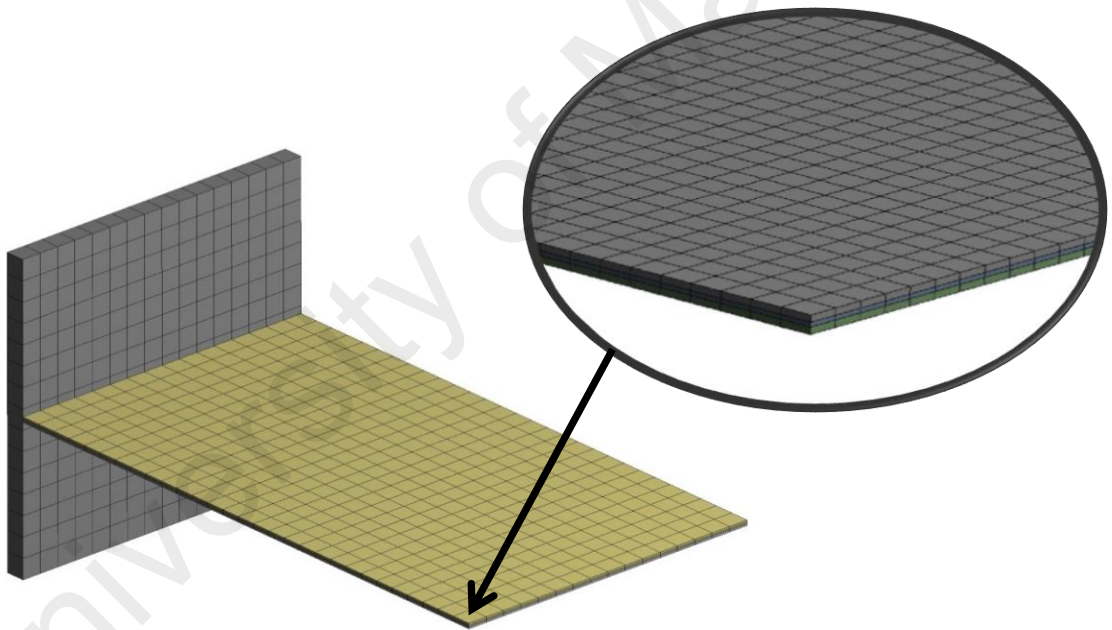


Figure 3.12: 0.001m Coupled Bluff Splitter Body and PVEH Plate Model Structured Prism Mesh

3.4.1.2 Computational Fluid Domain Mesh

0.001 m to 0.2 m of unstructured tetrahedral mesh was assigned onto the CFD domain depending on the closeness to the structural model's FSI interface shown in Figure 3.13. FSI interface wall boundary surrounding the structural model in CFD domain was meshed with element face size of 0.001 m integrated with 10 layers of inflation layer

grid as displayed in Figure 3.14. A total of 98,148 nodes and 325,010 elements were generated with maximum skewness reaching value of 0.78.

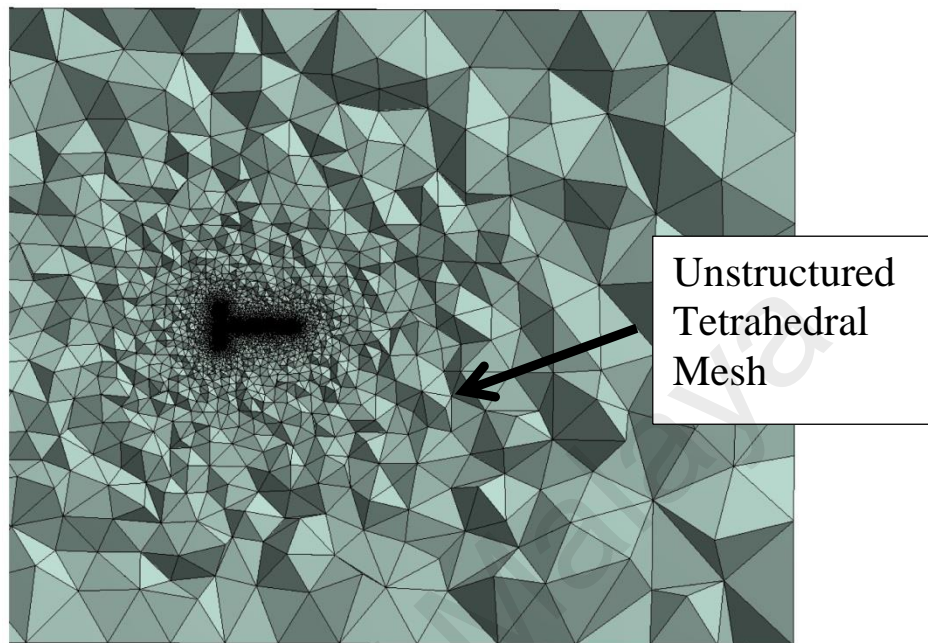


Figure 3.13: 0.001m to 0.2m size CFD Domain Mesh of Coupled Bluff Splitter Body and PVEH Plate Model

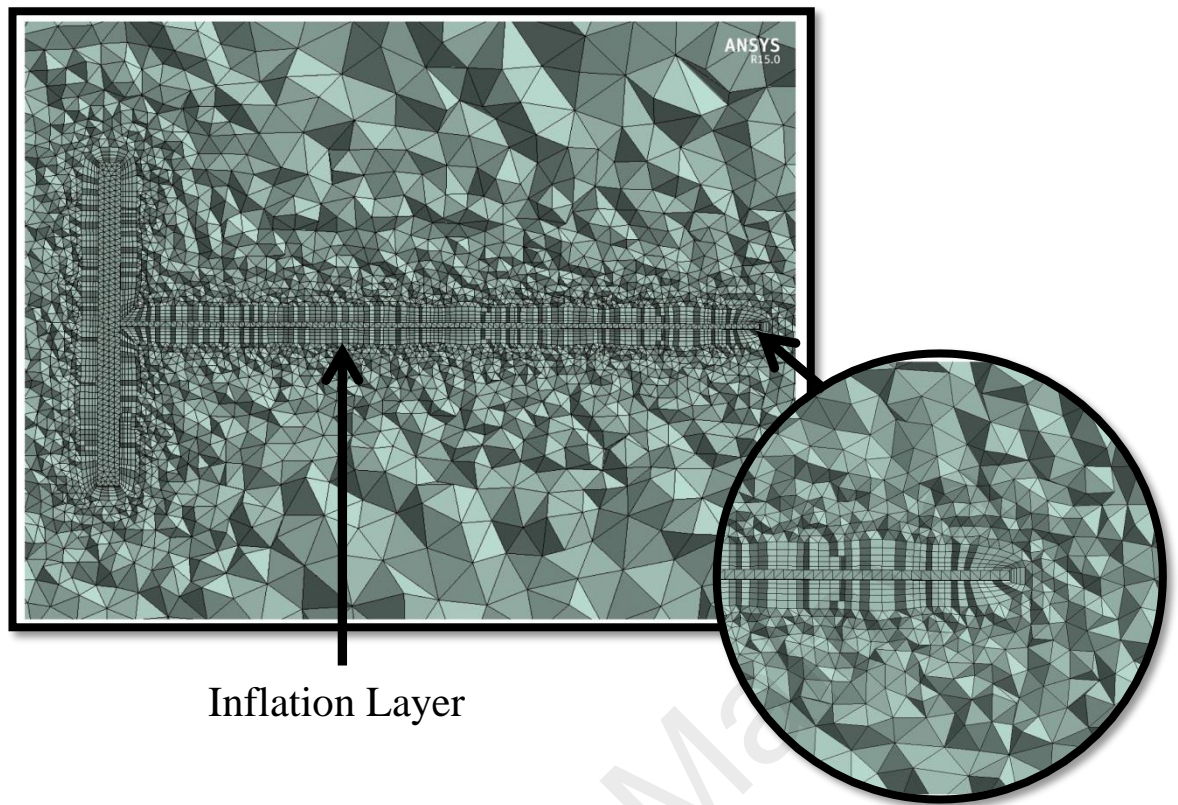


Figure 3.14: Magnified CFD Domain Mesh of Coupled Bluff Splitter Body and PVEH Plate Model with Display of 10 Layer Inflation Layer

3.4.2 Coupled Bluff Splitter Body and Elastic Plate Model

Although the coupled bluff splitter body and elastic plate model designed in Section 3.3.2 included different variations of bluff splitter body width, elastic plate length, shapes and edge angle of bluff splitter body, the meshing parameters remained the same throughout all three different objectives.

3.4.2.1 Structural Model mesh

The entire model was set with a prism mesh of dimension 0.001 m x 0.001 m. Figure 3.15 showed an example of structural model mesh using coupled bluff splitter body and elastic plate model. Table 3.3 showed the number of nodes, number of elements and the resulting mesh skewness for each individual structural model designed for simulation. The resulting mesh of coupled bluff splitter body and elastic plate models had different skewness values because some of the structural model contained curvature, thus the mesh was unable to be created with structured square prism shapes similar to Section

3.4.1.1. As for structural model with different elastic plate lengths and bluff splitter body widths, structural prism mesh was able to be generated, thus mesh skewness is 0.

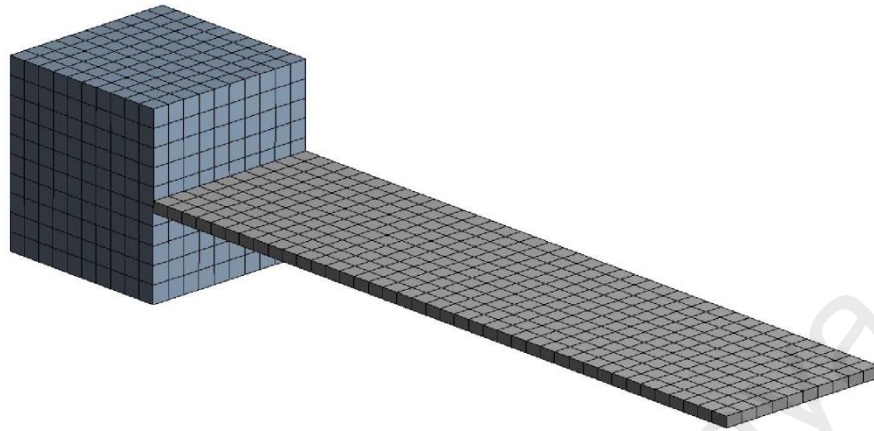


Figure 3.15: 0.001m Coupled Bluff Splitter Body and Elastic Plate Model Structural Mesh

Table 3.3: Structural Model Mesh of No. of Nodes, No. of Elements and Mesh Skewness of Different Coupled Bluff Splitter Body and Elastic Plate Model

Structural Model	Nodes	Elements	Skewness
Bluff Splitter Body Width = 0.005 m Elastic Plate Length = 0.04 m	5,704	900	0
Bluff Splitter Body Width = 0.01 m Elastic Plate Length = 0.04 m	8,014	1,400	0
Bluff Splitter Body Width = 0.02 m Elastic Plate Length = 0.04 m	12,634	2,400	0
Bluff Splitter Body Width = 0.03 m Elastic Plate Length = 0.04 m	17,254	3,400	0
Bluff Splitter Body Width = 0.04 m Elastic Plate Length = 0.04 m	21,874	4,400	0
Bluff Splitter Body Width = 0.06 m Elastic Plate Length = 0.04 m	31,114	6,400	0
Bluff Splitter Body Width = 0.08 m Elastic Plate Length = 0.04 m	40,354	8,400	0
Bluff Splitter Body Width = 0.03 m Elastic Plate Length = 0.02 m	15,754	3,200	0
Bluff Splitter Body Width = 0.03 m Elastic Plate Length = 0.03 m	16,504	3,300	0
Bluff Splitter Body Width = 0.03 m Elastic Plate Length = 0.05 m	18,004	3,500	0
Bluff Splitter Body Width = 0.03 m Elastic Plate Length = 0.06 m	18,754	3,600	0
Bluff Splitter Body Shape: Curve I	8,805	1,450	0.305
Bluff Splitter Body Shape: Curve II	8,805	1,450	0.304
Bluff Splitter Body Shape: Diffuser I	9,610	1,600	0.280
Bluff Splitter Body Shape: Diffuser II	9,610	1,600	0.280
Bluff Splitter Body Shape: Semicircle I	14,858	2,880	0.440
Bluff Splitter Body Shape: Semicircle II	29,152	6,100	0.920

Bluff Splitter Body Shape: Trapezoidal I	17,158	3,400	0.280
Bluff Splitter Body Shape: Trapezoidal II	17,566	3,480	0.158
Bluff Splitter Body Shape: Triangle I	11,881	2,210	0.578
Bluff Splitter Body Shape: Triangle II	27,830	5,800	0.589
Bluff Splitter Body Shape: Circular	61,307	13,630	0.792
Bluff Splitter Body Angle: 60°	17,158	3,400	0.280
Bluff Splitter Body Angle: 45°	16,202	3,200	0.422

3.4.2.2 Computational Fluid Domain Mesh

On the other hand, Figure 3.16 showed the overall fluid domain for CFD analysis was mesh with grid size 0.00025 m to 0.005 m depending on the closeness of the mesh to the structural interface. The closer the distance to the structural interface, the smaller was the mesh size. The fluid domain designed for all coupled bluff splitter body and elastic plate structural models were symmetrical, in which every cross-section along the thickness of the domain was similar. Hence, in this section, the domain was able to effectively mesh with an unstructured quadrilateral mesh instead of tetrahedrons slightly reducing number of nodes and elements furthermore lowered the computational cost. The fluid and structure interface wall were assigned with a constant face mesh size of 0.00025 m structured quadrilateral mesh illustrated in Figure 3.17. A 10 layer inflation layer shown in Figure 3.18 was added to the edges surrounding the structural model to ensure fine mesh surrounding the fluid and structure interface and thus able to generate higher resolution vortex formation result. A Sweep Method was applied onto the fluid domain replicating mesh from the frontal cross-section area to 5 subsequent cross-sectional layers shown in Figure 3.19. The total number of nodes and elements of the fluid domain mesh is shown in Table 3.4.

Table 3.4: Fluid Domain Mesh of No. of Nodes, No. of Elements and Mesh Skewness of Different Coupled Bluff Splitter Body and Elastic Plate Model

Computational Fluid Domain	Nodes	Elements	Skewness
Bluff Splitter Body Width = 0.005 m Elastic Plate Length = 0.04 m	338,910	279,520	0.682
Bluff Splitter Body Width = 0.01 m Elastic Plate Length = 0.04 m	355,026	292,705	0.659
Bluff Splitter Body Width = 0.02 m Elastic Plate Length = 0.04 m	351,360	289,535	0.705

Bluff Splitter Body Width = 0.03 m Elastic Plate Length = 0.04 m	367,068	302,465	0.729
Bluff Splitter Body Width = 0.04 m Elastic Plate Length = 0.04 m	381,090	313,975	0.736
Bluff Splitter Body Width = 0.06 m Elastic Plate Length = 0.04 m	401,688	330,715	0.718
Bluff Splitter Body Width = 0.08 m Elastic Plate Length = 0.04 m	428,394	352,620	0.700
Bluff Splitter Body Width = 0.03 m Elastic Plate Length = 0.02 m	344,382	283,945	0.618
Bluff Splitter Body Width = 0.03 m Elastic Plate Length = 0.03 m	353,670	291,500	0.734
Bluff Splitter Body Width = 0.03 m Elastic Plate Length = 0.05 m	378,600	311,885	0.717
Bluff Splitter Body Width = 0.03 m Elastic Plate Length = 0.06 m	388,890	320,270	0.671
Bluff Splitter Body Shape: Curve I	346,770	285,635	0.694
Bluff Splitter Body Shape: Curve II	371,628	306,340	0.678
Bluff Splitter Body Shape: Diffuser I	359,412	269,045	0.675
Bluff Splitter Body Shape: Diffuser II	348,576	287,040	0.809
Bluff Splitter Body Shape: Semicircle I	347,844	286,645	0.694
Bluff Splitter Body Shape: Semicircle II	366,516	302,150	0.643
Bluff Splitter Body Shape: Trapezoidal I	348,648	287,170	0.776
Bluff Splitter Body Shape: Trapezoidal II	355,848	293,205	0.711
Bluff Splitter Body Shape: Triangle I	348,684	287,315	0.772
Bluff Splitter Body Shape: Triangle II	350,976	289,150	0.914
Bluff Splitter Body Shape: Circular	360,000	296,455	0.684
Bluff Splitter Body Angle: 75°	328,086	270,035	0.813
Bluff Splitter Body Angle: 45°	349,176	287,600	0.716

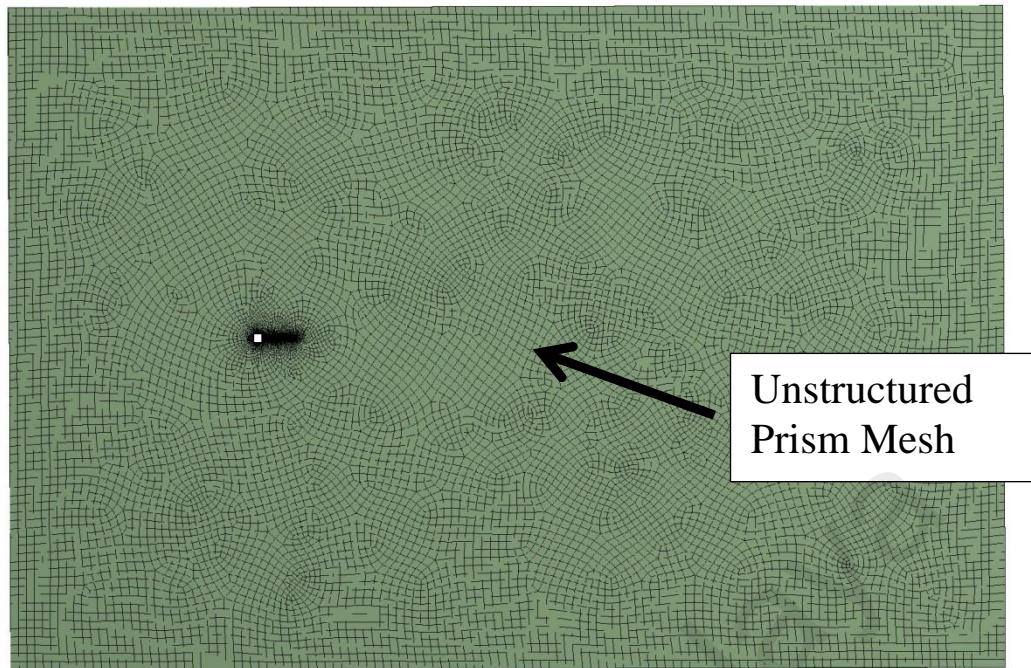


Figure 3.16: 0.00025m to 0.005m size CFD Domain Mesh of Coupled Bluff Splitter Body and PVEH Plate Model

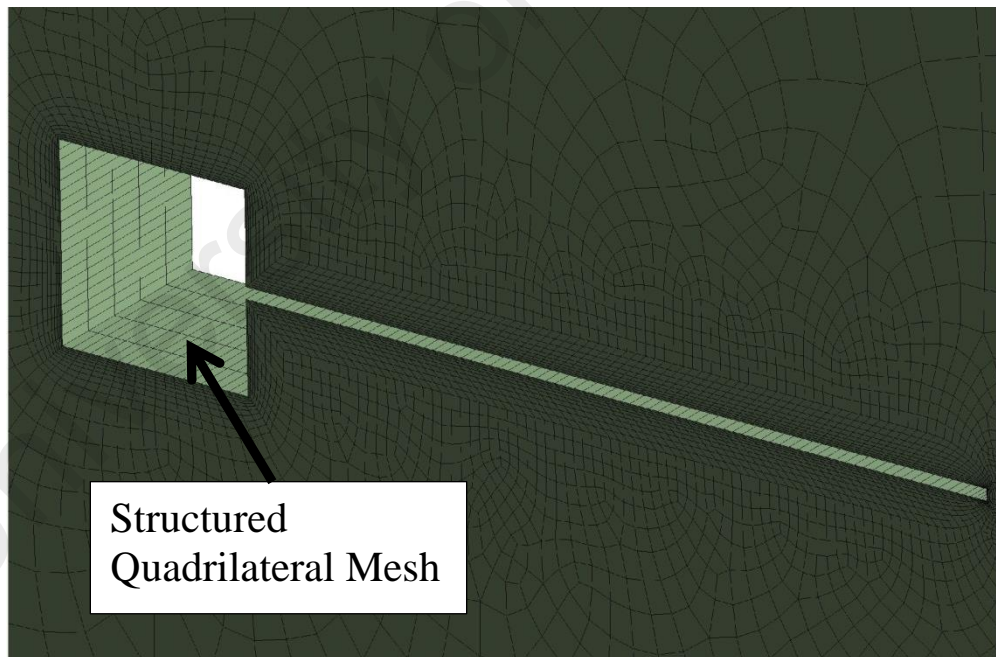


Figure 3.17: 0.00025m Mesh Size for Contact Wall Surface of Coupled Bluff Splitter Body and Elastic Plate Model in CFD Domain

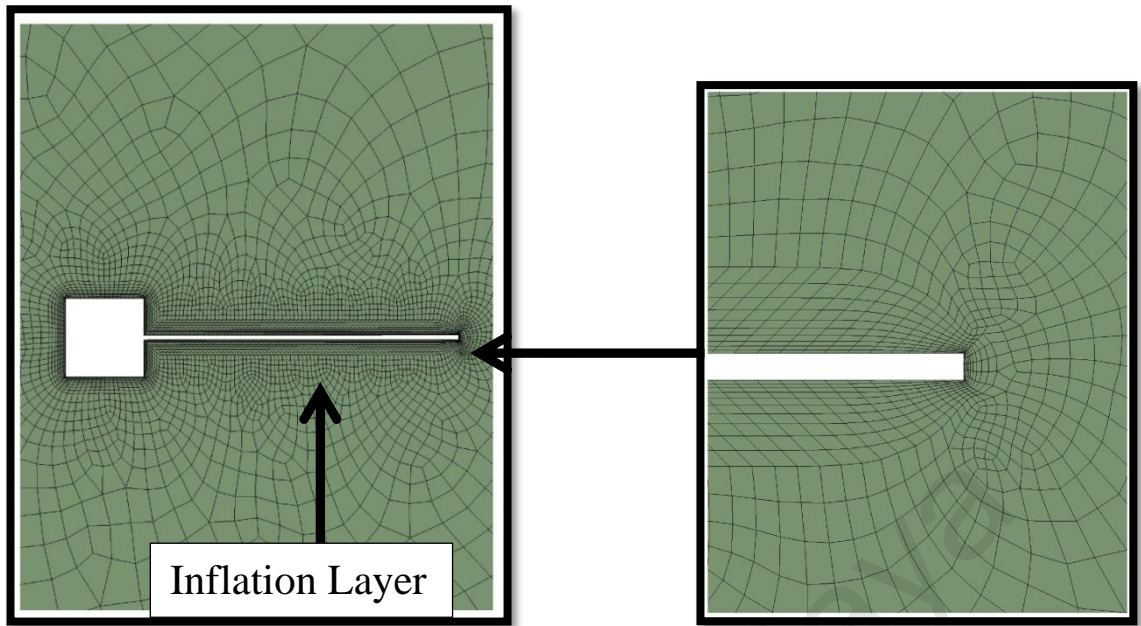


Figure 3.18: Magnified CFD Domain Mesh of Coupled Bluff Splitter Body and PVEH Plate Model with Display of 10 Layer Inflation Layer

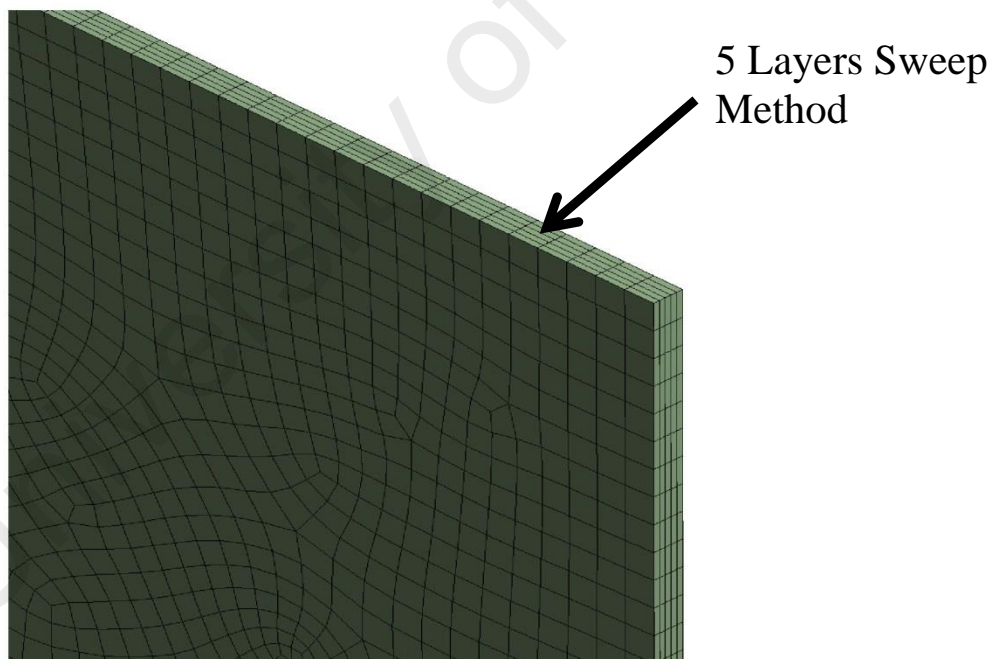


Figure 3.19: Sweep Method Layers across Thickness of Fluid Domain

3.5 Fluid-Structure Interaction Simulation Settings

Boundary conditions, simulation model and parameters, time steps and monitor points were set in order to obtain the desired results in most accurate manner.

3.5.1 Coupled Bluff Splitter Body and PVEH Plate Model

FSI simulation involved setup of both CFX module for CFD analysis and Mechanical APDL module for structural dynamics analysis. In Mechanical APDL module, the model's material properties were defined according to Table 3.1. The bluff splitter body model was set as fixed boundary relative to space. Surfaces around the PVEH plate model were set as fluid-structure interfaces where data exchange between structure and fluid model occurred shown in Figure 3.20.

The simulation setup for CFD module shown in Figure 3.20 used material properties displayed in Table 3.1. For wind speed variance simulation, different subsonic inlet velocity of 7 m/s, 10 m/s, 12 m/s, 14 m/s, 16 m/s, 18 m/s, 19 m/s, 20 m/s, 22.5 m/s and 25 m/s were set at the inlet boundary and reference pressure of 1 atm was set at the outlet boundary. Fluid medium used was air with density, $\rho_f = 1.82 \times 10^{-4} \text{ kg/m}^3$, kinematic viscosity $\mu_f = 1.18 \times 10^{-3}$ and a constant temperature of 298.15K. The wall boundary surrounding the structural model was set as fluid-structure interaction interface boundary allowing data exchange between structural and CFD solver. The surrounding walls excluding the inlet, outlet and FSI interface boundary was assigned as a non-slip wall boundary. The fluid domain was a stationary domain but the mesh within was allowed to deform with respect to time.

SST Reynolds Stress Turbulence model was applied in this study as it is better to predict unstable 3-D separation flow in smaller scale model compared to other turbulence model including $k-\varepsilon$, $k-\omega$, Shear Stress Transport (SST) and Large Eddy Simulation (LES). ANSYS MultiField option of external solver coupling was chosen to carry out FSI analysis. Transient scheme and advection scheme were both set with Second Order Backward Euler and High Resolution respectively. The FSI coupling for this simulation was a strong two way coupling approach where the exchange of data between structural and CFD module occurred in a single coupling iteration and a

converged solution was obtained before moving to the next time step. Monitor points was set to obtain PVEH tip vibrational displacement under the influence of vortex and lift force. FSI coupling applied for this simulation was a strong two way coupling approach.

The coupling time step for the run was set at 5×10^{-4} s for 0.3 s or equivalent to 600 time steps, the time step set was based on the resolution of the vortex frequency. This time step may collect results with frequency up to 1000 Hz and able to capture frequencies lower than 100 Hz with high resolution. A maximum of 5 iterations for CFD solver and 10 iterations FSI coupling solving were set for each time step. The convergence residual target for this simulation was set at 0.0001 with an under relaxation factor of 0.75.

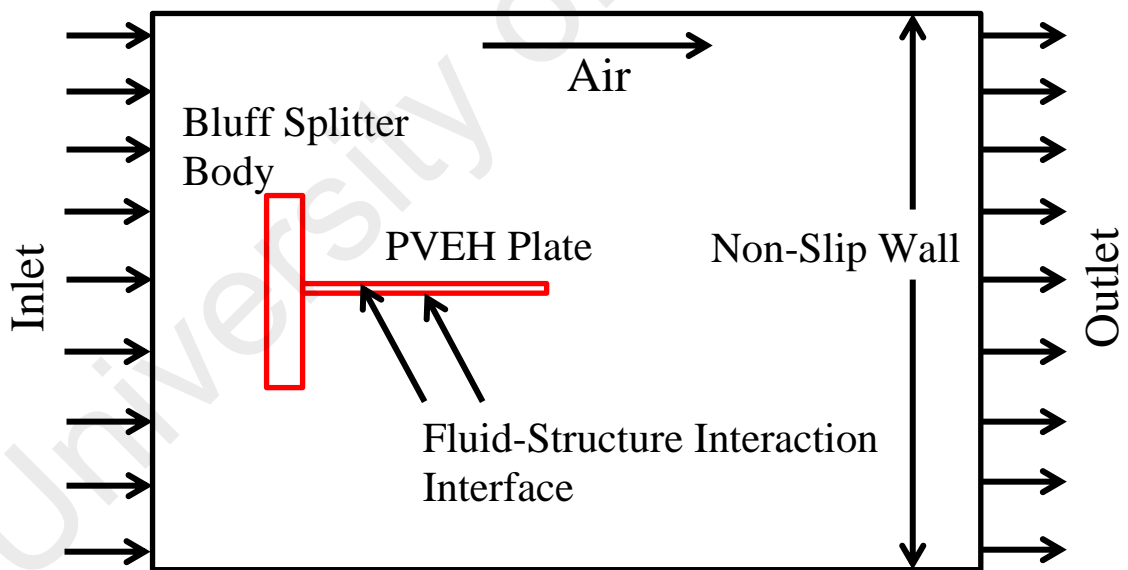


Figure 3.20: Simulation Setup of Bluff Splitter Body-PVEH Plate Coupled Model in 3D Fluid Domain with Wind Direction towards Model ($D = 30\text{mm}$)

3.5.2 Coupled Bluff Splitter Body and Elastic Plate Model

Conducting FSI simulation set up for coupled bluff splitter body and elastic plate model with symmetrical CFD domain was almost similar to the procedure done in Section

3.5.2. Mechanical APDL module was set up similarly to the PVEH plate model whereby the bluff splitter body model was applied with a fixed boundary while the elastic plate was attached onto the bluff splitter body with a cantilever boundary condition. In order to allow data transfer between modules, the surrounding side walls of the elastic plate were set as a fluid structure interaction interface.

Dettmer's original research applied a 0.513 m/s air as the main fluid medium across the domain. Using air as the fluid medium, density, $\rho_f = 1.82 \times 10^{-4} \text{ kg/m}^3$, kinematic viscosity $\mu_f = 1.18 \times 10^{-3}$ and constant temperature of 298.13 K. The outlet boundary was set at reference pressure of 1 atm. Under the section of investigating the effects of different wind speed towards VIV performance of coupled bluff splitter body and elastic plate model, wind speeds of 0.3 m/s, 0.4 m/s, 0.513 m/s, 0.6 m/s, 0.7 m/s, 1.0 m/s, and 1.5 m/s were applied onto the inlet boundary. However, in other research simulation such as bluff splitter body width variance, elastic plate length variance and different bluff splitter body design, the inlet boundary fluid velocity remained the same setting of 0.513 m/s. Likewise, the wall boundary surrounding the elastic plate was set as a fluid structure interface allowing data transfer between fluid and structural dynamics solver. As this is a symmetrical fluid domain, the side cross-sectional walls were set as a symmetrical boundary condition shown in Figure 3.21. The remaining walls which included fluid domain top and bottom walls and bluff splitter body walls were set as a non-slip wall.

The turbulence model applied in all these simulations is LES with WALE corrections. As these simulations were not conducted in a full 3-D environment and under a relatively low wind speed, complex turbulence model such as SSG Reynolds Stress Turbulence Model was not necessary. Similar to Section 3.5.1, the FSI coupling set in this section was also a strongly coupled two-way coupling approach. The residual convergence criterion was set at 0.0001 with under relaxation factor of 0.75.

Coupling time steps for all of the following fluid-structure interaction analysis was set at 0.005 s with a total of 500 steps or equivalent to a step end time of 2.5 s. The time step was not as low as the one used in Section 3.5.1 involving coupled bluff splitter body and PVEH plate model because the wind speeds involved was not too high hence the vortex frequency is lower. A maximum total of 10 iterations per coupling solving and 5 iterations for CFD solver are set for each time step.

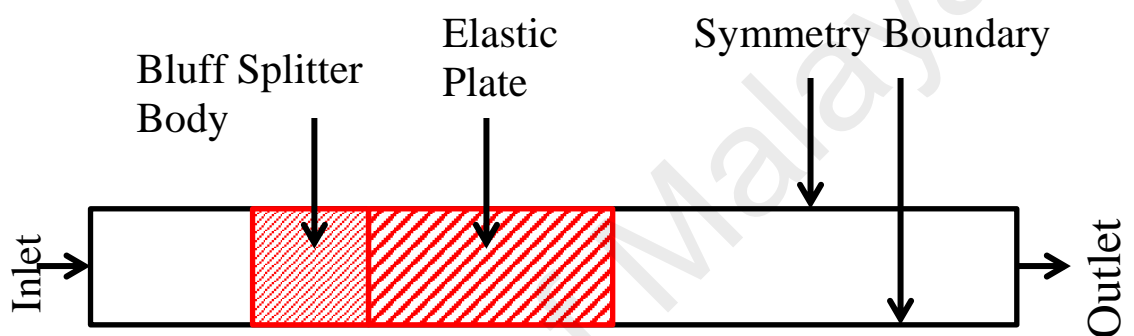


Figure 3.21: Symmetrical Boundary for Coupled Bluff Splitter Body and Elastic Plate CFD Domain (Top View)

3.6 Modal Analysis and Structural Validation

In order to identify the natural frequencies and mode shape of the models tested out in each section, modal analysis simulation had been done using the structural model meshed in Section 3.4 with the help of ANSYS Mechanical v15. This gives the vibrational mode of all natural frequencies involve. A total of 6 to 10 mode shapes and natural frequencies are being obtained through the analysis.

An experiment was set up as in Figure 3.22 to obtain the harmonic response of the PVEH plate under certain vibrational frequency; Function generator (Figure 3.22(a)) was used together with a Laser Doppler Vibrometer (LDV) (Figure 3.22(b)) to measure the vibrational displacement. The LDV model used is PDV-100 by the manufacturer on

Polytec GmbH Waldbronn. In addition, Electronic Speckle Pattern Interferometry (ESPI) technique was used to measure the transverse and planar vibrations and observe the mode shape of corresponding frequency (Figure 3.23). ESPI measurement techniques provide a real-time, non-contact and high precision measurement. The detailed ESPI technique experimental setup and performance comparison over other measurement techniques including Laser Doppler Vibrometer (LDV) and Impedance Analyzer are mentioned Ma and Huang et al. (Huang & Ma, 2009; Huang, Ma, & Li, 2014). The natural frequency and mode shape results obtained from this experiment is used further to validate the modal analysis simulation result done through ANSYS.

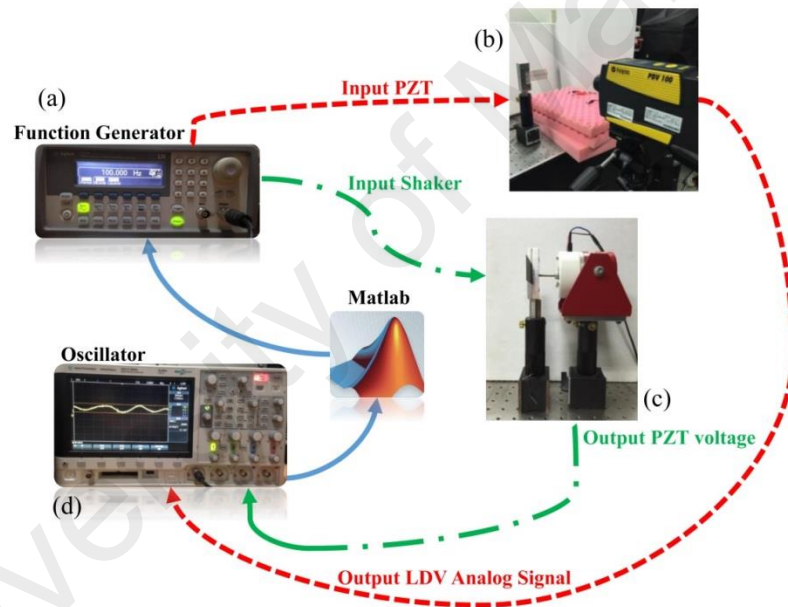


Figure 3.22: Schematic Setup of Output Voltage under Different Vibrating Frequency

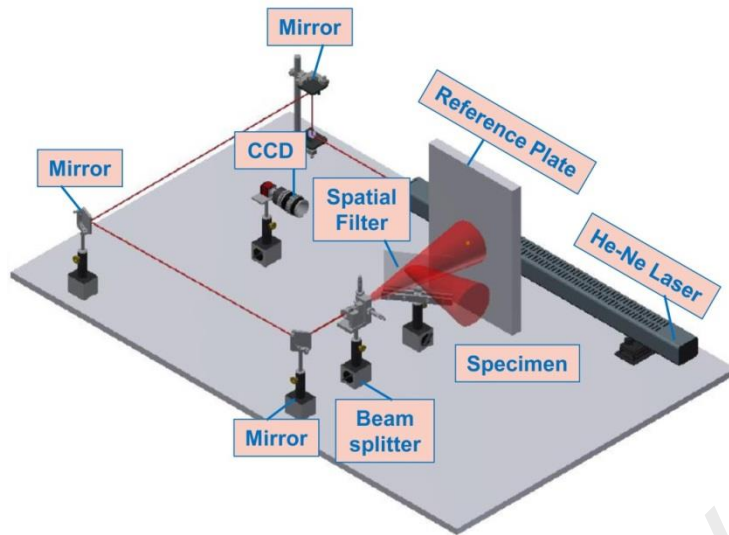


Figure 3.23: Schematic Diagram of ESPI

University of Malaya

CHAPTER 4: RESULTS AND DISCUSSION

4.1 Effect of Flow Speed on Vortex Induced Vibration Enhancement

In this objective, different wind speed are tested onto coupled bluff splitter body and PVEH plate model and also coupled bluff splitter body and elastic plate model.

4.1.1 Coupled PVEH Plate and Thin Bluff Splitter Body Model

Higher wind speeds of 7 m/s, 10 m/s, 12 m/s, 14 m/s, 16 m/s, 18 m/s, 19 m/s, 20 m/s, 22.5 m/s and 25 m/s are simulated using the same coupled bluff splitter body and PVEH plate model.

4.1.1.1 Grid Independence Study

Grid independence study is carried out in order to verify the outcome obtained is not being affected by the grid size applied. In this research, grid independence study is conducted in 4 different minimum grid sizes surrounding the model ranging from 0.006 m (20,990 elements), 0.004 m (39,168 elements), 0.002 m (104,721 elements), 0.001 m (325,010 elements) and 0.0005 m (375,598 elements). Grid independence study in this research is conducted using a transient computational fluid dynamics (CFD) method with 7 m/s inlet flow velocity while domain and turbulence model settings remain the same. By comparing the root mean square value (RMS) of fluctuating lift force acting on the PVEH plate under the effect of vortex, the simulated results in Figure 4.1 shows an increase in value from 0.000176 N by 0.006 m until it reaches 0.0016 N by 0.002 m of mesh size. The results obtained onwards have constant value around 0.0016 N and 0.0017 N which is in an acceptable range of 6.25 %. From this, the mesh size of 0.001 m, i.e. between 0.0005 m and 0.002 m is chosen for the reason of higher computational accuracy with relatively less computational cost induced when conducting simulation.

Mesh Independence Test

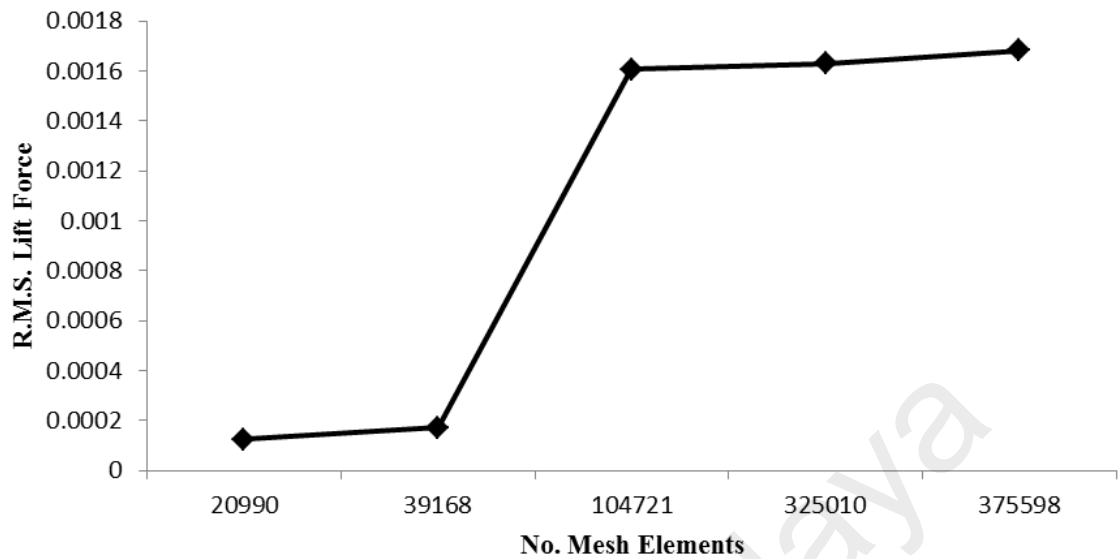


Figure 4.1: Graph of Mesh Independence Study

4.1.1.2 Structural Model Validation

Before the research is conducted, modal analysis simulation is performed onto the coupled bluff splitter body and PVEH plate to correlate with the displacement spectrum obtained from experiments ranging from 0-4000 Hz using Electronic Speckle Pattern Interferometry (ESPI). The simulated modal analysis result from Finite Element Method (FEM) (Figure 4.2) agrees well with the experimental results obtained as shown in Figure 4.3. The percentage difference is small between both simulated and experimental modal analysis with results ranging from 0.042 % to 4.614 %. Therefore, the structural model reproduced from computer aided modelling (CAM) is comparable to the real structure. As the desired frequency range in this research study is low (<100 Hz), only the first two modes are considered for comparisons especially the first mode. This model hence is experimental validated in terms of the structural aspect.

Modal Analysis simulation results shown in Figure 4.2 determined that the fundamental frequency for coupled bluff splitter body and PVEH plate model is a first bending mode at 76.955 Hz having a 3.75 % difference to 80 Hz obtained experimentally. The fixed boundary condition bluff splitter body is non-contributing at

lower natural modes thus not affecting the displacement shape and natural frequencies value. Natural frequencies only change with respect to the change of geometrical properties, material properties and boundary conditions. The discrepancy in experimental and simulated natural frequency shown in Table 4.1 happens when the three parameters mentioned above used in simulation environment differ from the real structural model. PVEH material properties in real-life may have slight difference as compared with the published material properties used in simulation. Besides, simulation of clamping mechanism of the PVEH plate may have slight difference as compared with the real clamping device. Although these discrepancies occurred, the result with a percentage difference of lower than 5% still can be considered acceptable.

Table 4.1: Difference Result between Harmonic Response Simulation and LDV Experimental Frequency of PVEH Plate

FEM Harmonic Response (Hz)	ESPI (Hz)	Difference (%)
76.9	80	-3.75
480.2	480	0.042
1344.5	1340	0.33
1707.4	1790	-4.614
2384.2	2430	-1.884
3532.5	3590	-1.602

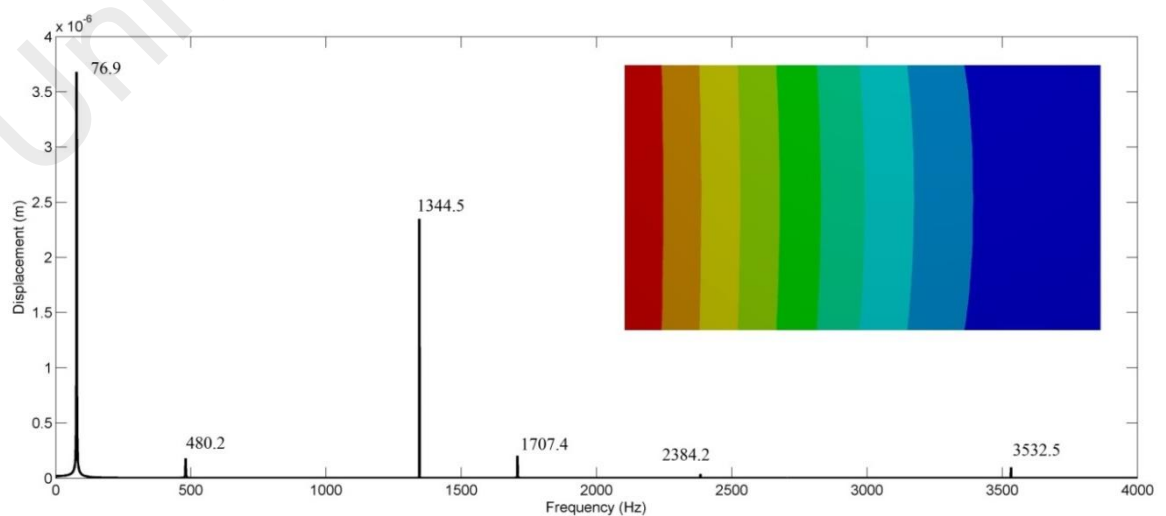


Figure 4.2: Simulated Harmonic Response of PVEH Plate Model

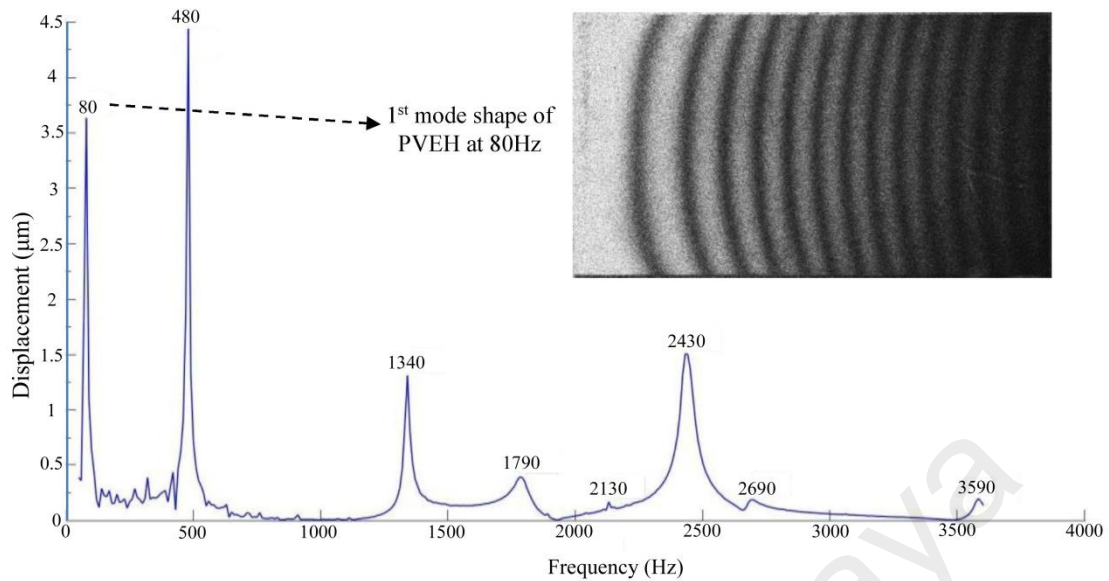


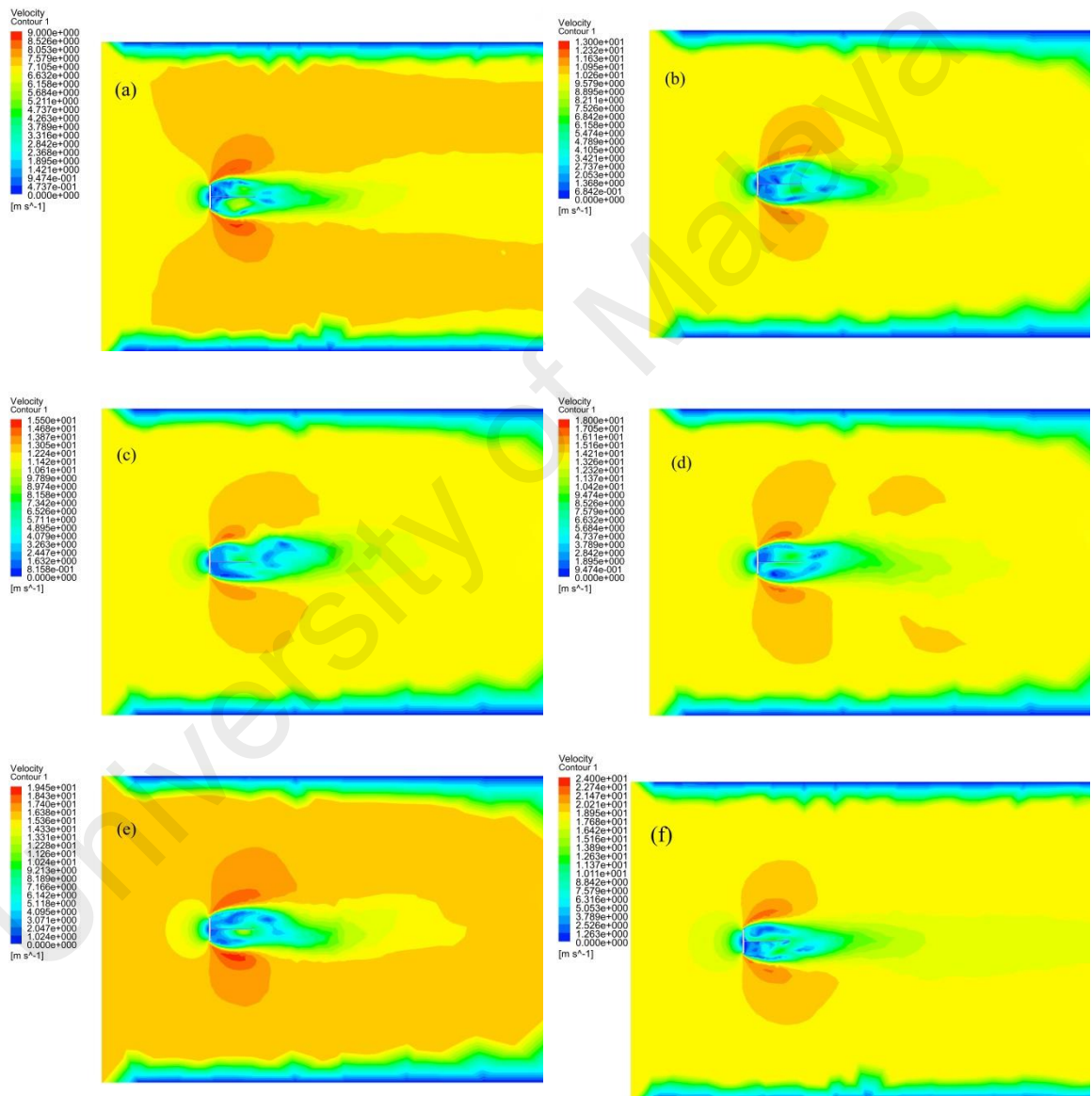
Figure 4.3: Dynamic Characteristic of Piezoelectric Plate Using ESPI

4.1.1.3 Vortex Formation with Different Wind Speed (PVEH Plate)

Results shown in Figure 4.4 (a-j) are velocity contours of 7 m/s, 10 m/s, 12 m/s, 14 m/s, 16 m/s, 18 m/s, 19 m/s, 20 m/s, 22.5 m/s and 25 m/s wind speed at time 0.3 s. It is shown in all figures that with constant fluid flow, either in high or low velocity wind speeds, the structural model is able to generate large area of vortex with the introduction of a bluff splitter body. Contour plots of Figure 4.4 shows flow separation occurrence when fluid is obstructed by an upstream bluff splitter body, leaving a low velocity high pressure vortex region as illustrated in the blue region downstream of the bluff splitter body. It is observed that vortex formation length and pattern generated under all wind speeds are similar. According to P. Bearman (1965), vortex formation length is the length downstream of the model whereby the velocity fluctuation reaches a maximum level. This proves that similar shape and aspect ratio value structural model produces similar vortex formation length and shape disregarding the flow speed.

Vortex generation usually causes wake propagation downstream with certain frequency and pressure force that will excite and damage downstream structures. It is

mentioned by F.J. Huera-Huarte, a rigid plate installed behind a bluff body is able to suppress wake propagation downstream (Huera-Huarte, 2014). It is noted in the contour plots in Figure 4.4 below, by switching a rigid plate to a slightly more flexible PVEH plate in this current research provides additional vibrational tendency to the plate under the influence of vortex and in a degree of generating power while suppressing further wake propagation downstream.



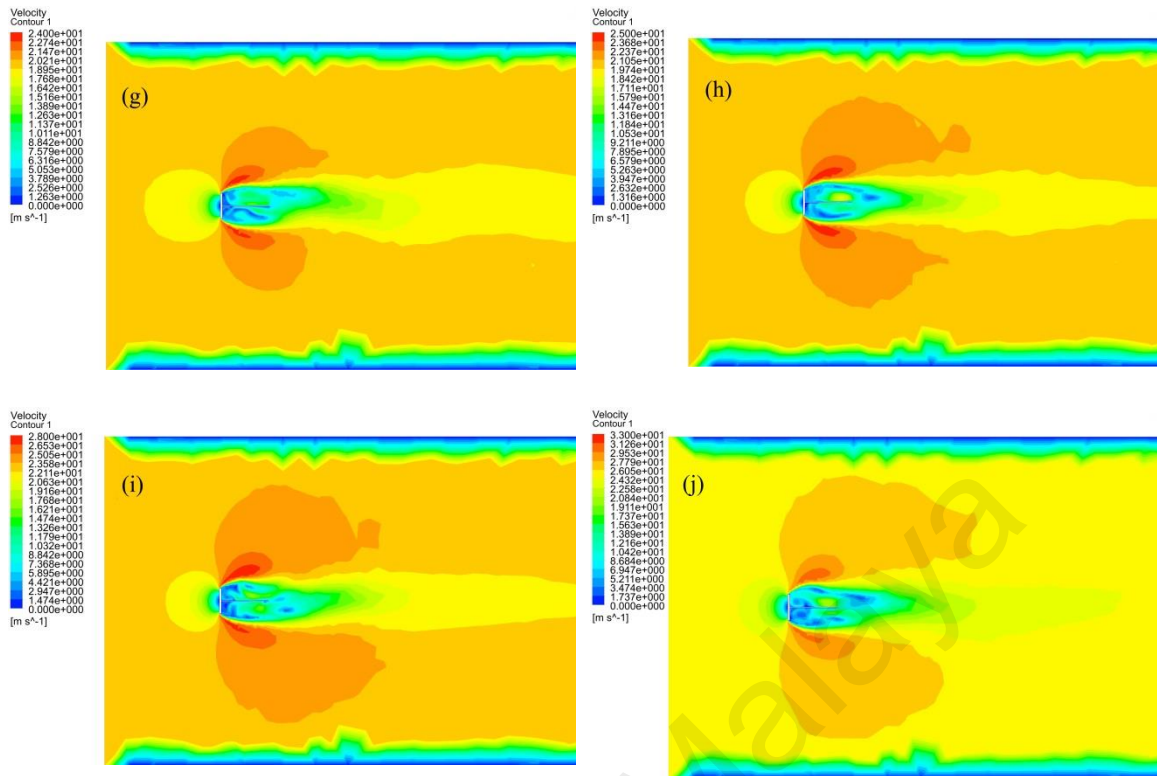


Figure 4.4: Velocity Contour Showcasing Vortex Formation at 0.3s at wind speed of (a) 7 m/s (b) 10 m/s (c) 12 m/s (d) 14 m/s (e) 16 m/s (f) 18 m/s (g) 19 m/s (h) 20 m/s (i) 22.5 m/s (j) 25 m/s

4.1.1.4 Fluctuating Lift Force with Different Wind Speed (PVEH Plate)

Fluctuating lift force is referring to the alternating pressure force created by vortex flow acting on the surface of the PVEH plate. Figure 4.5 indicates that with the increase of wind velocity increases the fluctuating lift force acting on the PVEH plate. Referring to Bernoulli's principle, due to a higher flow velocity generating a lower pressure vortex region, larger force is acting on the opposite surface of the plate. Vortex occurrence by nature is unstable, hence fluctuating lift force generated is usually periodic containing a certain vortex frequency after reaching steady condition. Equation 2.1 denotes that with similar model, larger wind speed generates higher vortex frequency as a result of higher rate of alternating lift force acting on the PVEH plate. Vortex frequency heavily influences the vibrational frequency and amplitude of the PVEH plate explained latter in Section 4.5.

Graph of lift force induced under 19 m/s wind speed (Figure 4.6) displays that the amplitude of lift force acting on the PVEH is strongly fluctuating. This phenomenon is

determined to be caused by two reasons. First, the simulation research is done with a three dimensional domain instead of a usual 2D or 3D symmetrical domain which is widely used in most of the simulation research. The three dimensionality of the flow causes fluctuations in lift force applied on the PVEH model, as tip flow vortex generated at front and back edge of the model exerts different directional force and frequency that disrupts the main vortex flow created from side edge of the structure. Tip speed flow cannot be observed via 2D or symmetrical 3D simulations therefore occasionally being ignored by researchers. Although the contribution of tip speed vortex is small, it brings substantial effect on the flow amplitude and steadiness. The second reason is that the fluid flow is located at a high turbulence region of Reynolds number (Re) of $2.33E+05$ to $3.24E+05$. Referring to Figure 2.4, a high turbulence flow consists of high fluctuations in value and uncertainties causing much vortex fluctuations formed around the body.

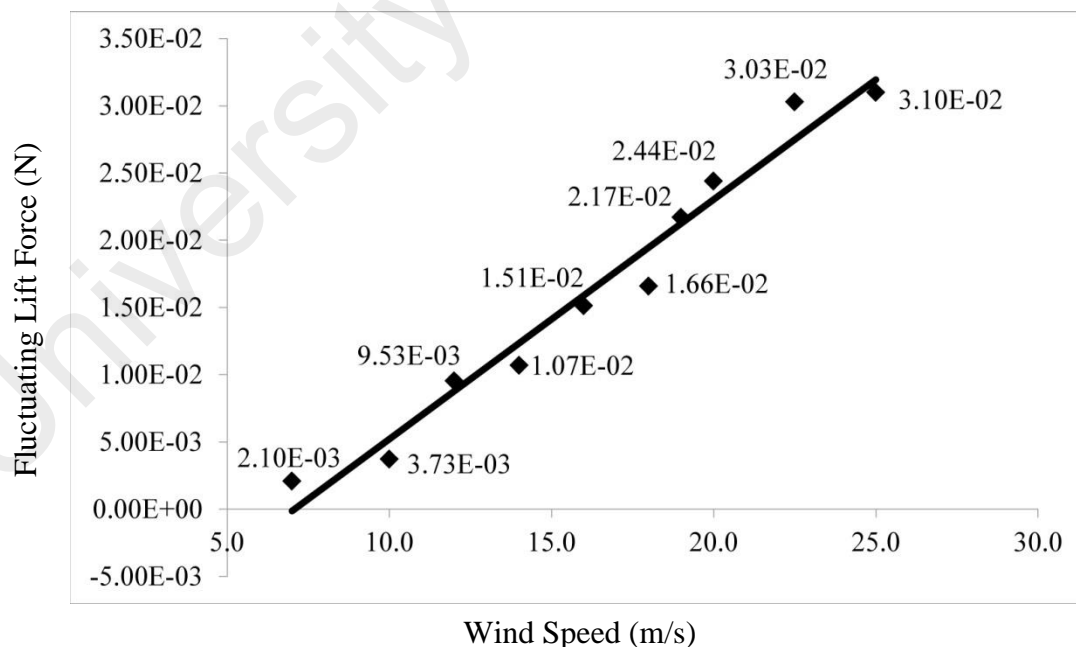


Figure 4.5: Graph of Lift Force Acting on PVEH plate (N) Under Different Wind Speed (m/s)

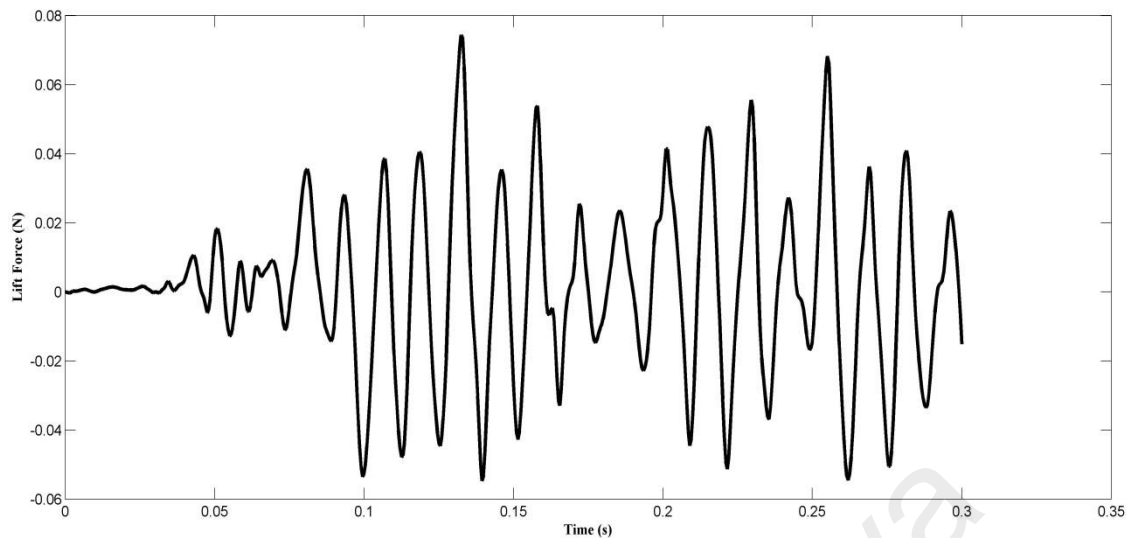


Figure 4.6: Time Domain Graph of Lift Force Acting on PVEH Plate under Wind Speed = 19m/s

4.1.1.5 Vortex Induced Vibration with Different Wind Speed (PVEH Plate)

Mentioned in 4.1.1.4, it is proven in Table 4.2 that wind speed magnitude is contributing proportionally to the vortex and vibrational frequency of the model, as higher velocity wind speed induces higher vortex frequency. A structure's vibrational frequency usually locks-in to the vortex frequency generated, hence the vortex frequency value has a high impact towards the resultant vortex induced vibration amplitude of the PVEH plate.

Structural resonance is a natural phenomenon defined as maximum structural vibration amplitude when vibrational frequency of the structure lies near or coincides to the model's natural frequency. Referred to Section 4.1.1.2 and Table 4.2, as the resultant vibrational frequency lies between 20 Hz and 100 Hz, therefore only the first 2 modes are relevant. Displayed in Figure 4.7, the trend of vibrational amplitude against wind speed is a bell curve with vibrational amplitude increases with the increase of wind speed until it reaches the highest point during 19 m/s wind speed before proceeds to decrease. This phenomenon can well be explained by structural resonance theory because when vortex or vibrational frequency is near to the model's natural frequency,

higher vibrational amplitude is being produced. Vortex frequency of 75.758 Hz produced at 19 m/s is almost similar to the model's natural frequency of 76.9 Hz, resonance occurred producing highest VIV amplitude with 2.09 mm and a RMS value of 1.26 mm. At wind speed lower or higher than 19 m/s, it is noted that a decrease in VIV amplitude because the vortex frequency values generated shy away from the model's natural frequency. Hence, 25 m/s wind speed having vortex frequency of 100 Hz is far away from the model's natural frequency and receives a less contribution of the vibrational mode and hence vibrating at relatively lower VIV amplitude although having a higher level of fluctuating lift force.

It is noted in this research that vortex frequency is more influential than lift force in affecting the vortex induced vibration amplitude. Although higher wind speeds of 20 m/s, 22.5 m/s and 25 m/s produced larger lift force acting on the surface of the flexible PVEH plate, the vibrational amplitude generated is not as high as 19 m/s wind speed as vortex frequency produced does not resonate with the model's natural frequency. Referring to Figure 4.7, RMS vibrational amplitude of PVEH plate increased by a margin of 49.76 % on 19 m/s with 1.26 mm compared to 20 m/s with 0.63 mm. It can also be compared between 20 m/s and 22.5 m/s whereby 20 m/s wind speed produces VIV with RMS amplitude 0.63 mm while 22.5 m/s wind speed only achieves 0.26 mm although the latter applies 0.03N more lift force. 20 m/s wind speed produces vortex frequency of 80.808 Hz which is nearer to the fundamental frequency of 76.9Hz compared to 22.5 m/s wind speed with vortex frequency of 82.418 Hz.

25 m/s wind speed result shows slight twisting in structure's vibrational pattern compared to 19 m/s wind speed result shown in Figure 4.8 which is a pure bending mode. This is because with 100 Hz vortex frequency value by 25 m/s wind speed moves away from the model's fundamental frequency but starting to approach the structure's second natural frequency of 480.2 Hz, creating slight contribution of second vibrational mode

or the first twisting mode towards the vibrational pattern although the first bending mode is still dominating the overall vibrational pattern.

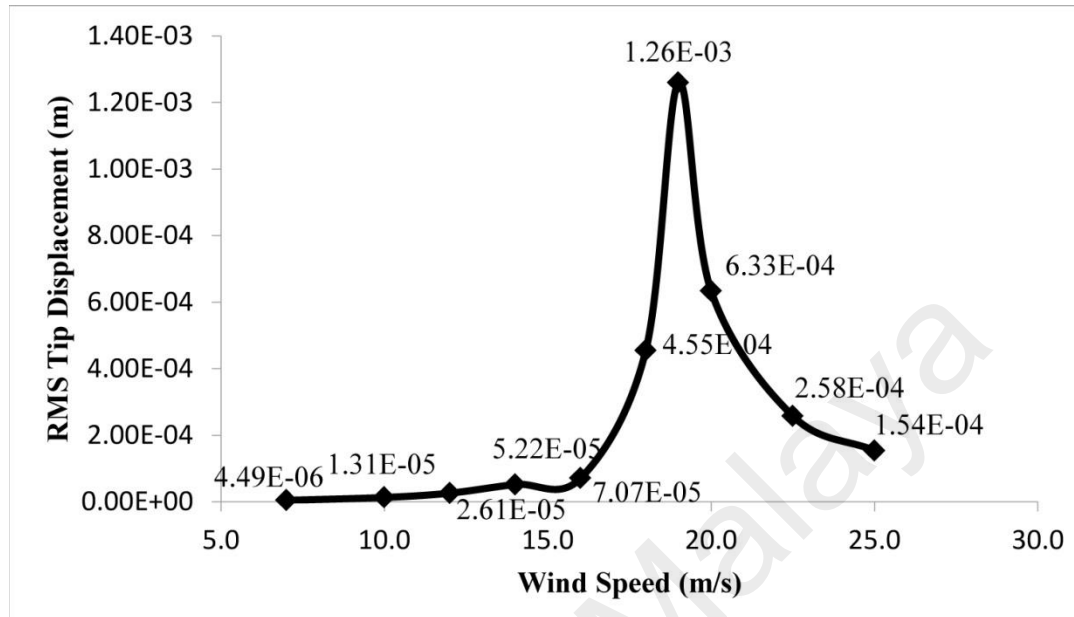


Figure 4.7: Graph of Vibrational Amplitude of the PVEH Plate (m) under Certain Excitation Vortex Frequency (Hz)

Table 4.2: Difference between Resultant Vibrational Frequency (Hz) of PVEH Plate and Natural Frequency (Hz)

Wind Speed (ms ⁻¹)	Resultant Frequency (Hz)	Natural Frequency (Hz)	Difference (%)
7.00	20.020	76.9	-73.73%
10.00	30.303		-60.59%
12.00	41.958		-45.44%
14.00	50.505		-34.22%
16.00	60.606		-21.19%
18.00	70.707		-8.05%
19.00	75.758		-1.48%
20.00	80.808		+4.04%
22.50	82.418		+7.18%
25.00	100.00		+30.05%

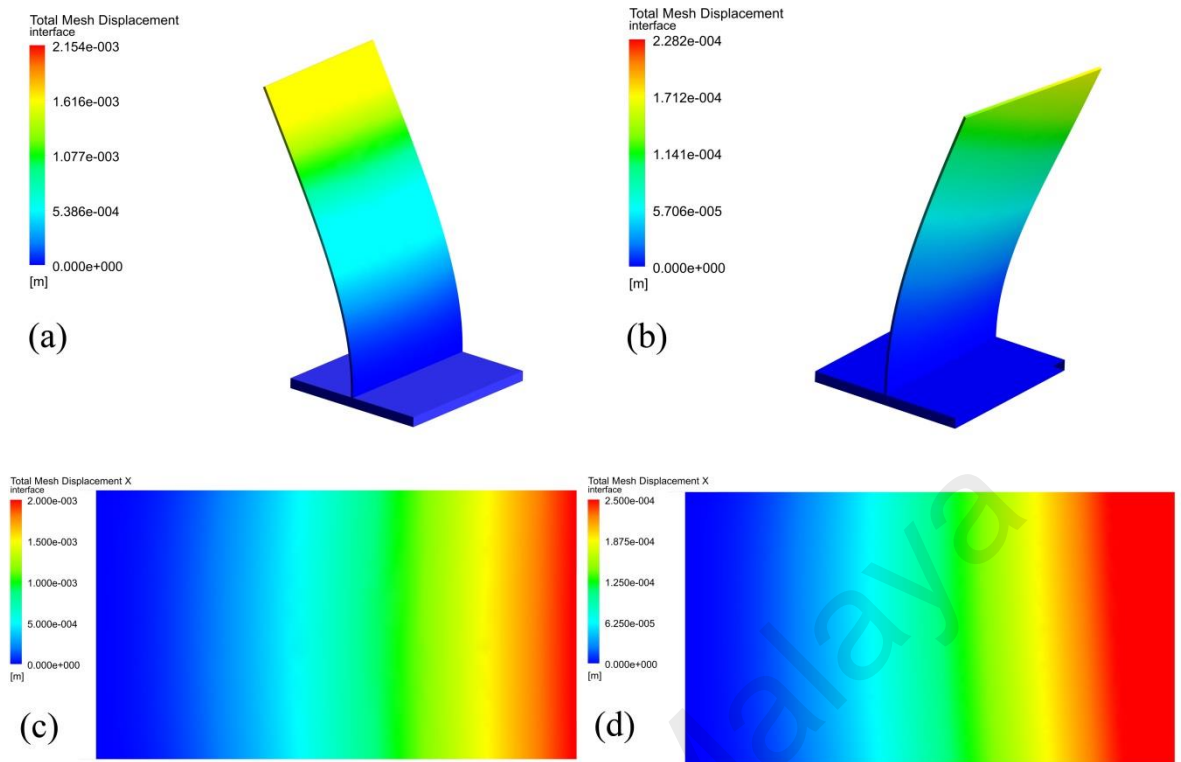


Figure 4.8: Deflection contour of model (a) 19 m/s isometric (b) 25 m/s isometric (c) 19 m/s top (d) 25 m/s top

4.1.2 Coupled Elastic Plate and Bluff Splitter Body Model

This section showcased the results from different wind speed of 0.3 m/s, 0.4 m/s, 0.513 m/s, 0.6 m/s, 0.7 m/s, 1.0 m/s and 1.5 m/s applied onto a coupled bluff splitter body and elastic plate model.

4.1.2.1 Grid Independence Study

Since the structural model applied in both Sections 4.1.1 and 4.1.2 is different, grid independence study has to be carried out on the fluid domain applied in the current research section. Three different minimum grid sizes settings of 0.001 m, 0.0005 m and 0.00025 m is applied on the computational domain each generating 34 956, 98 934, and 337 656 elements. Single Transient CFD analysis with 0.513 m/s wind speed and Large Eddy Simulation turbulence model is conducted and the root mean square (RMS) lift forces obtained for all mesh sizes are computed. The RMS lift force value against the number of elements is displayed in Figure 4.9 shows that the RMS lift force between

0.0005 m mesh size and 0.00025 m mesh size has a difference of 2.86%. This value is under the threshold value and is acceptable as mesh independent. Hence the minimum mesh size of 0.00025 m is applied as the mesh size for the following simulation process done.

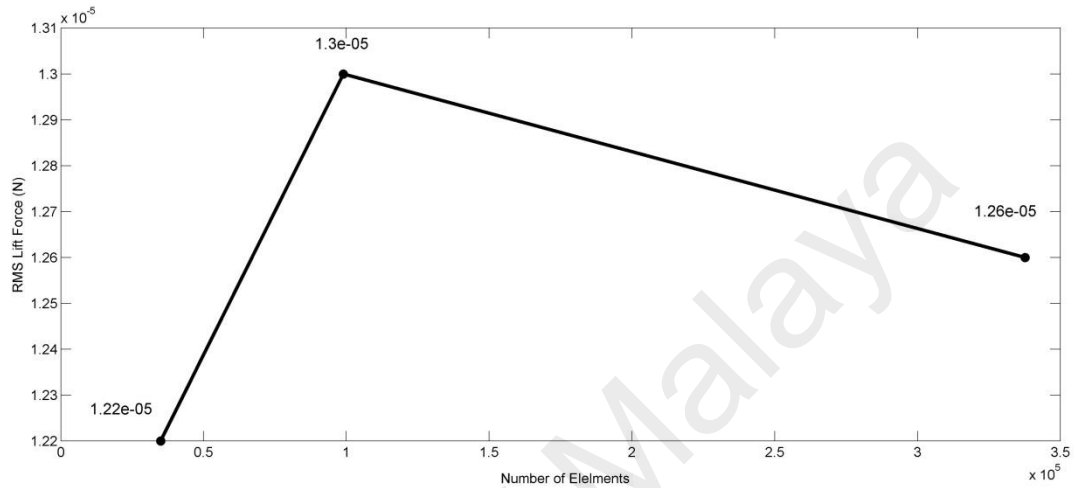


Figure 4.9: Mesh Independence Graph of RMS Lift Force against Number of Elements

4.1.2.2 Numerical Model Validation

In this section, the structural model used is a reference to a vortex induced vibration research conducted by Dettmer. In order to justify the results of present research, FSI numerical method in this research needs to be validated. Dettmer's results in Figure 4.10(a) showcases vibrational frequency ranging from 2.96Hz to 3.31Hz while the tip displacement amplitude has a value in the range of 0.011 m to 0.014 m. The results obtained from the present FSI validation simulation using LES WALE turbulence model and Figure 4.10(b) shows that the vibrational frequency of 3.03 Hz with structural tip displacement amplitude ranging from 0.0106 m to 0.0122 m. Considering the average vibrational frequency of 3.135 Hz from Dettmer's study, the percentage difference in frequency is 3.35% while structural tip displacement percentage difference

is ranged from 3.364 % to 12.86 %. The difference of both results is in an acceptable range thus the numerical model is said to be validated.

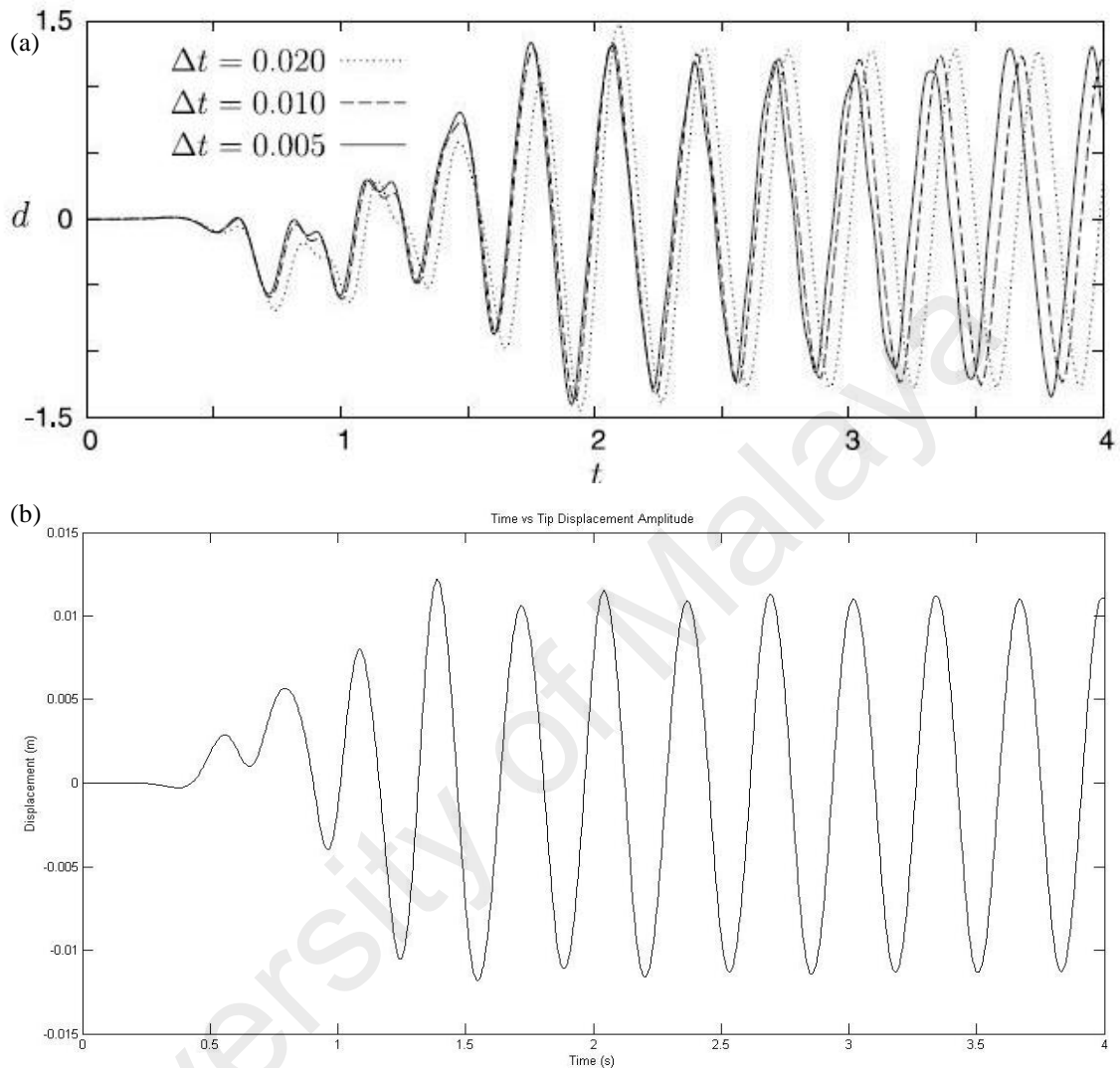


Figure 4.10: Elastic Plate Flow Induced Vibrations Validation: Time Domain Vibrational Displacement of the Tip of the Structure. (a) Different Time Step Sizes (Dettmer et al.) (b) Current Research FSI Simulation

4.1.2.3 Structural Modal Analysis

Section 4.1.1.2 proves that simulated harmonic response is able to decently reproduce all of the natural frequencies of the PVEH model. Henceforth, in this section, the natural frequencies and mode shapes of the coupled bluff splitter body and elastic plate model is simulated in a similar method with results as shown in Figure 4.11. As the wind speed involved in this simulation is relatively low, i.e. from 0.3 m/s to 1.5 m/s, only the first

two natural frequencies are involved in this research section where the first bending mode of 3.087 Hz and the second bending mode of 19.287 Hz. The corresponding mode shapes of the first two natural frequencies are displayed in Figure 4.11 (a) and (b) respectively.

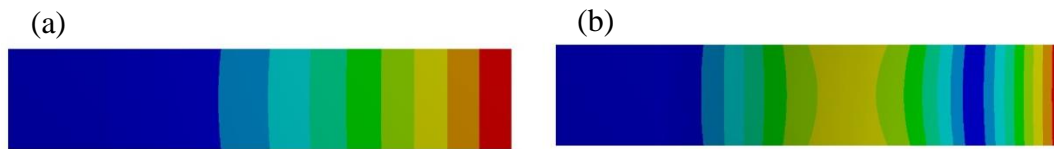


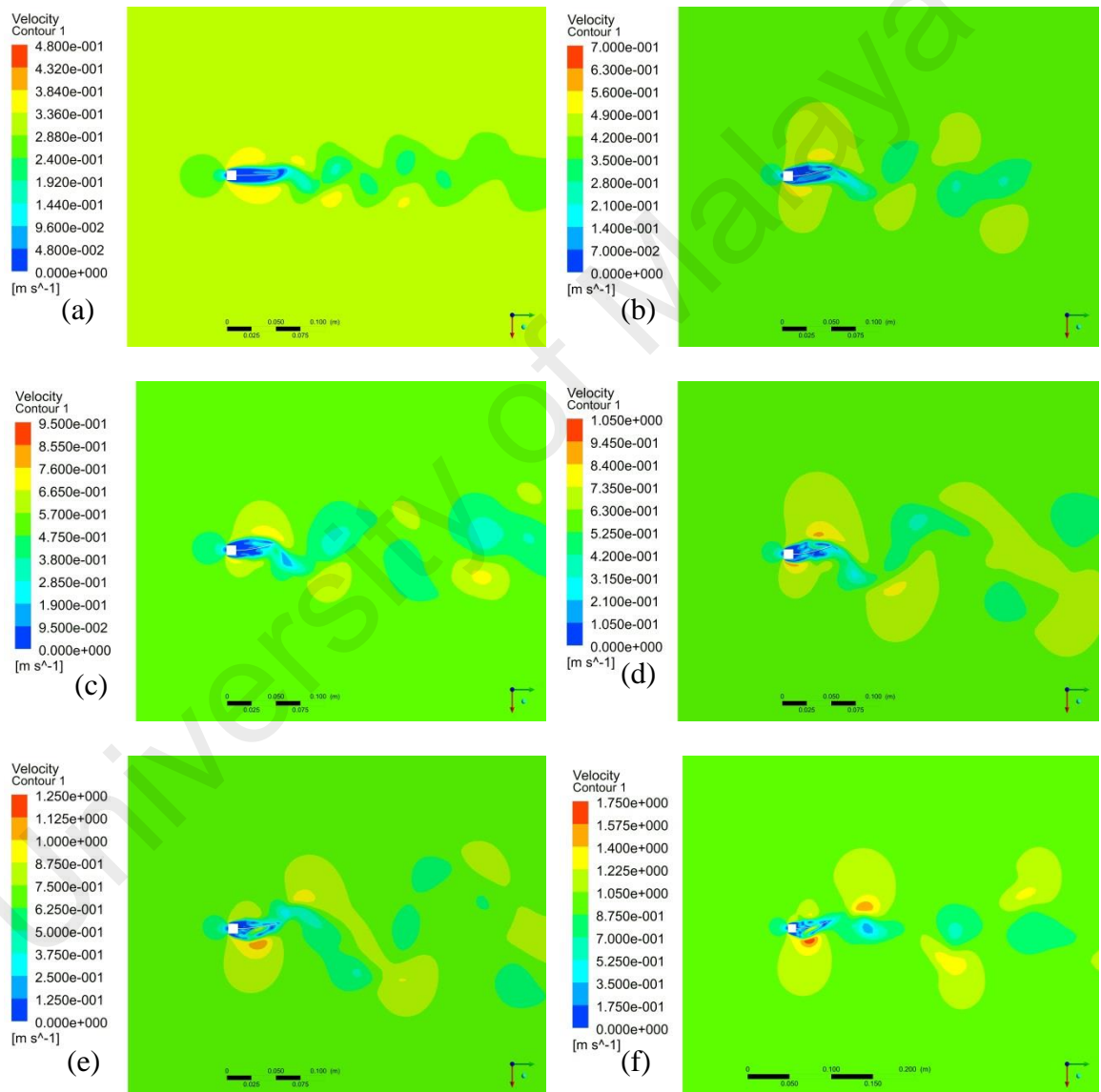
Figure 4.11: Modal Analysis of 1cm Coupled Bluff Splitter Body and Elastic Plate (a) Fundamental Natural Frequency = 3.087 Hz (b) Second Natural Frequency = 19.287 Hz

4.1.2.4 Vortex Formation with Different Wind Speed (Elastic Plate)

Figure 4.12 (a) to (g) shows the velocity contour induced from flow separation by different wind speed ranging from 0.3 m/s to 1.5 m/s. Similar to section 4.1.1.3, a bluff splitter body installed upstream of a flow induces flow separation, causing downstream vortex formation. Dark blue region in the contour that represents vortex formation length is observed to have remained the same throughout the course of wind speed change which is similar to the situation occurred in Section 4.1.1.3. The vortex formation length created by coupled bluff splitter body and elastic plate model is observed to be at similar length as the elastic plate length. Hence, it is proven that vortex formation length is not affected by the fact of varying wind speeds.

Apart from the main vortex formation region surrounding the elastic plate, it is noted that wake propagation is formed downstream of the structural model. Although it is mentioned by Akilli et al. and F.J. Huera-Huarte that a plate fixed behind a bluff splitter body is able to suppress any wake propagation, a rather elastic plate is unable to perform such task effectively as shown in Figure 4.12 (Akilli, Sahin, & Tumen, 2005; Huera-Huarte, 2014). Comparatively, PVEH plate in Section 4.1.1 is much stiffer than

the elastic plate in Section 4.1.2. Stiffer plate is able to suppress wake propagation downstream of the flow while elastic plate is more prone to vibrational motion due to the fact that vortex is able to disrupt downstream flow and forming the wakes. The absence of vortex suppression encourages continuous and periodic force to be applied onto the elastic plate and promotes higher stability VIV.



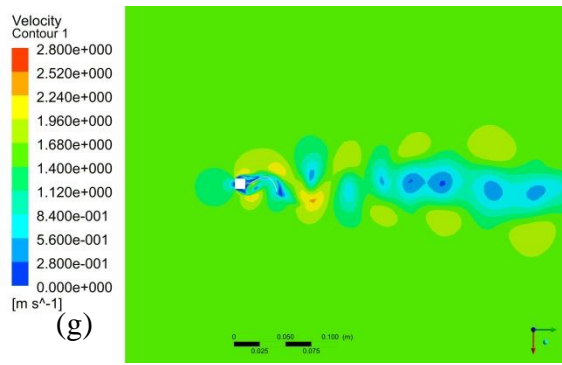


Figure 4.12: Velocity Contour of Vortex Formation under Wind Speed (a) 0.3 m/s (b) 0.4 m/s (c) 0.513 m/s (d) 0.6 m/s (e) 0.7 m/s (f) 1.0 m/s (g) 1.5 m/s

4.1.2.5 Fluctuating Lift with Different Wind Speed (Elastic Plate)

In the present study, the fluctuating lift force acting on the elastic plate increases from $2.26\text{E-}6$ N to $6.73\text{E-}4$ N with the increase of wind speed from 0.3 m/s to 1.5 m/s as shown in Figure 4.13. Explained in Section 4.1.2.4, flow instability due to vortex is creating a periodic lift force acting on the elastic plate. According to Bernoulli's principle, a higher velocity vortex flowing past a bluff splitter body model induced lower pressure region on the model, hence the lift force acting on the opposite surface of the elastic plate increases with the increase of wind speed.

It is shown in this section that although wind velocity value of 0.3 m/s to 1.5 m/s is relatively low, vortex flow is still able to be generated yielding fluctuating lift force. Table 4.3 shows Reynolds numbers calculated from Eq. 2.12 are quite low compared to previous section as a result of low wind speed passing through the bluff splitter body. From literature review of 2.2.4, Figure 2.4 shows that Reynolds number of 150 to 300 is at a transitional to turbulence region, this ensures that the vortex flow produced is in periodic pattern and furthermore producing periodic fluctuating lift force acting on the elastic plate. Thus, lift force in the present section shows a steadier periodic pattern compared to Section 4.1.1.4. Moreover, the flexible elastic plate receives less suppression compared to a metal PVEH plate.

According to Section 4.1.1.4, fluctuating lift force increases proportionally with wind speed. But, due to very high lift force acting on the elastic plate at 1.5 m/s wind speed, the vibrational pattern is not synchronized with the first vibrational mode probably due to non-linearity and thus the fluctuating lift force produced by this wind speed is not proportional with the remaining results obtained.

Table 4.3: Reynolds Number of Vortex Shedding with Different Wind Speed.

Wind Speed (m/s)	Reynolds Number
0.3	2.03E+02
0.4	2.70E+02
0.5	3.38E+02
0.6	4.05E+02
0.7	4.73E+02
1.0	6.76E+02
1.5	1.01E+03

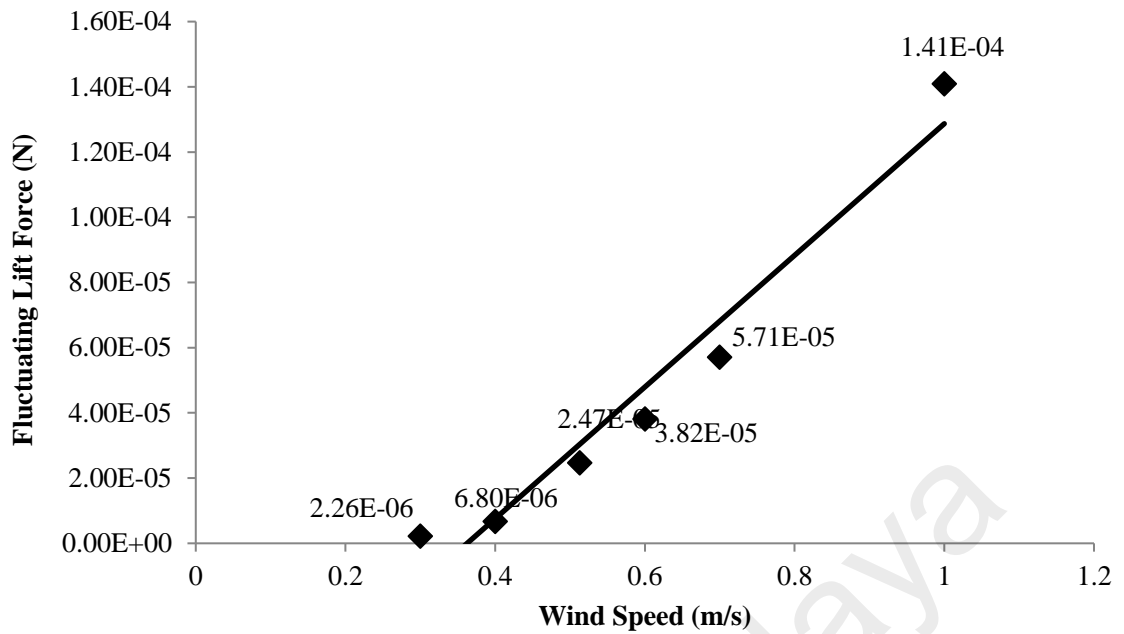


Figure 4.13: Graph of Lift Force against Wind Speed of Coupled Elastic Plate and Bluff Splitter Body Model

4.1.2.6 Vortex Induced Vibration with Different Wind Speed (Elastic Plate)

Figure 4.14 illustrates the vortex induced vibration magnitude of coupled bluff splitter body and elastic plate model increases steeply from 0.3 m/s to 0.7m/s and remains almost the same during 0.7 m/s, 1 m/s and 1.5m/s.

Table 4.4 displays the difference between vortex frequency and the natural frequency of the model. Vortex frequency becomes closer to the natural frequency of the model when wind speed increases from 0.3 m/s to 0.513 m/s and becomes further away when wind speed increases from 0.6 m/s to 1.5m/s. Vortex frequency by 0.513m/s wind velocity is the closest to the first natural frequency of the model with a 1.8% difference.

Referring to Section 4.1.1.5, the closer the vortex frequency is to the natural frequency of the model, the larger is the magnitude of VIV. However, in this study it is shown in Figure 4.14 that the maximum tip displacement occurs during 1.5 m/s followed by 0.7 m/s which both wind speeds do not produce vortex frequency that is

close to the natural frequencies of the structural model. This can be explained through the following reasoning. In Section 4.1.1, the structural model is a PVEH plate with stiffer material properties compared to an elastic plate with relatively less stiff material properties plate used in this section. For the stiffer PVEH plate, the change in lift force is minimal and it does not cause a drastic change in the structure's VIV displacement magnitude. Closeness of vortex frequency to the structure's natural frequency creates resonance lock in which is the main factor that dominates the VIV magnitude in PVEH plate. On the hand, the elastic plate used in this section has a highly elastic material property and thus increasing the fluctuating lift force over wind speed. This has larger contribution and impact towards the VIV magnitude than the contribution from the closeness of vortex frequency to the natural frequency of the model. Although 0.7 m/s wind speed is 27.6 % away from the natural frequency of the model, it has 17.43% larger RMS tip displacement magnitude due to 56.74 % higher lift force compared to 0.513 m/s wind speed that is 1.8% away from the natural frequency of the structural model. . Nevertheless, closeness of vortex frequency is still a dominant factor in determining the magnitude of VIV. Comparing the case of 1 m/s and 0.7 m/s, although 1 m/s wind speed produces 59.5 % higher fluctuating lift force, it has 3.75 % less tip displacement amplitude than 0.7 m/s wind speed. This is due to 1 m/s wind speed has a larger 57.1% vortex frequency deviation from the first natural frequency.

1.5 m/s wind speed case shows a slight increase in tip displacement amplitude compared to 1 m/s and 0.7 m/s case. This is because 1.5 m/s wind speed has a higher fluctuating lift force value while also produces vortex frequency of 15.15 Hz which is near to the second natural frequency of the model, i.e. 19.287 Hz with a difference of 21.4%. It is proven through observation of the structural model's displacement contour shown in Figure 4.12(e), (g) and Figure 4.15, VIV pattern at 0.7 m/s is similar to a first bending mode as it is near to the first natural frequency of the model, while for VIV

pattern at 1.5 m/s, plate displacement shows contribution from both first and second bending mode as it is approaching the second natural frequency of the model at 19.287 Hz.

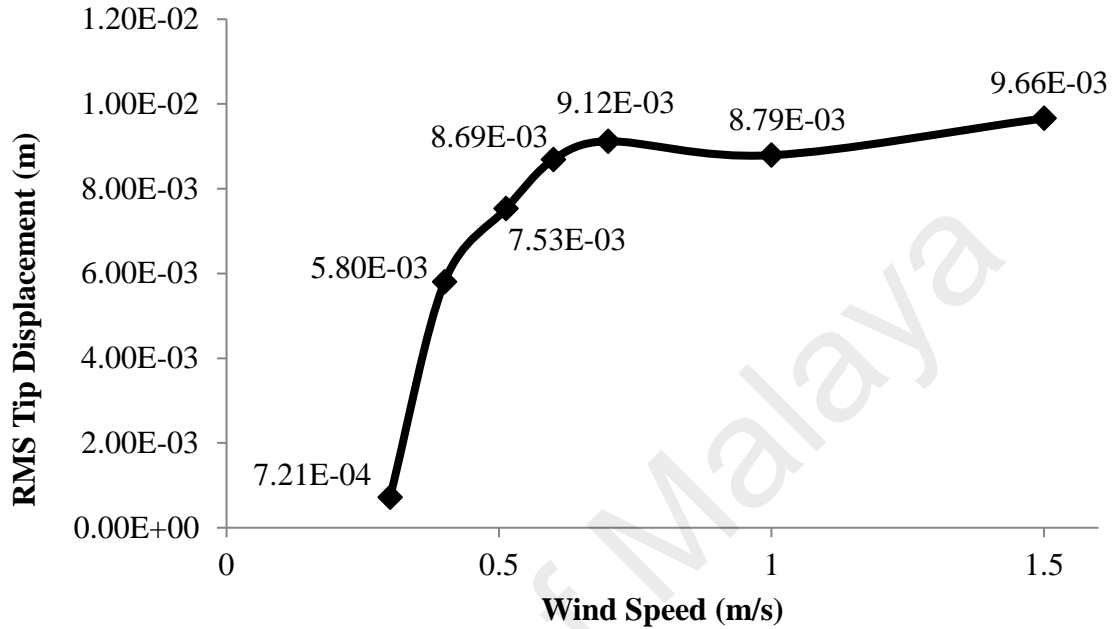


Figure 4.14: Graph of RMS Tip Mesh Displacement against Wind Speed with Coupled Elastic Plate and Bluff Splitter Body Model.

Table 4.4: Table of Resultant Vibrational Frequency to Natural Frequency of Coupled Elastic Plate and Bluff Splitter Body Model.

Wind Speed (ms ⁻¹)	Resultant Frequency (Hz)	Natural Frequency (Hz)	Difference (%)
0.3	2.564	3.087	16.9
0.4	2.797		9.4
0.513	3.030		1.8
0.6	3.290		-6.6
0.7	3.940		-27.6
1.0	4.850		-57.1
1.5	15.150		19.287

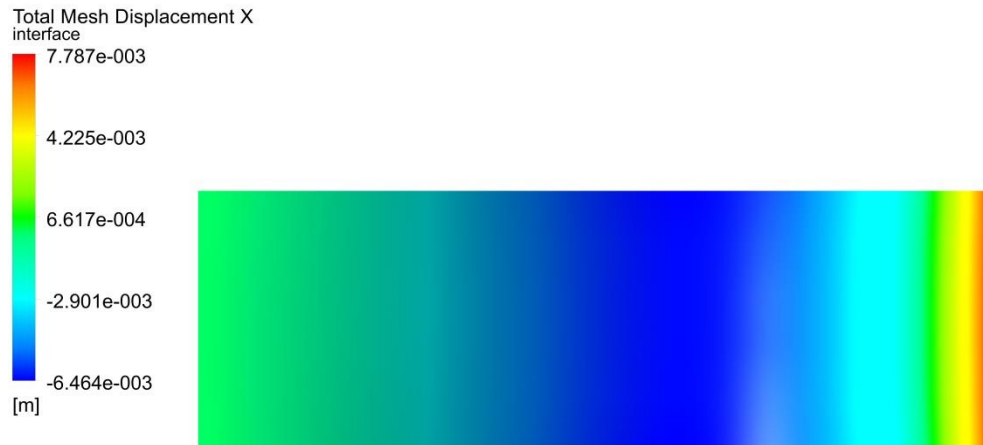


Figure 4.15: Deflection Contour of Structural Model at 1.5 m/s wind speed

4.1.3 Summary (Wind Speed Variance)

It is realized that increasing wind speed increases the fluctuating lift force acting on the cantilever plate, But in order to generate the highest vibrational amplitude, wind speed that had the closest vortex frequency compared to the natural frequency of the model was able to achieve it i.e. 19 m/s in Section 4.1.1 and 0.7 m/s in Section 4.1.2

4.2 Effect of Coupled Elastic Plate and Bluff Splitter Body Aspect Ratio on Vortex Induced Vibration Enhancement

Aspect ratio (D/L) in this section is the ratio of width of the bluff splitter body to the length of the elastic plate. One of the sections focused on changing different bluff splitter body width while the other section had variant elastic plate length.

4.2.1 Bluff Splitter Body Width Difference

In this section, different bluff splitter body widths including 0.005 m, 0.01 m, 0.02 m, 0.03 m, 0.04 m, 0.06 m and 0.08 m are applied while coupled with elastic plate length of 0.04 m.

4.2.1.1 Modal Characteristic Analysis of Model with Different Bluff Splitter Body Size

Modal Analysis simulation is performed on all of the structural models and it is realized that the natural frequencies for all lower modes remain the same for all of the structural models. As illustrated in Figure 4.16, the fundamental natural frequency for both models with 0.01 m bluff splitter body which is tested in previous section and 0.08 m bluff splitter body is similar at 3.087 Hz. The reason is that the bluff splitter body in the current research is a solid body with fixed boundary condition at one of the elastic plate's end. Therefore, the first natural frequency of the elastic plate and its corresponding mode shape remain the same with different width of bluff splitter body.

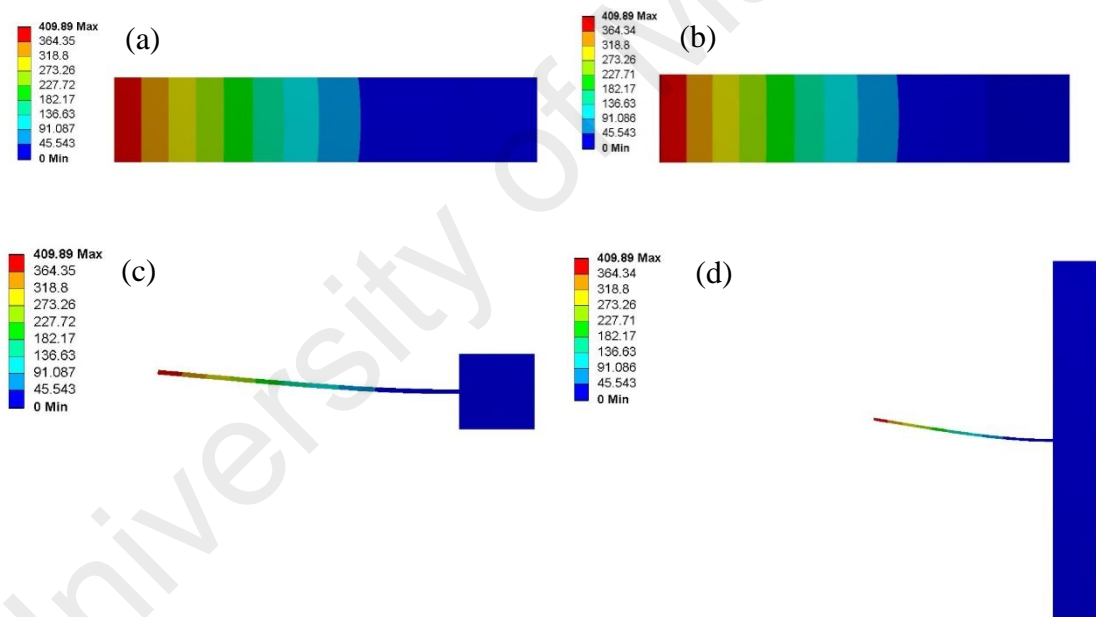


Figure 4.16: First Bending Mode of Coupled Bluff Splitter Body and Elastic Plate Model at 3.087 Hz with Bluff Splitter Body Width of (a) 1cm (Top View) (b) 1cm (Side View) (c) 8cm (Top View) (d) 8cm (Side View)

4.2.1.2 Vortex Street Formation of Different Bluff Splitter Body Sizes

Attachment of a bluff splitter body had been proven effective in generating good quality vortex from flow separation in Section 4.1. By changing the width of the bluff splitter body, factors such as vortex formation length, fluctuating lift force and vortex frequency

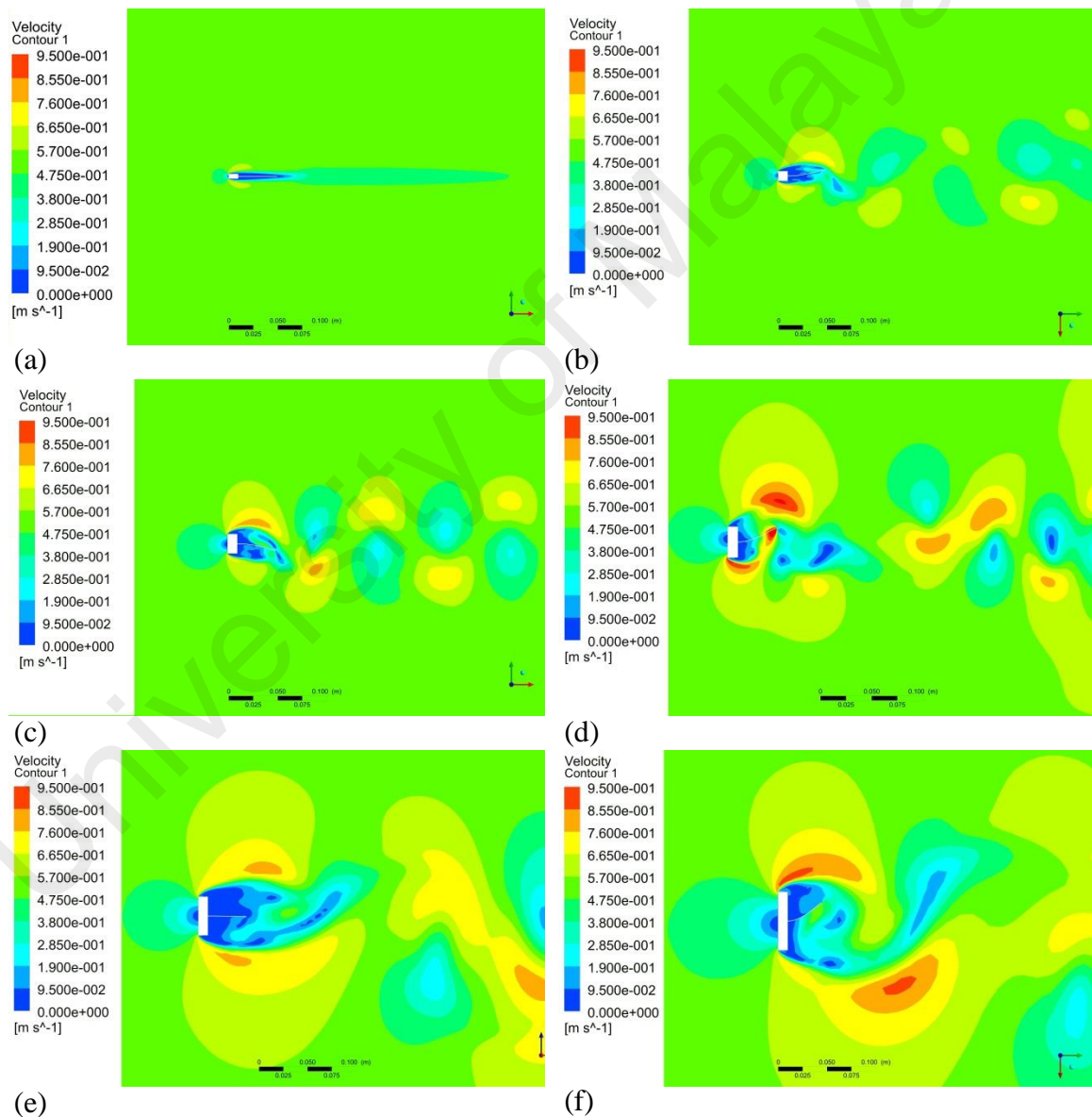
are all affected. Figure 4.17 clearly displayed the vortex formation pattern when coupled with different width of bluff splitter bodies.

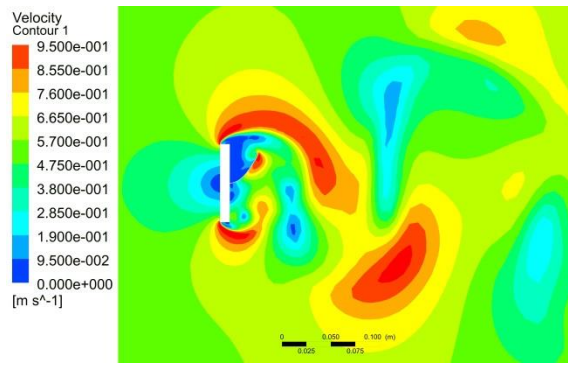
Figure 4.17(a) shows that with small bluff splitter body width of 0.005 m ($D/L = 0.125$), vortex induced from flow separation is fairly weak and the vortex formation length is quite short thus the condition is not fulfilled to create vortex induced vibration. The short width of bluff splitter body forms vortex near to the root of the elastic plate, hence the weak vortex created by flow instabilities is suppressed by the long elastic plate while unable to induce vibrational motion towards it. Wider bluff splitter body of width 0.01 m, 0.02 m, 0.03 m, 0.04 m, 0.06 m and 0.08 m with D/L ratio = 0.25, 0.5, 0.75, 1, 1.5 and 2 respectively shown in Figure 4.17(b)-(g) produce visible and better quality vortex deducing that larger bluff splitter body are better at flow separation and furthermore generating VIV.

In Figure 4.17, the vortex formation length is illustrated as the dark and light blue region enclosed within the initial high velocity flow or red and yellow region beside the bluff splitter body. It is shown that vortex formation length increases proportionally to the width of the bluff splitter body applied. The 0.005 m bluff splitter body model is observed to have minimal vortex formation length which occurs only by the root of the elastic plate while vortex formed with 0.01 m, 0.02 m and 0.03 m bluff splitter body model is mainly by the side of the elastic plate. With shorter vortex formation length, the vortex region is formed at the side of the elastic plate without exceeding the plate's length. Vortex induced vibration observed in these three bluff splitter body width is more periodic.

Bluff splitter body of width 0.04 m, 0.06 m and 0.08 m are noticed to have longer vortex formation length exceeding the length of the elastic plate. Presented in Figure 4.17(e)-(g), as vortex formation length exceeds the elastic plate, it is unable to

contain vortex region within both sides of the elastic plate therefore vortex from one side of the plate will interact with the other side resulting in lift force, vortex frequencies and tip displacement disruptions. Catastrophic flow mentioned above when vortex formation length is longer than the elastic plate is proven with high velocity, i.e., red and yellow zone cross to the other side of the elastic plate, instead of remaining at each individual side of the structural body. The resulting effects towards fluctuating lift force, vortex frequency and the resultant VIV will be discussed in latter sections.





(g)

Figure 4.17: Vortex Street Formation of Coupled Bluff Splitter Body and Elastic Plate Model with Different Bluff Splitter Body Width of (a) 0.005m (b) 0.01 m (c) 0.02 m (d) 0.03 m (e) 0.04 m (f) 0.06 m (g) 0.08 m

4.2.1.3 Fluctuating Lift of Different Bluff Splitter Body Sizes

At the start of every simulation, fluctuating lift force acting on the elastic plate is unsteady before transitioning into a periodic sine wave. When flow first encounters the bluff splitter body, a sudden change of flow velocity and direction causes drastic change in pressure gradient of flow. Subsequently, flow tends to be unstable and fills up the empty region downstream of the model as vortex. Vortex flow stabilizes as time progresses with the growth of wake downstream and eventually evolves into a steady flow with periodic fluctuating lift force acting on the elastic plate.

Section 4.2.1.2 mentions that 0.005 m case did not produce any significant vortex. Therefore, as illustrated in Appendix C Figure C.3 (i) no significant periodic fluctuating lift force is observed compared to the other cases. Vortex is formed from flow separation with bluff splitter body width of 0.01 m to 0.08 m recognized in Figure 4.17(b)-(h) is proven in Appendix C Figure C.3 (ii – vii) where a certain magnitude of periodic fluctuating lift force is acting on the elastic plate. The effect of different bluff splitter body widths on fluctuating lift force pattern and magnitude acting on the surface of the elastic plate are being monitored.

Figure 4.18 shows that RMS lift force increases proportionally with the increase of the bluff splitter body width. 0.01 m bluff splitter body has a small RMS lift force value of 2.57E-05 N compared to 0.08 m bluff splitter body that applied 8.91E-05 N of

fluctuating lift force onto the elastic plate. By increasing the aspect ratio, (i.e. D/L) from 0.25 to 2, the fluctuating lift force increases by a total of 246.7%. Wider bluff splitter body produces a larger area of low velocity vortex region, hence creating larger high-pressure vortex region and larger fluctuating lift force is then acting on the elastic plate.

In the case of bluff splitter body width and elastic plate length aspect ratio less than 1, (i.e. $D/L < 1$), the fluctuating lift force is increasing at a lower increment, but when aspect ratio is larger or equal to 1, the force applied is observed to be increasing with a larger increment. This is due to the vortex formation length of the model with different aspect ratio values relates to the passive vortex suppression effect as mentioned by (Akilli et al., 2005). Discussed in Section 4.2.1.2, smaller aspect ratio structural model induces smaller vortex region formed at respective sides of the elastic plate. Interaction of elastic plate with shorter vortex formation length only involves vortex that is present at each individual sides of the plate. Hence, an increasing periodic fluctuating lift force value is affected by the vortex region size increment through the increment of bluff splitter body width. Comparatively, as the vortex region gets larger, i.e. $D/L \geq 1$, vortex formation length exceeds the length of the elastic plate, encouraging vortex region from one side of the plate to interact with vortex region on the other side causing a larger increment in fluctuating lift force. The fluctuating lift force generated is observed to have a combination of two different frequencies, i.e. frequency originated from flow separation through bluff splitter body and frequency due to interaction of vortices after the elastic plate length shown in Appendix C Figure C 3 (v – vii).

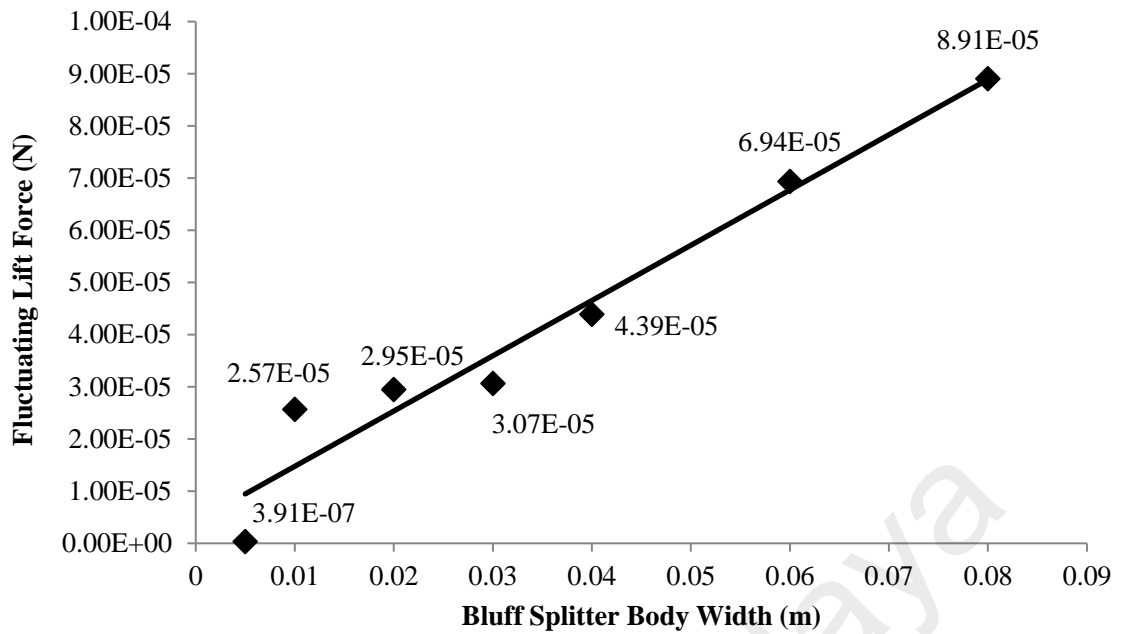


Figure 4.18: R.M.S. Coefficient of Lift Value against Different Aspect Ratio of Bluff Splitter Body-Elastic Plate Couple Model

4.2.1.4 Vortex Induced Vibrations of Different Bluff Body Sizes

Different bluff splitter body widths produce vortex flow with different frequencies and fluctuating lift force resulting in different VIV amplitudes. Without any vortex formation and fluctuating lift force, the elastic plate of 0.005 m bluff splitter body remains almost at the same position without any vibrations displacement occurred on the plate illustrated in Appendix D Figure D 3 (i). As the bluff splitter body width increases, vortex is clearly formed around the model resulting in vortex induced vibrations on the elastic plate shown in Appendix D Figure D 3 (ii – vii).

Section 4.1 mentioned that vortex frequency plays an important role in determining the tip displacement of the elastic plate during vortex induced vibration. Since the model is in lock-in condition where vibrating frequency is equal to the vortex frequency, the bluff splitter body that produces vortex frequency that is near to the models' natural frequency is able to achieve high vibrational amplitude. In Table 4.5, the vortex frequency of aspect ratio, i.e. D/L less than 1 is observed to be around 3.03

Hz to 3.611 Hz which is near to the natural frequency of the model. On the contrary, aspect ratio larger or equal to one has a relatively lower vortex frequency between 1.212 Hz to 1.515 Hz. The drop in vortex frequency values is strongly related to the vortex formation length and the fluctuating lift force induced. Mentioned in Section 4.2.1.3 that a coupled bluff splitter body and elastic plate model that has an aspect ratio of larger or equal to one produces chaotic vortex flow where vortex from each side disrupts each other generating secondary vortex frequency. This has lowered the vortex frequency generated in these bluff splitter body models which is moving away from the model's natural frequency.

The trend line of elastic plate RMS Tip Displacement with different bluff splitter body widths illustrated in Figure 4.19 shows an increase in value from aspect ratios of 0.25 to 0.75. Aspect ratios 1.0 and above experience a drop in tip displacement as compared to aspect ratio value of 0.75 before it increases again when approaching aspect ratio value of 2. The increase in RMS tip displacement value aspect ratio value equal or more than 1 is due to the increase of fluctuating lift force proportionally to the increase of bluff splitter body width as mentioned in Section 4.2.1.3.

Instead of increasing proportionally with the increase of lift force, the tip displacement experiences a drop in value resulting in RMS tip displacement of bluff splitter body width of 0.03 m has a higher value compared to 0.04 m and 0.06 m by 38.36 % and 15.03 %. Resonance theory is able to explain the phenomenon occurred. When the aspect ratio value of the model is less than 1, vortex frequency produced is very near to the natural frequency of the structural model thus the closeness of vortex frequency to the natural frequency of the model is the main contributing factor towards generating high vibrational displacement. However, when the aspect ratio value exceeds the value of 1, vortex frequency produced is away from the natural frequency of the structural model, causing the contribution of the natural mode to be less significant.

While the increment of the resultant tip displacement from case 0.04 m to 0.06 m is solely due to the increase in fluctuating lift force, the tip displacement value is still lower than 0.03 m which has a decent fluctuating lift force and owns vortex frequency near to the first natural frequency of the structural model.

The 0.08 m bluff splitter body has the highest vibrational amplitude of with 1.67E-02 m. But the 0.03 m bluff splitter body can be considered to have the best performance. Comparing 0.08 m and 0.03 m bluff splitter body width, smaller sized 0.03 m and a lower fluctuating lift force of 61.4 % yields vibrational amplitude difference by only 27.6 %. This is because 0.03 m VIV is dominated by the closeness of the vibrational frequency to the model's natural frequency despite having a deficit in lift force compare to 0.08 m bluff splitter body width. In short, in order to create a high VIV amplitude condition, a model had to have a larger bluff splitter body width to elastic plate length aspect ratio and also having the model's natural frequency tuned to the resonant with the vortex frequency generated.

Table 4.5: Vortex and Vibrational Displacement Frequency with Respect to the Aspect Ratio

Bluff Splitter Body Width (m)	Aspect Ratio (D/L)	Vortex Frequency (Hz)
0.005	0.125	0.000
0.01	0.250	3.030
0.02	0.500	3.611
0.03	0.750	3.182
0.04	1.000	1.399
0.06	1.500	1.515
0.08	2.000	1.212

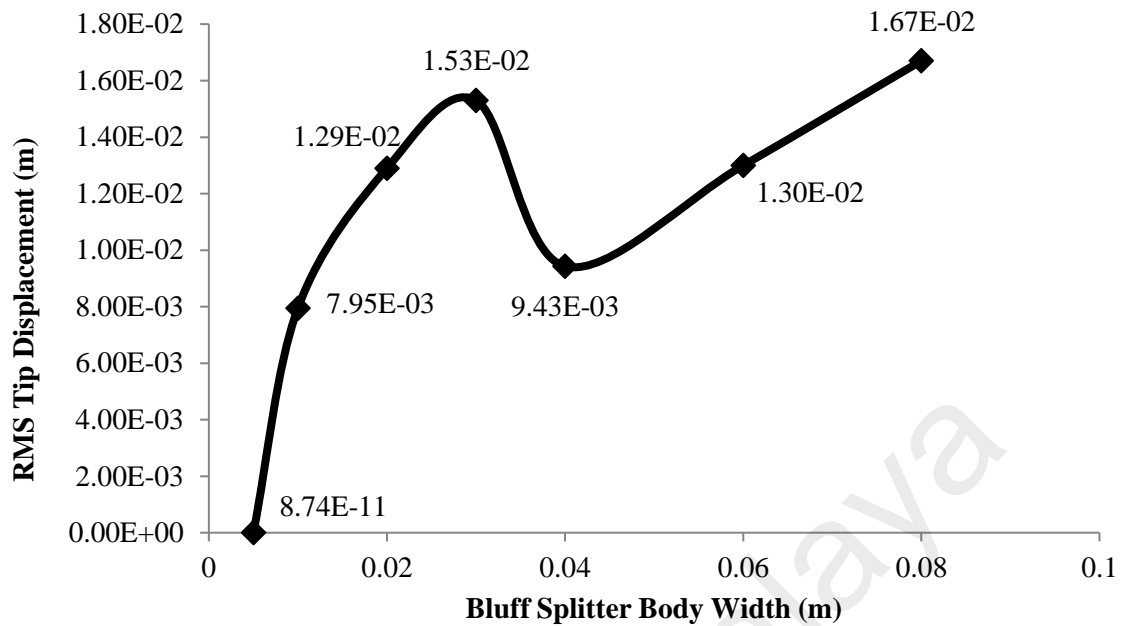


Figure 4.19: RMS Tip Mesh Displacement with Different Bluff Splitter Body Width.

4.2.2 Elastic Plate Length Difference

In this section, the elastic plate length is changed between 0.02 m, 0.03 m, 0.04 m, 0.05 m, and 0.06 m. The results are observed and related towards the effect of aspect ratio difference on the VIV performance.

4.2.2.1 Structural Modal Analysis

Section 4.2.1.1 shows that bluff splitter body with different widths does not affect the structural natural frequency at lower modes. In this section however, the part of the structural model that is varying is the elastic plate fixed with a cantilever boundary condition onto the fixed boundary bluff splitter body. The natural frequency of the elastic plate changes with different elastic plate length. Table 4.6 shows the fundamental natural frequency of different elastic plate lengths. Elastic plate has an increased fundamental natural frequency with the decrease of length because the plate is getting stiffer as the length becomes shorter. Although the fundamental natural frequency for different lengths of elastic plates varies, the fundamental mode shape is similar for

different lengths. Low wind speed velocity of 0.513 m/s is applied in this research, hence second natural frequency and higher is not being considered as vortex frequency will not achieve the value.

Table 4.6: Fundamental Natural Frequency of Different Elastic Plate Length

Elastic Plate Length (m)	Fundamental Natural Frequency (Hz)
0.02	12.499
0.03	5.150
0.04	3.087
0.05	1.970
0.06	1.365

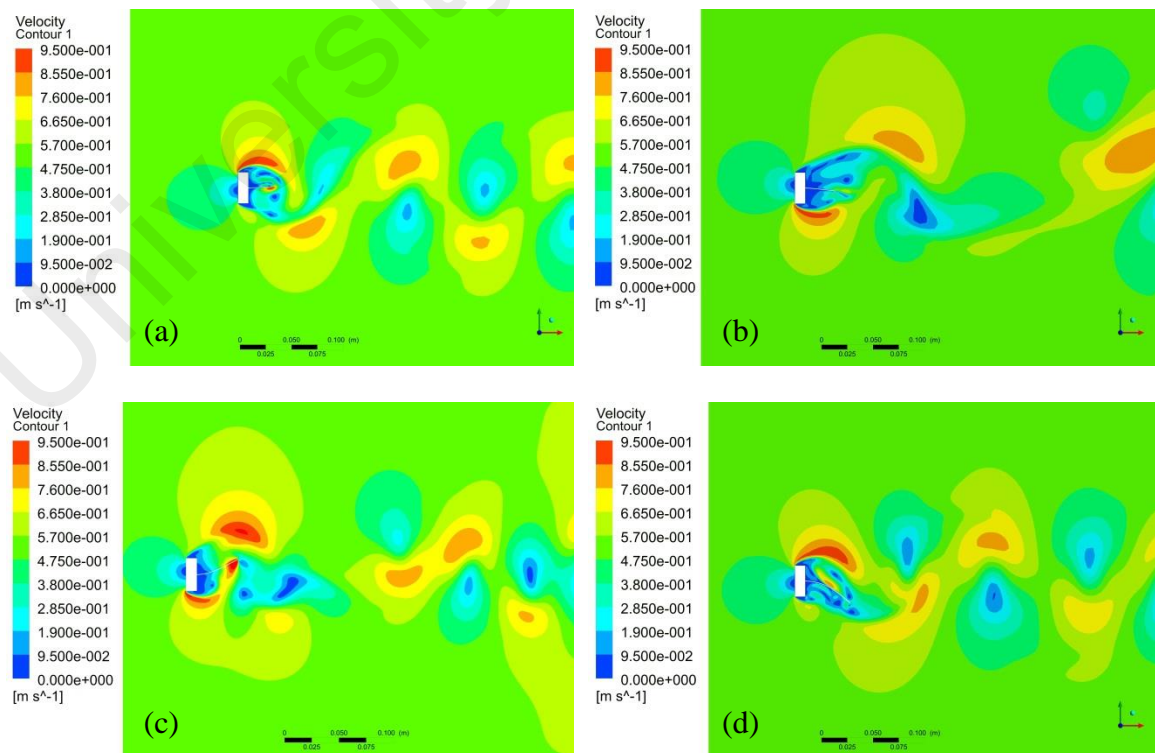
4.2.2.2 Vortex Formation with Different Elastic Plate Length

Aspect ratio of a structural body is an important factor that affects the vortex formation, fluctuating lift force, vortex frequency and the resulting VIV observed in Section 4.2.1. In this section, bluff splitter body width is set at a constant 0.03 m and elastic plate length is varied in order to investigate the effect of the plate length. Shown in Figure 4.20 is the velocity contour of different elastic plate lengths of 0.02 m, 0.03 m, 0.04 m, 0.05 m and 0.06 m with aspect ratio values, i.e. D/L ratio of 1.5, 1.0, 0.75, 0.60 and 0.50 respectively.

Section 4.2.1.2 shows that the vortex formation length increases with the increase of bluff splitter body width. From Figure 4.20, the vortex formation length for all simulated cases is observed to be similar. This is due to the bluff splitter body width is constant at 0.03 m for all of the cases. It is noted that the vortex formation length is affected by the width of the bluff splitter body and not the elastic plate length.

Although vortex formation length is the same for all cases, structure's aspect ratio value still brings an impact on how vortices interact with the elastic plate. Observed in Figure 4.20, when aspect ratio is less than one, the vortex formation length is less than the elastic plate length creating vortex at each respective side of the elastic plate. On the other hand when aspect ratio value is equal or larger than 1, the vortex formation length is longer compared to the elastic plate. Likewise in Section 4.2.1.2, vortex formed travels from one side of the elastic plate to the other and disrupts the vortex on the other side.

In short, these two research sections of 4.2.1 and 4.2.2 show that aspect ratio value larger or equal to one will always cause vortex formation length to exceed the length of the elastic plate, resulting in chaotic vortex flow with interaction of vortex between both sides of the elastic plate. Aspect ratio less than one will have vortex formation length shorter than the plate length ensuring vortices only interact by each individual side of the plate respectively.



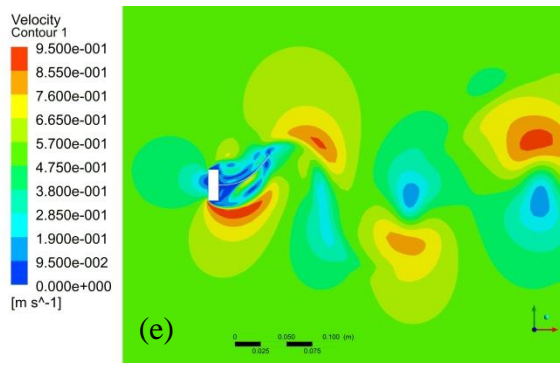


Figure 4.20: Velocity Contour of Vortex Formation with Different Elastic Plate Length (a) 0.02 m (b) 0.03m (c) 0.04m (d) 0.05m (e) 0.06m

4.2.2.3 Fluctuating Lift Force with Different Elastic Plate Length

In Section 4.2.1.3, it is mentioned that the fluctuating lift force increase with the increase of bluff splitter body width or the aspect ratio of the model. In this section, the fluctuating lift force is displayed in Figure 4.21. Noticed from the figure is that with the increase of elastic plate length, the lift force is increased besides having a drop in value in 0.04 m of elastic plate length or aspect ratio value of 0.75. Larger lift force observed acting on a longer elastic plate can well be explained with a larger effective area that came into contact with the vortex flow.

Supposing the values of shorter elastic plate length has a comparably lower fluctuating lift force, but as shown in Figure 4.21, 0.03 m and 0.02 m elastic plate length has fluctuating lift force of $6.75E-5$ N and $4.64E-5$ N respectively which is 119.8% and 51.14% higher than the result obtained by 0.04 m. Vortex formation length is the main reason behind the increase in fluctuating lift force for these structural models. Mentioned in the section above, a model with aspect ratio value equal or larger than one, the vortex formation length exceeds the elastic plate length causing vortex formation to be chaotic and have two frequencies present as with the vortex from one side affecting the other, illustrated in Appendix C Figure C 4 (i) and (ii). This causes the increase in fluctuating lift force because the plate undergoes additional pressure from combination of vortex from flow separation and vortex from opposite side of the elastic plate.

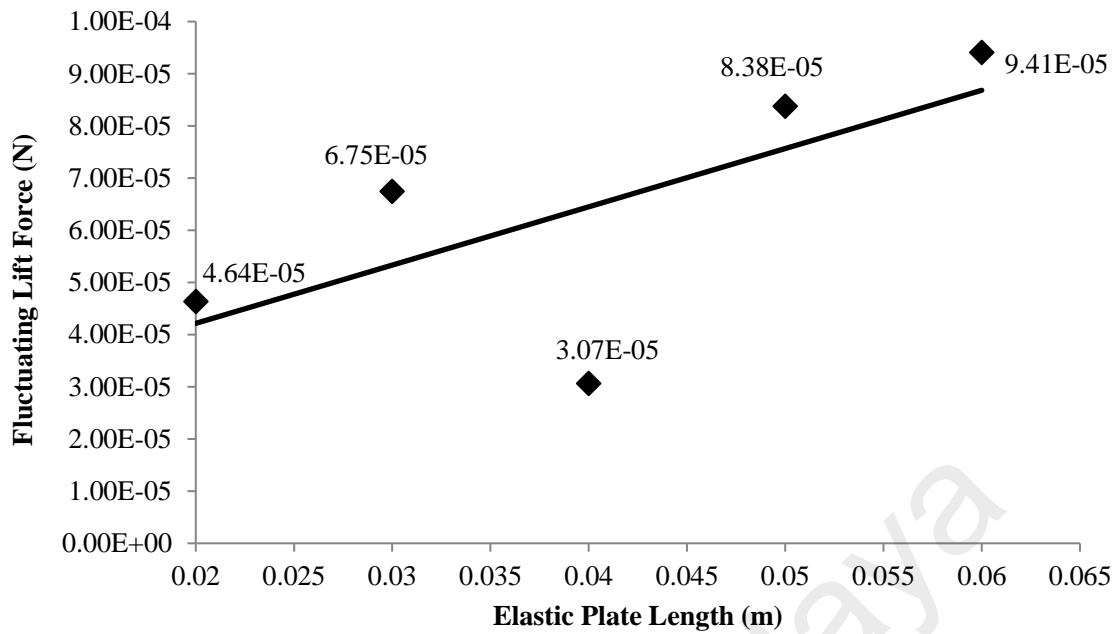


Figure 4.21: RMS Lift Force of Difference Elastic Plate Length

4.2.2.4 Vortex Induced Vibration with Different Elastic Plate Length

From Section 4.2.1.4, bluff splitter body width with aspect ratio value less than one produced vortex frequency near to the natural frequency of structural model. While in Table 4.7, it is observed likewise that with different length of elastic plate, when aspect ratio remains below the value of one, vortex frequency produced is close to the natural frequency of the respective structural model disregarding the wind speed. This shows that vortex frequency produced depends not only on a singular part in a T-shaped structural model, but the overall aspect ratio of the model as it is proven that the length of the elastic plate also interacts and affects the resulting plate VIV.

Following the same pattern, when the aspect ratio value is equal or larger than one, vortex frequency produced drops to a much lower value than the natural frequency of the structural model. Similar to Section 4.2.1.4, the reason behind this event as observed in 4.2.2.2 is the vortex formation length is longer than the elastic plate causing vortex disruption between both sides of the elastic plate increasing the fluctuating lift

force and at the same time reducing the vortex frequency produced where VIV graph over time is shown in Appendix D Figure D 4.

Figure 4.22 shows the tip displacement of different length of elastic plate under VIV. In the graph it is clearly seen that the longer the length of the plate, the vortex induced vibration displacement value will be larger disregarding the vortex frequency and the fluctuating lift force. This is because this simulation records the tip displacement of the elastic plate, hence longer plate having higher elasticity properties has a higher tendency to displace at a larger magnitude compared to shorter plates that are stiffer in elastic properties.

By computing the displacement over length ratios shown in Figure 4.23, the performance of the elastic plate length is able to be evaluated better. Longer elastic plate has a lower aspect ratio values thus having larger displacement to length ratios. This is due to the vortex frequency generated being closer to the natural frequency of the structural model. Aspect ratio of 0.75 has the best performance out of all the different elastic plates simulated because the vortex frequency generated is the nearest to the structure's natural frequency with only 3.077% difference. With 6.497% and 47.985% difference between vortex frequency and natural frequency, the difference in displacement between aspect ratios of 0.6 and 0.5 with aspect ratio 0.75 are 2.1% and 11.3% respectively. Vortex frequency of aspect ratios of 1.0 and 1.5 drift further away from the natural frequency of the corresponding model, the displacement to length ratio value is not ideal with a difference of 54.47% and 87.1% compared to model with aspect ratio of 0.75.

Table 4.7: Vortex Frequency and Difference with Natural Frequency on Different Elastic Plate Length

Elastic Plate Length (m)	Aspect Ratio (D/L)	Natural Frequency (Hz)	Vortex Frequency (Hz)	Difference (%)
0.02	1.50	12.499	2.797	77.622
0.03	1.00	5.150	1.515	70.582
0.04	0.75	3.087	3.182	-3.077
0.05	0.60	1.970	2.098	-6.497
0.06	0.50	1.365	2.02	-47.985

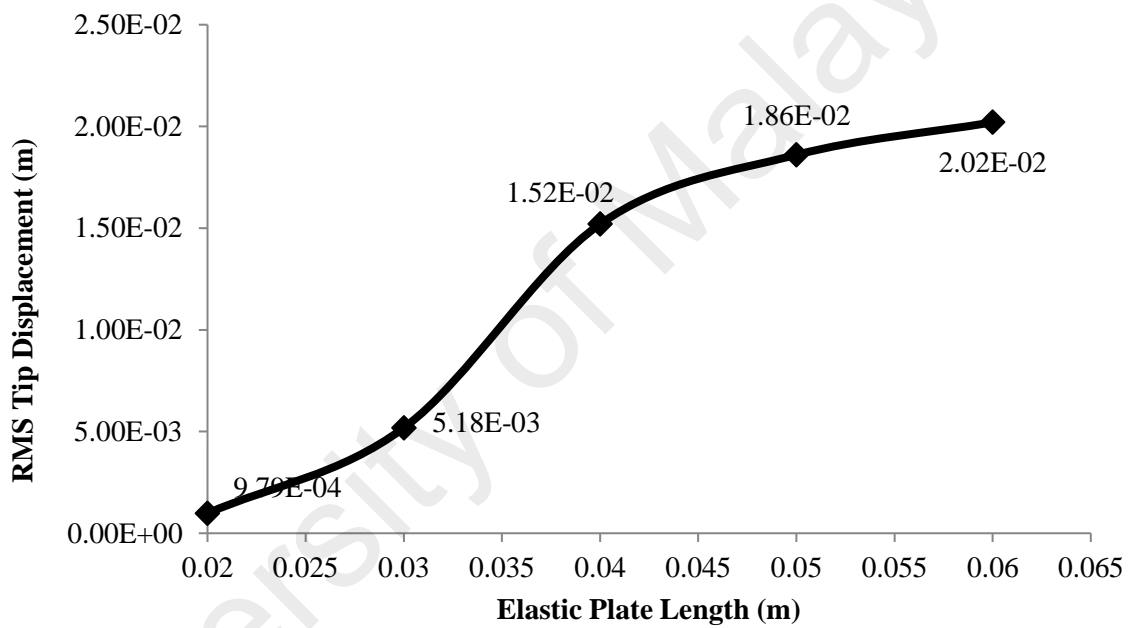


Figure 4.22: Graph of RMS Tip Mesh Displacement against Elastic Plate Length

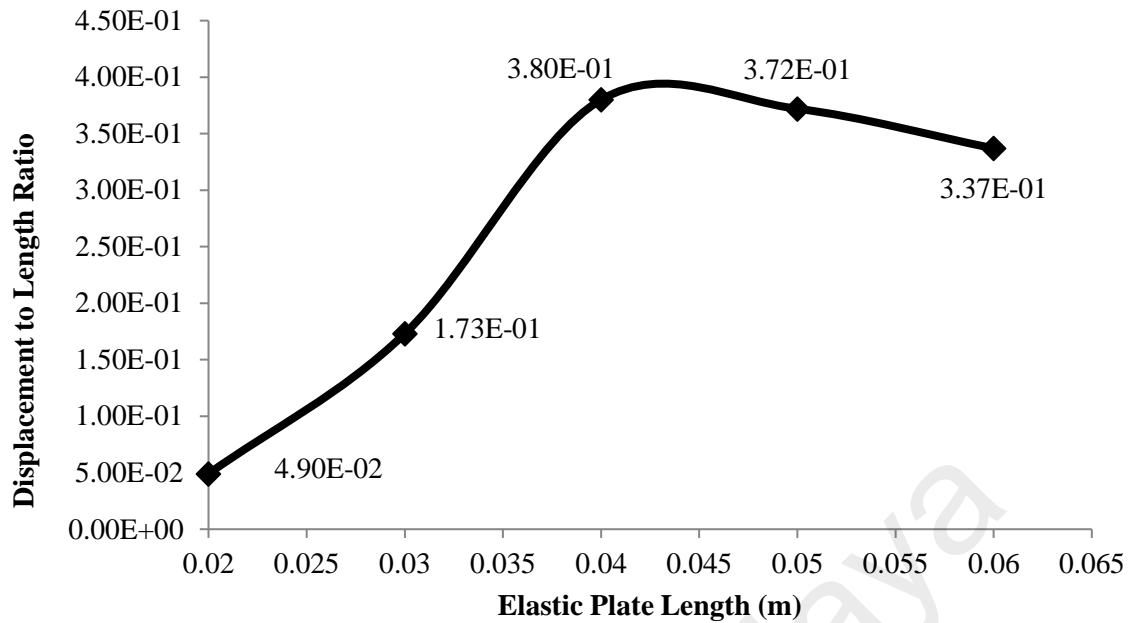


Figure 4.23: Graph of Displacement to Length Ratio against Elastic Plate Length

4.2.3 Summary (Aspect Ratio Difference)

For both sections on width to length (D/L) aspect ratio, fluctuating lift force increases with the increase of aspect ratio value. The best performing aspect ratio shown in both sections is with a 0.03 m bluff splitter body width and 0.04 m elastic plate length, i.e. aspect ratio of 0.75. This coupled bluff splitter body and elastic plate model has the best performance out of other dimensions because the model produces decent fluctuating lift force with wider bluff splitter body width and more importantly, the vortex frequency synchronizes with the natural frequency of the elastic plate model. Moreover, aspect ratio of 0.75 is less than 1; hence vortex interacts with the plate by each individual side without crossing over to the other side. On the other hand, when aspect ratio value is equal or larger than 1, the vortex formation length is longer compared to the elastic plate causing the vortex formed travels from one side of the elastic plate to the other and disrupts the vortex on the other side. Hence, for a coupled bluff splitter body and elastic plate model, aspect ratio of 0.75 provides the best VIV performance.

4.3 Effect of Bluff Splitter Body Design Modification on Vortex Induced Vibration Enhancement

This objective is to investigate the effect when different bluff splitter body designs are applied onto structural model. The first section is conducted using different shapes of bluff splitter body while the second section applied trapezoidal bluff splitter body with different edge angle to observe the resulting VIV performance.

4.3.1 Bluff Splitter Body Cross-Sectional Shapes Difference

In this section, the bluff splitter body with different shapes of Triangle, Trapezoidal, Semicircle, Curve, Diffuser, Rectangular and Circular are investigated.

4.3.1.1 Structural Modal Analysis

It is mentioned in Section 4.2.1.1 that when a bluff splitter body is a fixed solid body, change in dimensions does not affect the lower natural frequencies of the entire structural model. In this section, different bluff body shape designs are tested out. It is realized that with different bluff splitter body shapes, even thin shapes such as Curve I, Curve II, Diffuser I and Diffuser II the first natural frequency and mode shape remains the same with the value 3.087 Hz at its first bending mode respectively. Figure 4.24 (a) and (b) shows the first mode contour of Semi-Circle I.

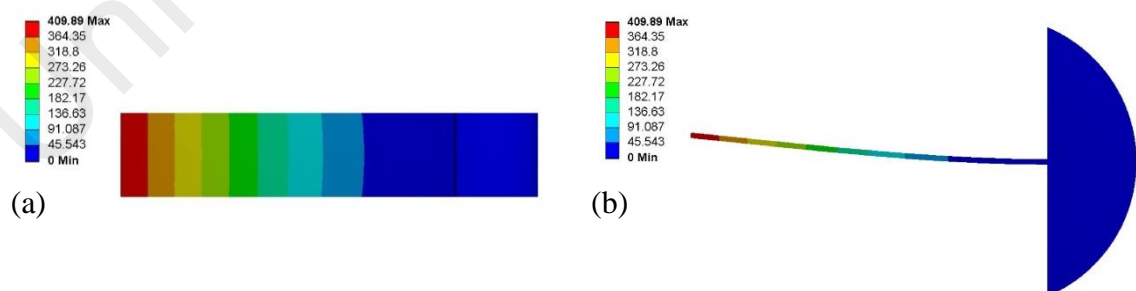


Figure 4.24: Modal Analysis of Coupled Semicircle Bluff Splitter Body and Elastic Plate Model (a) Top View (b) Side View

4.3.1.2 Vortex Formation Length of Different Bluff Splitter Body Shapes

In order to investigate the vortex formation length, fluctuating lift force and vortex induced vibration of a structural model with different bluff splitter body shapes, the

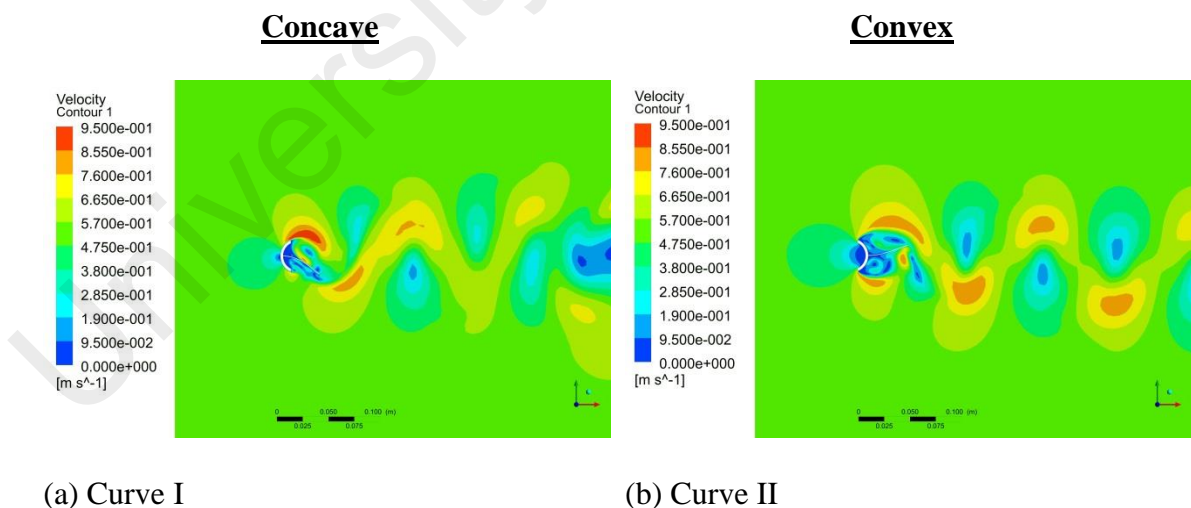
models are divided into three main categories according to the design of the shape, the first category is a Concave shape consists of Curve I, Diffuser I, Semi-Circle I, Trapezoidal I, and Triangle I, the second category is a Convex shape consists of Curve II, Diffuser II, Semi-Circle II, Trapezoidal II and Triangle II and the last is symmetrical category consists of two shapes which is circle and rectangular shape. Figure 4.25 shows that change in bluff splitter body shape causes slight difference in vortex formation pattern mainly between Concave and Convex shapes.

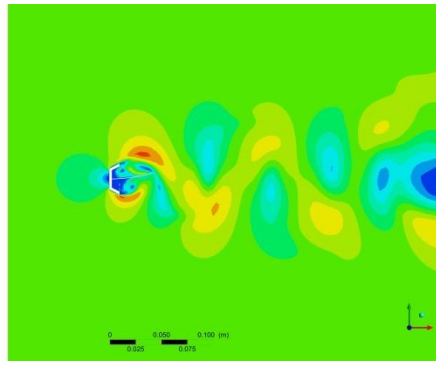
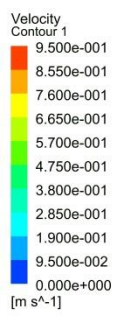
Illustrated in Figure 4.25 (a, c, e, g, and i) of shaped Curve I, Diffuser I, Semi-Circle I, Trapezoidal I, and Triangle I when flow first encounters concave bluff splitter body, it undergoes flow separation at the diverging leading edge but the flow travel along the edge of the bluff splitter body outwards. A secondary flow separation occurs at the straight trailing edge of bluff splitter body and evolves the flow into vortex. Hence, for a concave shape, the low velocity vortex region only occurs after the bluff splitter body surrounding the elastic plate. The vortex formation of a concave shape is thus mainly affected by trailing edge flow separation but less affected by leading edge.

Convex shapes of bluff splitter body of Curve II, Diffuser II, Semi-Circle II, Trapezoidal II and Triangle II in Figure 4.25 (b, d, f, g, and h) show that flow separation occurs at the leading edge of bluff splitter body, small amount of vortex is formed around the converging transitioning region downstream. These vortices are guided downstream and develop into the main vortex region that surrounds the elastic plate after undergoing a secondary flow separation at trailing edge. For a convex shape, vortex is affected by both the leading and trailing edge of bluff splitter body. However, if the converging area is too large due to small edge angle, i.e. Triangle II in Figure 4.25(j); the main vortex region accumulates by the side edges of the bluff splitter body instead of interacting with the elastic plate. As a result, addition of vortex from both

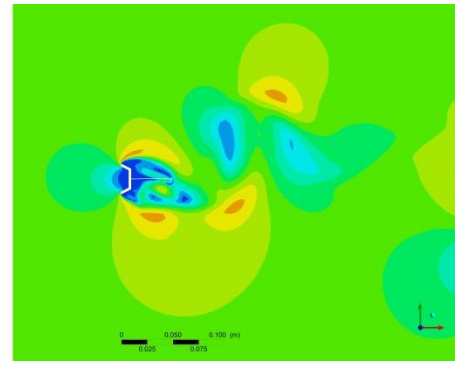
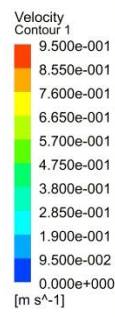
initial and secondary flow separation create irregular vortex propagation downstream which affect the resultant force and displacement.

Circular bluff splitter body is a combination of both concave and convex shapes. When flow encounters a circular bluff splitter body, it exhibits characteristic of both the shapes discussed above. The flow is observed to be separated at the leading edge and follows along the edge of the circle until it reaches the midpoint of the shape. A secondary flow separation occurs where part of the vortex is formed at the converging edge before the main vortex region surrounding the elastic plate. From Figure 4.25 (I), a rectangular shape exhibits a similar characteristic as a convex shape but because the edge of the bluff splitter body does not have an angular transitional region, a smaller region of vortex is formed at the side of the bluff splitter body. The main vortex region still occurs around the elastic plate after the flow undergoes a secondary flow separation. Unlike convex shape where it has a transitional inward angle, the flat edged rectangular shape has a comparably smaller vortex region as per discussed above.

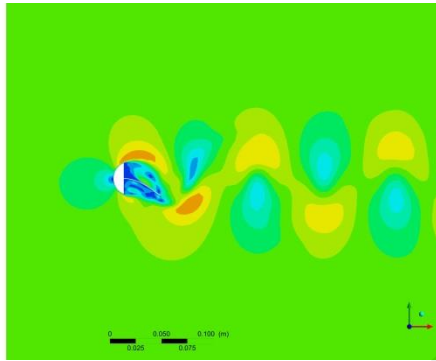
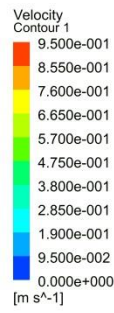




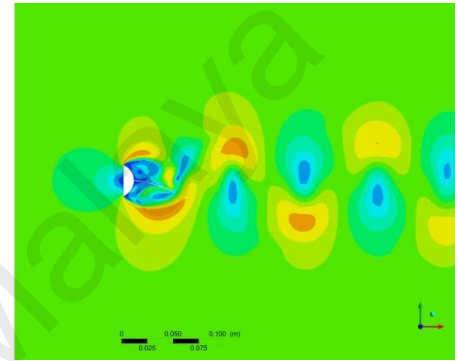
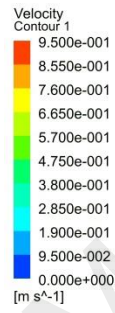
(c) Diffuser I



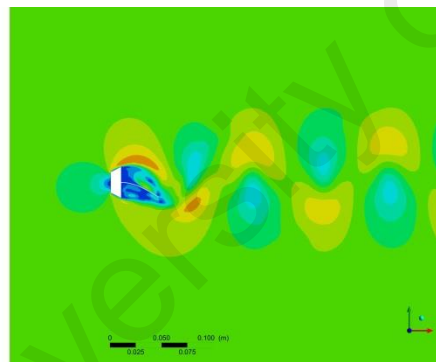
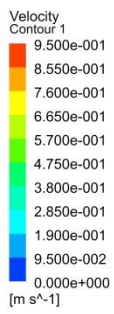
(d) Diffuser II



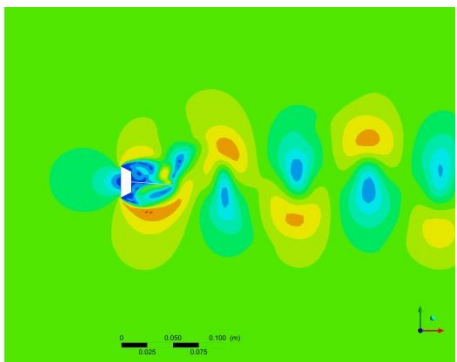
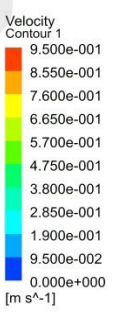
(e) Semi-Circle I



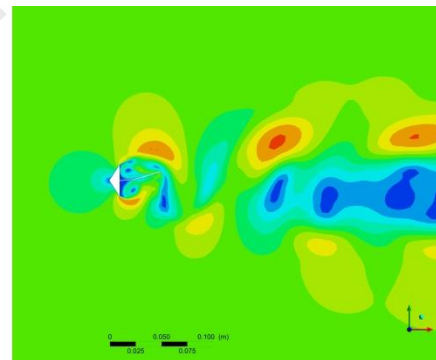
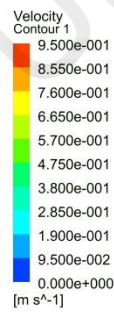
(f) Semi-Circle II



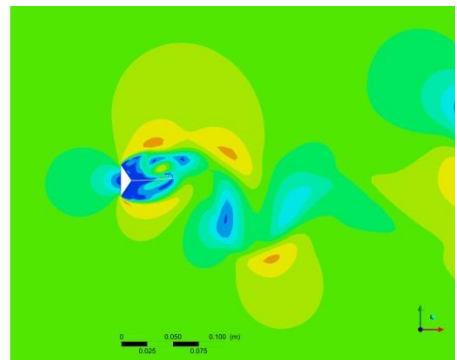
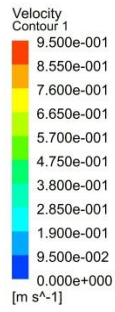
(g) Trapezoidal I



(h) Trapezoidal II



(i) Triangle I



(j) Triangle II

Symmetrical

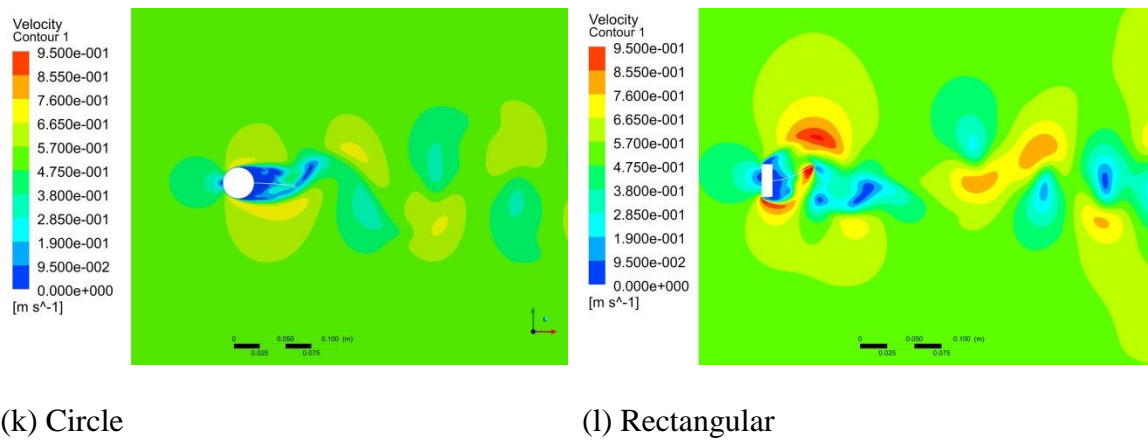


Figure 4.25: Velocity Contour of Different Cross Section of Bluff Splitter Body Shape

4.3.1.3 Fluctuating Lift Force of Different Bluff Splitter Body Shapes

In this section, it is shown in Figure 4.26 although having the same maximum width of 0.03m and undergoing the same wind speed of 0.513 m/s, due to different bluff splitter body shapes, the fluctuating lift force generated is different. Vortex formation after passing through the bluff splitter body as per mentioned in Section 4.3.1.2 has a heavy influence on the fluctuating lift force. The following results on different bluff splitter body shapes are compared with rectangular bluff splitter body shape used as a benchmark case.

Concave shapes of Curve I, Diffuser I, Semi-Circle I, and Triangle I generate higher lift force compared to rectangular bluff splitter body, registering 76.04%, 82.69%, 19.57% and 53.91% respectively. According to Section 4.3.1.2, vortex formed by a concave shape bluff splitter body is mainly contribute by the diverging trailing edge and vortex region mainly accumulates around the elastic plate. A larger low velocity vortex region covering entire downstream width of concave bluff splitter body develops higher fluctuating lift force or higher force applied normal to the elastic plate according to Bernoulli's principle relationship.

Convex shapes of Curve II, Trapezoidal II and Semicircle II have lower lift force generated compared to rectangular bluff splitter body, having difference -0.53%, -22.77%

and -18.09% respectively. Small vortex region that accumulates at the converging edge due to leading edge flow separation of a convex bluff splitter body is the main reason that weakens the fluctuating lift force of the vortex region surrounding the elastic plate. Partial flow undergoes vortex formation at converging edge, the main vortex region occurs around the elastic plate is then comparatively weaker. It is observed that Triangle II and Diffuser II convex bluff splitter body shapes tend to had a higher than usual RMS lift force value of $6.91E-05$ N and $7.41E-05$ N compared to the Rectangular bluff splitter body with difference of 55.571% and 58.569% respectively. According to Appendix C Figure C.5 (iv and x), the high fluctuating lift force in Triangle II was due to propagation of vortex accumulated at the large converging area acting onto the plate. Hence, the elastic plate first experienced lift force induced from flow separation vortex and then followed by the lift force from vortex propagation mentioned above, as the graph line with respect to time had an integration of two frequencies. Diffuser II on the other hand, is made out of a plate, thus when flow is obstructed and accumulated at the empty leading edge area shown in Figure 4.25, flow is affected by the sharp curve at the side edge of the leading edge area as this prevents fluid from flowing smoothly unlike Curve II which have smooth edges at the mentioned area. This flow has a different flow frequency thus creates an out-of phase vortex that disrupts the main vortex generated.

Circular shape that has the combination of both concave and convex side is observed to be not performing well in generating high fluctuating lift force. This is due to the shape promotes smooth fluid flow along the wall from leading and trailing edges of the shape and hence, reducing the vortex formation at the elastic plate and minimizing fluctuating lift force magnitude developed.

Solid shapes (i.e. Semicircle and Trapezoidal) and thin plate shapes (i.e. Curve and Diffuser) present some differences in the results generated. The thinner shape counterpart of curve and diffuser show a comparatively higher fluctuating lift force than

the solid shape counterpart. Curve I and Diffuser I thin bluff splitter body shapes allow part of the elastic plate to submerge in the hollow region of the trailing edge. Vortices fill the entire hollow region of the bluff splitter body shape as flow separation occurred. This induced a larger vortex area compared to a solid bluff splitter body, henceforth producing a larger value of fluctuating lift force in which increase by 28.33% and 53.83% respectively in comparison with Solid bluff splitter body shapes of Semicircle I and Trapezoidal 1.

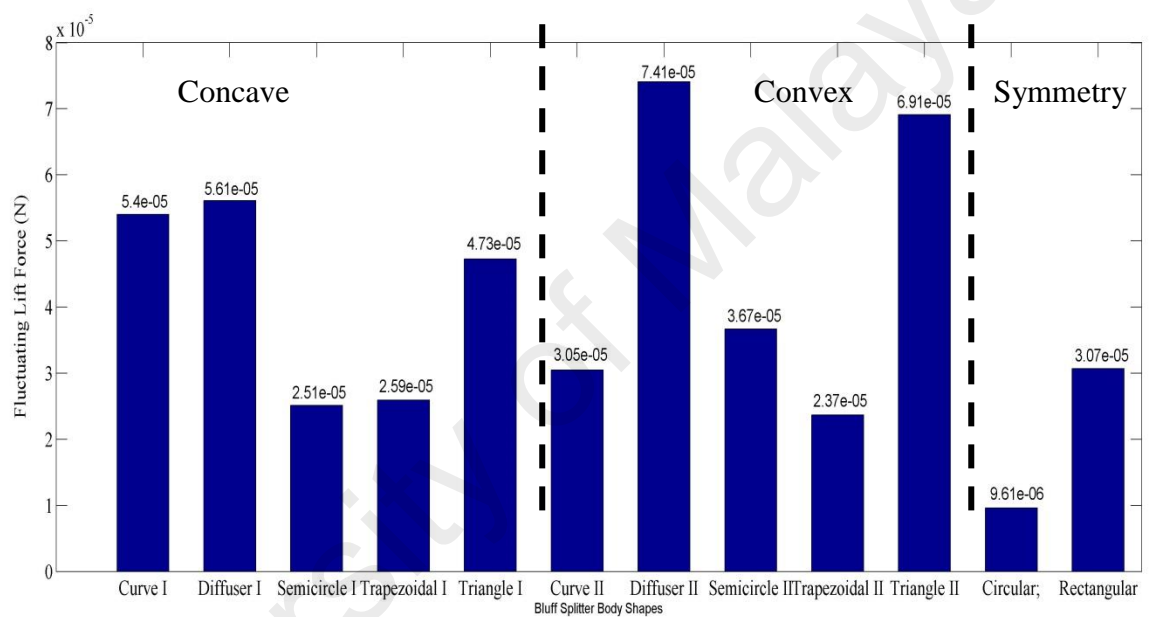


Figure 4.26: Graph of RMS Lift Force with Different Bluff Splitter Body Shape

4.3.1.4 Vortex Induced Vibration of Different Bluff Splitter Body Shapes

Different bluff splitter body shape also affects the resulting vortex frequency and VIV amplitude of the elastic plate. According to the context in previous sections, vortex frequency and fluctuating lift force generated are important in determining the resulting VIV performance.

From Table 4.8, concave shaped bluff splitter bodies i.e. Curve I, Diffuser I, Semi-Circle I, and Triangle I generate higher vortex frequency compared to other

shapes, ranging from 3.491 Hz to 3.571 Hz which is equivalent to 13.07% to 15.66% higher compared to a rectangular bluff splitter body. From the context above, fluid flow undergoes an initial flow separation when came across the leading edge of bluff splitter body and travels along the edge of the bluff splitter body before a secondary flow separation at the trailing edge forming the main vortex region surrounding the elastic plate. By focusing all vortex regions around the elastic plate without any accumulation on the bluff splitter body, larger pressure difference is induced during vortex occurrence. The diverging concave shape also acts as a diffuser to slightly accelerate the flow speed when passing through the bluff splitter body. With larger pressure difference and also slightly accelerated flow, resulting in higher vortex frequency as faster vortex interval acting by the side of the plate. By referring to Eq. 2.10, fluid flow velocity is proportional to the vortex frequency produced.

According to Figure 4.27, concave shapes have lower RMS tip displacement compared to a Rectangular bluff splitter body ranging from 1.17E-2 m to 1.41E-2 m with percentage difference of -23.04% to -7.33%. This is due to the vortex frequency produced by a concave shape is higher than the model's natural frequency and not coming near to the value. Lower RMS tip displacement value is induced despite having a higher fluctuating lift force shown in Appendix D Figure D 5.

Convex shaped bluff splitter bodies of Curve II, Trapezoidal II and Semicircle II on the other hand produced vortex frequency slightly lower than a rectangular bluff splitter body with values range from the lowest 2.797 Hz to the highest of 3.03 Hz which is -9.41% and -1.87% away from the natural frequency of the model. Trapezoidal II has the closest vortex frequency value compared to the model's natural frequency. The reason behind the reduction in vortex frequency is because convex bluff splitter body allows vortex formation to occur partially surrounding the bluff splitter body, slowing down the flow before reaching the elastic plate hence reducing the speed of the

main vortex formed around the elastic plate. Both Triangle II and Diffuser II creates a very high fluctuating lift force due to the geometrical shape generating additional vortex flow besides the main vortex from flow separation as explained in Section 4.3.1.3. The delayed propagation of wake from the accumulated region combined with the main vortex region has resulted in very low vortex frequency with value 0.833 Hz and 0.714 Hz or equivalent to 73.02% and 76.88% which are far away from the natural frequency of the model.

Observed in Figure 4.27, convex shapes of Curve II, Semicircle II and Trapezoidal II have the same or higher RMS tip displacement compared to Rectangular bluff splitter body shape. Although having a relatively smaller value of fluctuating lift force, vortex frequency produced by a convex shape was closer to the natural frequency compared to a concave shape. The RMS tip displacement values for convex shapes mentioned above ranged from 0.0152 m to 0.0154 m or 0 to 1.32% increment compared to Rectangular bluff splitter body with Trapezoidal II having the highest RMS tip displacement out of all the bluff splitter body shapes by a slight margin. This occurrence is related to the resonance phenomenon of structure, when the vortex frequency produced is close to the natural frequency of the structure, high vibrational amplitude is induced. Diffuser II and Triangle II have a very low vortex frequency value compared to the model's natural frequency stated in Table 4.8, resulting in a very low RMS tip displacement magnitude. These shapes have a RMS tip displacement value of 0.0119 m and 0.00114 m respectively or equivalent to -21.64% and -24.90% compared to the rectangular shape.

Circular and Rectangular Bluff Splitter Body representing symmetrical bluff splitter body shapes generate vortex frequency value of 3.334 Hz and 3.182 Hz which are in between vortex frequencies generated by Concave and Convex shapes. The symmetrical properties of both the shapes are the main reason vortex frequency values

are between the two main shape categories. A symmetrical Circular bluff splitter body, having lower fluctuating lift force and unmatched vortex frequency to the model's natural frequency value has a low resulting RMS tip displacement of 0.014 m or 25.33% lower than the RMS tip displacement of a rectangular bluff splitter body.

Table 4.8: Vortex Frequency Produced by Different Bluff Splitter Body Shape and Difference with Natural Frequency

Bluff Splitter Body Shape	Vortex Frequency (Hz)	Natural Frequency (Hz)	Difference (%)
<u>Concave Shape</u>			
Curve I	3.497	3.0876	13.26
Diffuser I	2.976		-3.61
Semicircle I	3.496		13.23
Trapezoidal I	0.714		-76.88
Triangle I	3.491		13.07
<u>Convex Shapes</u>			
Curve II	2.797		-9.41
Diffuser II	3.571		15.66
Semicircle II	3.03		-1.87
Trapezoidal II	3.571		15.66
Triangle II	0.833		-73.02
<u>Symmetrical Shapes</u>			
Cylinder	3.334		7.98
Square	3.182		3.06

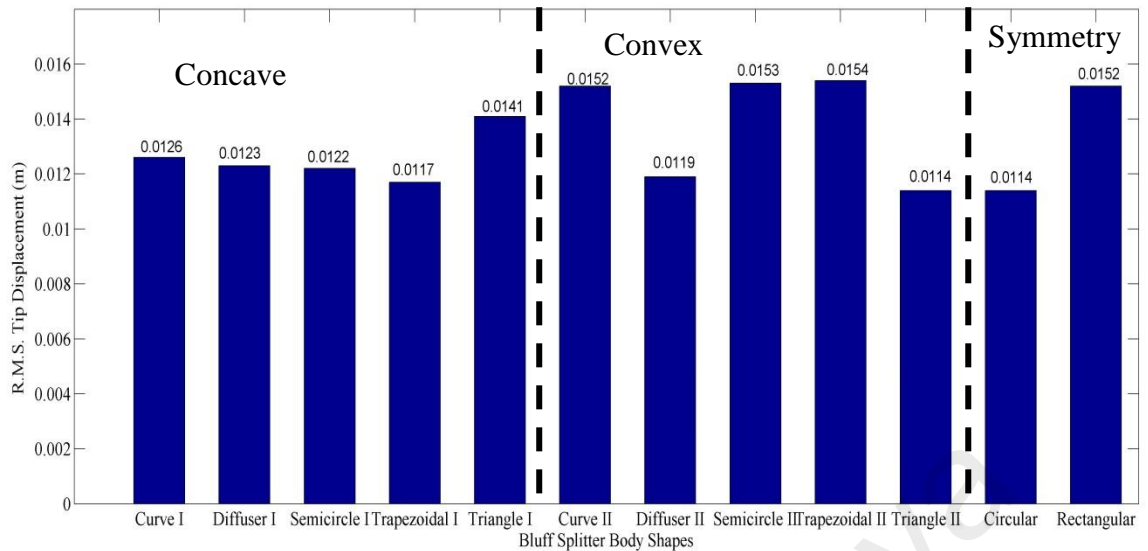


Figure 4.27: Graph of RMS Tip Mesh Displacement with Different Bluff Splitter Body Shape

4.3.2 Bluff Splitter Body Edge Angle Difference

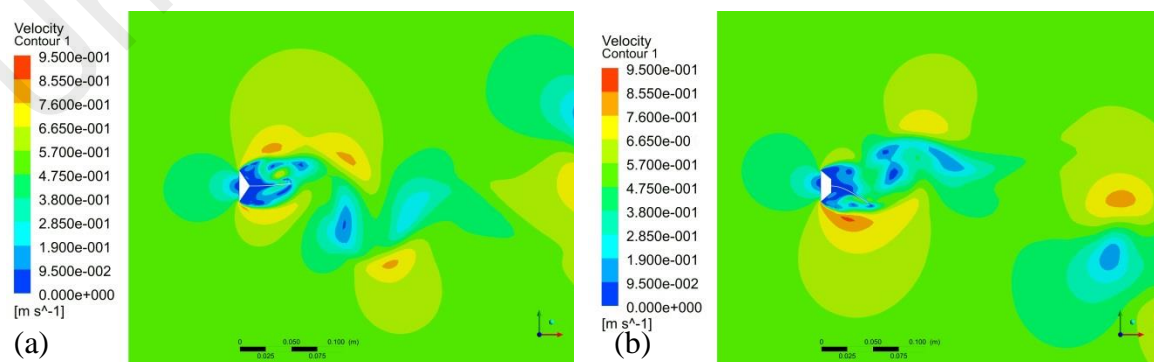
From previous section of 4.3.1, it is seen that concave and convex shape bluff splitter body heavily affects the resultant fluctuating lift force, vortex frequency and RMS tip displacement performance of a coupled bluff splitter body and elastic plate model. Since it is proven in the previous section that Trapezoidal II bluff splitter body has the highest RMS tip displacement performance, this section is focus on altering the edge angle of the bluff splitter body in order to improve the VIV performance. 7 different angles of 34.22° , 45° , 60° , 75° , 90° , 120° , and 146.31° have been tested in order to improve the performance through angle change.

4.3.2.1 Vortex Formation of Different Angle of Trapezoidal Bluff Splitter Body

Figure 4.28 presents the vortex formation with different edge angle of bluff splitter body with the same bluff splitter body width of 0.03 m under 0.513 m/s wind speed. Similar to Section 4.3.1, a bluff splitter body of different edge angle with 0.03 m width is sufficient to produce quality periodic vortex formation around the elastic plate. This is proven with periodic wave propagation downstream developed from upstream vortex region as shown in Figure 4.28 (a) - (g).

Bluff splitter body shapes with edge angle of 120° and 146.31° which resembles a concave shaped Trapezoidal I and Triangle I caused an outward flow separation, where the flow encounters initial flow separation at the leading edge of the bluff splitter body before travelling along the edge until it undergoes a secondary flow separation at the trailing edge of the bluff splitter body. The vortex region formed from these shapes only accumulates around the elastic plate after passing the bluff splitter body.

Bluff splitter body shapes with edge angle of 34.22° , 45° , 60° and 75° resemble a convex shaped triangle and trapezoid. After an initial flow separation at the straight leading edge, small vortex region is accumulated at the converging region of the convex bluff splitter body. A secondary flow separation occurred at the trailing edge forming vortex region that covers the elastic plate. Figure 4.28 (a) and (b) observes that 34.22° and 45° bluff splitter body shapes generate wake that is non periodic compared to 60° and 75° bluff splitter body mentioned above. It is mentioned in Section 4.3.1.2 that if the edge angle value is too small, vortex region accumulated at the converging area is very large. The large accumulated vortex region around the edge of the bluff splitter body is delayed, causing disruption in the main vortex region when propagating downstream thus the contour in Figure 4.28 (a) and (b) does not displayed a periodic interval of high and low velocity region.



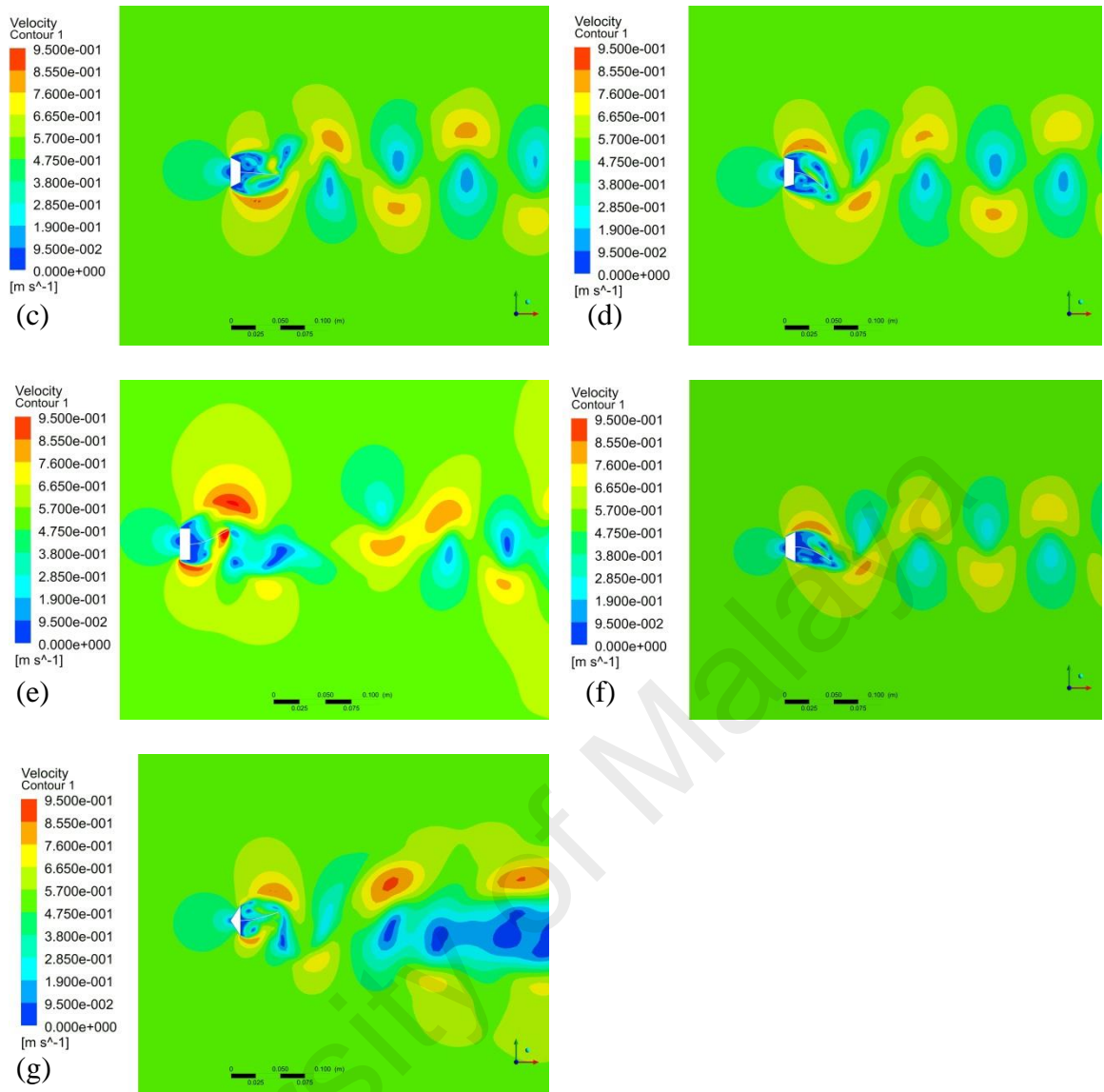


Figure 4.28: Vortex Formation with Different Angle Bluff Splitter Body of (a) 34.22°(b) 45° (c) 60° (d) 75° (e) 90° (f) 120° and (g) 146.31°

4.3.2.2 Fluctuating Lift Force of Different Angles of Trapezoidal Bluff Splitter

Body

Variance in edge to the base angle of a bluff splitter body generates different fluctuating lift force values. Edge angle of a bluff splitter body affects the fluid flow through flow separation and vortex formation. Bluff splitter bodies with edge angle increasing from 60° to 146.31° showed general increase in fluctuating lift force illustrated in Figure 4.29.

Concave shapes bluff splitter body of 120° and 146.31° edge angle have comparatively higher fluctuating lift force values of 3.69E-5 N and 4.73E-5 N or 20.19% and 54.07% away from the rectangular bluff splitter body value. Vortex formed by a

concave shape bluff splitter body is mainly contributed by the trailing edge and vortex region mainly accumulates around the bluff splitter body. A larger low velocity vortex region covering entire downstream width of concave bluff splitter body develops higher fluctuating lift force or force applied normal to the elastic plate

Edge angles of 60° and 75° which resembled a convex shape have the lowest fluctuating lift force compared to all other angles with values of $2.69\text{E-}5$ N and $2.37\text{E-}5$ N or 12.377% and 22.80% away from rectangular bluff splitter body value. Small vortex region that accumulates at the converging edge due to leading edge flow separation of a convex bluff splitter body is the main reason that weakened the fluctuating lift force of the vortex region surrounding the elastic plate. Due to partial flow energy has been consumed during vortex formation at converging edge, the main vortex region occurred around the elastic plate post trailing edge flow shedding is comparatively weaker.

Convex bluff splitter bodies with edge angle of 34.22° and 45° have extremely large vortex region accumulated around the converging edges instead of the elastic plate. The large accumulated vortex region propagates downstream adding on to the main vortex region surrounding the elastic plate to act as a secondary force that increases the overall fluctuating lift force value acting on the elastic plate. These 2 edge angle bluff splitter bodies induce fluctuating lift force of $6.91\text{E-}5$ N and $10.4\text{E-}5$ N which is 125.08% and 238.76% higher than 90° rectangular bluff splitter body.

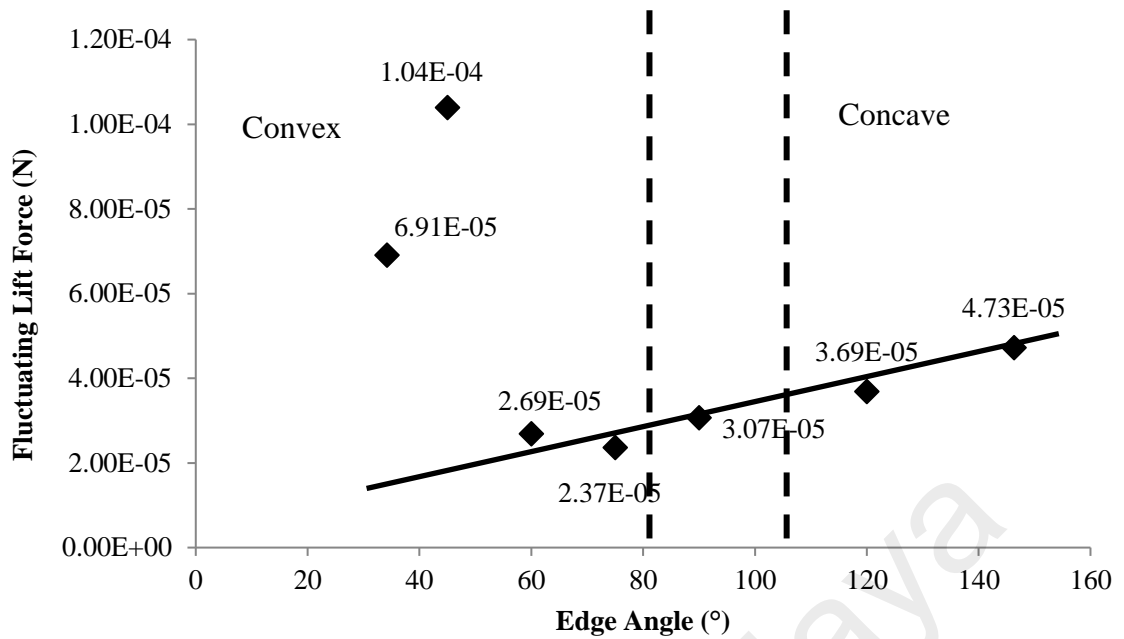


Figure 4.29: Graph of RMS Lift Force against Angle of Trapezoidal Bluff Splitter Body

4.3.2.3 Vortex Induced Vibration of Different Edge Angles of Bluff Splitter Body

Vortex frequency of different edge angle bluff splitter bodies are shown in Table 4.9. From the table, it is shown that vortex frequency produced by bluff splitter body increases with the increase of the edge angle.

Bluff splitter bodies with edge angle of 120° and 146.31° resemble a concave shaped bluff body of Trapezoidal I and Triangle I produce relatively higher vortex frequency with similar values of 3.571 Hz which is 15.671% higher if compared to a natural frequency of structural model. Domination of trailing edge vortex shedding focuses the vortex region mainly around the elastic plate without any accumulation by the side of the bluff splitter body and thus increasing pressure difference caused by vortex acting on the elastic plate. Diverging edge of concave bodies also act as a diffuser guide and accelerator when flow passes through it. Due to these reasons, vortex frequency generated is slightly higher. These 2 angle bluff splitter bodies do not have a high RMS tip displacement values, i.e. 0.0117 m and 0.0141 m which yield a difference

of 23.03% and 7.24% respectively compared to the rectangular bluff splitter body. Larger edge angle bluff splitter body produce a lower RMS tip displacement is due to the vortex frequency generated is far away from the natural frequency of the model. By not resonating with the model's natural frequency, high vibrational amplitude is unachievable. However, bluff splitter body with edge angle 146.31° has a fluctuating lift force of 21.99 % higher compared to 120° edge angle creating comparably higher RMS tip displacement despite having the same vortex frequency value.

Bluff splitter bodies with 60° and 75° edge angle resembling a convex shape have a similar vortex frequency value of 3.03 Hz with -1.853% difference compared to the natural frequency of the structure. Vortex region that is partially accumulated at the converging edge after leading edge flow shedding reduces the vortex area that excites the elastic plate and hence reduces the vortex frequency. Higher value of RMS tip displacement of 0.0159 m and 0.0154 m is achieved which is equivalent to 4.61% and 1.31% higher than a rectangular bluff splitter body. Edge angle 60° has the highest RMS tip displacement value out of all edge angle with 0.0159 m as the fluctuating lift force produced is slightly higher. Convex shape bluff splitter body is able to achieve higher value of RMS tip displacement mainly due to closeness of vortex frequency to the natural frequency of the model albeit having the lowest fluctuating lift force. This again proves that having a vortex frequency that is near to the natural frequency is the top priority in generating high displacement in VIV. Besides, the converging edge also acts as a guide for the flow to act onto the surface of the elastic plate.

Small angles bluff splitter body of 34.22° and 45° have very low vortex frequencies. The low vortex frequency is contributed by the accumulation of vortex region mainly around the bluff splitter body instead of the elastic plate. As wake propagates downstream, it creates a combination of accumulated vortex with the main vortex formation around elastic plate. But as the wake propagates downstream is

delayed, it results in low vortex frequency yielding 74.28% and 72.31% away from rectangular bluff splitter body. As seen in Figure 4.30, these bluff splitter bodies own lower RMS tip displacement with values 0.0114 m and 0.0125 m. They are 25% and 17.76% in difference compared to the rectangular bluff splitter body. The reason behind the drop in values is because of the vortex frequency produced is far away from the natural frequency of the model although the fluctuating lift force generated is the highest among all other edge angle of the bluff splitter bodies. The tip displacement chart can be viewed in Appendix D Figure D 6 (i) and (ii).

Table 4.9: Vortex Frequency with Different Bluff Splitter Body Angle and the Difference with Natural Frequency.

Angle of Bluff Splitter Body	Vortex Frequency (Hz)	Natural Frequency (Hz)	Difference (%)	
<u>Convex</u>				
34.22°	0.794	3.087	-74.28	
45°	0.855		-72.31	
60°	3.03		-1.87	
75°	3.03		-1.87	
<u>Symmetry</u>				
90°	3.182	3.087	3.06	
<u>Concave</u>				
120°	3.571		15.66	
146.31°	3.571		15.66	

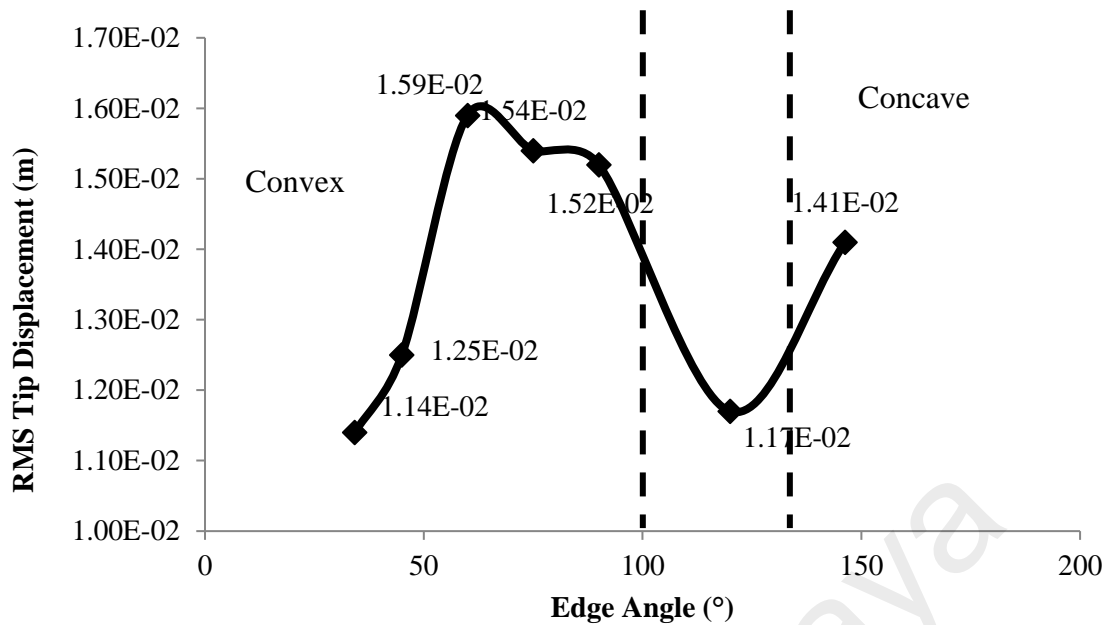


Figure 4.30: Graph of RMS Tip Displacement against Different Angle of Trapezoidal Bluff Splitter Body

4.3.3 Summary (Bluff Splitter Body Design)

From Section 4.3.1, it is summarized that a convex bluff splitter body especially trapezoidal bluff splitter body has the best performing VIV amplitude. This is due to convex shapes having a converging region that allows flow to be accumulated and guided onto the elastic plate. This region slightly lowers the vortex frequency generated, hence produces vortex frequency that is closer to the natural frequency of the model. It is shown in Section 4.3.2 that the best performing bluff splitter body shape is a convex trapezoidal shape with 75° edge angle. In Section 4.3.2, changing the edge angle from 75° to 60° the convex shape bluff splitter body experiences the same flow separation process but produces a higher fluctuating lift force and hence is able to produce a better VIV performance.

CHAPTER 5: CONCLUSION

5.1 Conclusion

In conclusion, all the objectives listed in this research have been achieved with decent results. With simulation of coupled bluff splitter body and cantilever plate models validated with respective cases, the conclusion obtained for each objective is showcased below.

It is determined that with constant fluid flow, low and high wind speed does not affect the vortex formation length and the pattern of vortex, but it will change the lift force and vortex frequency acting on the model. With the PVEH plate model, wind speed of 19 m/s yields vortex frequency of 75.758 Hz near to the natural frequency of the model, hence produce the highest RMS tip displacement of 1.26 mm with a 49.76% increment compared to the 20m/s non-resonant cases. As the elasticity of the elastic plate is very high compare to PVEH plate, the closeness of the vortex frequency to the natural frequency of the model is not the only factor that affects the resultant VIV performance. In this section, 0.7 m/s has a better performance with 0.00912 m RMS tip displacement although 3.94 Hz vortex frequency is slightly away from the model's natural frequency. But, 0.513 m/s wind speed with 0.00753 m RMS tip displacement yields vortex frequency 3.03 Hz which is the nearest to the model's natural frequency. This research section deduces that the model's vibrational frequency tends to always lock-in to the vortex frequency produced by flow separation. In order to maximize vibrational amplitude, the lock-in vibrational frequency must be near to the natural frequency of the model to undergo resonance and a higher lift force value will improved the effect of VIV on more elastic models.

In the section of bluff splitter body width variation, only with the presence of a larger bluff splitter body of $D/L > 0.125$, visible and better quality vortex is generated.

Change of aspect ratio is proved to be affecting vortex formation length, vortex frequency and the fluctuating lift force amplitude. In both sections of bluff splitter body width and elastic plate length variations, larger aspect ratio of $D/L \geq 1$ produces much lower frequency than the natural frequency due to vortex formation length exceeding the elastic plate length causing vortex disruptions from either side of the plate. On the other hand, smaller aspect ratio of $D/L < 1$ produces vortex frequency nearer to the natural frequency of the model used. In the section of bluff splitter body width variation, a larger bluff splitter body width is shown to produce higher lift force. 0.03 m bluff splitter body having relatively higher lift force and a closer vortex frequency to the natural frequency of the model with the best VIV performance of 0.0153 m comparably. In the elastic plate length variation section, 0.04 m elastic plate length having the closeness of vortex frequency to the natural frequency of the model is the best performing model with RMS tip displacement of 0.0152 m and the highest displacement to length ratio of 0.38. Both of these scenario shows that model of aspect ratio value of 0.75 is able to perform at the best level.

In the final section of bluff splitter body shape variation in VIV enhancement, it is concluded that a convex shaped bluff splitter body has a better performance compared to other shapes with Trapezoidal shape of 60° having the best performance with 0.0159 m RMS tip displacement. A convex shape ensures vortex frequency 3.03 Hz is closer to the model's natural frequency compared to rectangular with a lower value of lift force. A concave shape guiding the flow outwards have larger lifts force and also a higher vortex frequency. Bluff splitter body of edge angle 34.22° and 45° and Diffuser II is observed to have a very low vortex frequency value because disruption of flow occurred due to shape geometry, hence lowering the RMS tip displacement value.

In a nutshell, a Trapezoidal Bluff Splitter Body shape with 60° angle, Bluff Splitter Body width of 0.03m and Elastic Plate length of 0.04m generates RMS tip

displacement value of 0.0159 m is the highest performing structural model conducted in this research. Compared to the original research model done by Dettmer, this improved version of coupled bluff splitter body and elastic plate model had a RMS tip displacement value increased by a margin of 111.16 %.

In future works, with the results obtained from the current investigation, an omni-directional wind collector with wind speed control can be designed and installed in front of the coupled bluff splitter body and PVEH plate to fulfill the task of energy harvesting. The omni-directional wind collector is able direct winds in single direction to the wind speed controller which either enhances or reduces the wind speed to an optimum range to before channeling it to the adopted optimum aspect ratio, shape and angle design of coupled bluff splitter body and PVEH plate. By generating optimum vortex frequency according to the characteristics of the PVEH plate, maximum energy output is expected.

5.2 Future Recommendations

In future, more efforts in reducing the overall structure's natural frequency could be focused to lower the wind speed required to achieve the resonant frequency, henceforth improving the performance when installed in conventional exhaust air cooling tower that generates lower exhaust air velocity. A prototype could also be fabricated to conduct wind tunnel and on site tests in the future to further justify the practicality of the VIV harvesters in real life application. Beside, an array of modules could be looked into when different orientation and arrangement of models are able to improve the average power generated.

REFERENCES

- Agency, I. E. (2014). *Key World Energy Statistics 2014* (2014 ed.). Paris: Chirat.
- Akaydin, H. D., Elvin, N., & Andreopoulos, Y. (2010). Energy Harvesting from Highly Unsteady Fluid Flows using Piezoelectric Materials. *Journal of Intelligent Material Systems and Structures*, 21(13), 1263-1278.
- Akaydin, H. D., Elvin, N., & Andreopoulos, Y. (2012). The performance of a self-excited fluidic energy harvester. *Smart Materials & Structures*, 21(2).
- Akilli, H., Sahin, B., & Tumen, N. F. (2005). Suppression of vortex shedding of circular cylinder in shallow water by a splitter plate. *Flow Measurement and Instrumentation*, 16(4), 211-219.
- Apelt, C., & West, G. (1975). The effects of wake splitter plates on bluff-body flow in the range $10^4 < R < 5 \times 10^4$. Part 2. *Journal of Fluid Mechanics*, 71(01), 145-160.
- Ashwin Vinod, A. K., Arindam Banerjee, Jonathan Kimball, . (2013). *Augmenting Energy Extraction From Vortex Induced Vibration Using Strips Of Roughness/Thickness Combinations*. Paper presented at the Proceedings of the 1st Marine Energy Technology Symposium, Washington, D.C.
- Bao, Y., Zhou, D., & Tu, J. (2011). Flow interference between a stationary cylinder and an elastically mounted cylinder arranged in proximity. *Journal of Fluids and Structures*, 27(8), 1425-1446.
- Barrero-Gil, A., Pindado, S., & Avila, S. (2012). Extracting energy from Vortex-Induced Vibrations: A parametric study. *Applied Mathematical Modelling*, 36(7), 3147-3154.
- Bearman, P. (1965). Investigation of the flow behind a two-dimensional model with a blunt trailing edge and fitted with splitter plates. *Journal of Fluid Mechanics*, 21(02), 241-255.
- Bearman, P. W. (1984). Vortex Shedding from Oscillating Bluff-Bodies. *Annual Review of Fluid Mechanics*, 16, 195-222.
- Benra, F. K., Dohmen, H. J., Pei, J., Schuster, S., & Wan, B. (2011). A Comparison of One-Way and Two-Way Coupling Methods for Numerical Analysis of Fluid-Structure Interactions. *Journal of Applied Mathematics*, 2011, 16.

- Bernitsas, M. M., Raghavan, K., Ben-Simon, Y., & Garcia, E. M. H. (2006). VIVACE (Vortex induced vibration aquatic clean energy): A New Concept in Generation of Clean and Renewable Energy from Fluid Flow. *Proceedings of the 25th International Conference on Offshore Mechanics and Arctic Engineering, Vol 2*, 619-637.
- Billah, K. Y., & Scanlan, R. H. (1991). Resonance, Tacoma Narrows Bridge Failure, and Undergraduate Physics Textbooks. *American Journal of Physics*, 59(2), 118-124.
- Breinlinger, F., Kunz, C., Loche, K., Niemann, H. J., Novak, B., Ruckebrod, C., & Schwind, W. (2011). Eurocode 1-Actions on Structures. *Bauingenieur*, 86, 315-326.
- Brika, D., & Laneville, A. (1993). Vortex-Induced Vibrations of a Long Flexible Circular-Cylinder. *Journal of Fluid Mechanics*, 250, 481-508.
- Brika, D., & Laneville, A. (1999). The flow interaction between a stationary cylinder and a downstream flexible cylinder. *Journal of Fluids and Structures*, 13(5), 579-606.
- Cable, M. (2009). *An evaluation of turbulence models for the numerical study of forced and natural convective flow in Atria*. (Master of Science (Engineering)), Queen's University, Ontario.
- Cengel, Y., & Cimbala, J. (2013). *Fluid Mechanics Fundamentals and Applications: Third Edition* (3 ed.). New York: McGraw-Hill Higher Education.
- Chung, M. H. (2016). Transverse vortex-induced vibration of spring-supported circular cylinder translating near a plane wall. *European Journal of Mechanics B-Fluids*, 55, 88-103.
- Cimbala, J. M., & Garg, S. (1991). Flow in the Wake of a Freely Rotatable Cylinder with Splitter Plate. *Aiaa Journal*, 29(6), 1001-1003.
- De Nayer, G., Kalmbach, A., Breuer, M., Sicklinger, S., & Wüchner, R. (2014). Flow past a cylinder with a flexible splitter plate: A complementary experimental–numerical investigation and a new FSI test case (FSI-PfS-1a). *Computers & Fluids*, 99, 18-43.
- Demori, M., Ferrari, M., Ferrari, V., Farisè, S., & Poesio, P. (2014). Energy Harvesting from Von Karman Vortices in Airflow for Autonomous Sensors. *Procedia Engineering*, 87, 775-778.

- Dettmer, W., & Peric, D. (2006). A computational framework for fluid-structure interaction: Finite element formulation and applications. *Computer Methods in Applied Mechanics and Engineering*, 195(41-43), 5754-5779.
- Ding, L., Zhang, L., Wu, C. M., Mao, X. R., & Jiang, D. Y. (2015). Flow induced motion and energy harvesting of bluff bodies with different cross sections. *Energy Conversion and Management*, 91, 416-426.
- Donea, J., Giuliani, S., & Halleux, J.-P. (1982). An arbitrary Lagrangian-Eulerian finite element method for transient dynamic fluid-structure interactions. *Computer Methods in Applied Mechanics and Engineering*, 33(1-3), 689-723.
- Durst, F. (2008). *Fluid Mechanics: An Introduction to the Theory of Fluid Flows*. Berlin: Springer Berlin Heidelberg.
- Energy Academy, H.-W. (2014). *BP Statistical Review of World Energy 2014*.
- Energy Commission. (2014). *Energy Malaysia: Towards A World Class Energy Sector*.
- Étienne, S., & Pelletier, D. (2012). The low Reynolds number limit of vortex-induced vibrations. *Journal of Fluids and Structures*, 31, 18-29.
- Feng, C. C. (1968). *The Measurement of Vortex Induced Effects in Flow Past Stationary and Oscillating Circular and D-section Cylinders*. (Master of Applied Science), University of British Columbia, Vancouver. Retrieved from <https://books.google.com.my/books?id=jvz2SAAACAAJ>
- Ferziger, J. H., & Peric, M. (2012). *Computational Methods for Fluid Dynamics*: Springer Berlin Heidelberg.
- Giosan, I., & Eng, P. (2013). Vortex shedding induced loads on free standing structures. *Structural Vortex Shedding Response Estimation Methodology and Finite Element Simulation*, 42.
- Goushcha, O., Akaydin, H. D., Elvin, N., & Andreopoulos, Y. (2015). Energy harvesting prospects in turbulent boundary layers by using piezoelectric transduction. *Journal of Fluids and Structures*, 54, 823-847.
- Griebel, M., Dornseifer, T., & Neunhoffer, T. (1997). *Numerical Simulation in Fluid Dynamics: A Practical Introduction*: Society for Industrial and Applied Mathematics (SIAM, 3600 Market Street, Floor 6, Philadelphia, PA 19104).

- Griffin, O. M. (1995). A Note on Bluff-Body Vortex Formation. *Journal of Fluid Mechanics*, 284, 217-224.
- Grouthier, C., Michelin, S., Bourguet, R., Modarres-Sadeghi, Y., & de Langre, E. (2014). On the efficiency of energy harvesting using vortex-induced vibrations of cables. *Journal of Fluids and Structures*, 49, 427-440.
- Gu, F., Wang, J. S., Qiao, X. Q., & Huang, Z. (2012). Pressure distribution, fluctuating forces and vortex shedding behavior of circular cylinder with rotatable splitter plates. *Journal of Fluids and Structures*, 28, 263-278.
- Gulvanessian, H. (2001). EN1991 Eurocode 1: Actions on structures. *Proceedings of the Institution of Civil Engineers-Civil Engineering*, 144, 14-22.
- Han, Z. L., Zhou, D., He, T., Tu, J. H., Li, C. X., Kwok, K. C. S., & Fang, C. Q. (2015). Flow-induced vibrations of four circular cylinders with square arrangement at low Reynolds numbers. *Ocean Engineering*, 96, 21-33.
- Hehn, T., & Manoli, Y. (2014). *CMOS Circuits for Piezoelectric Energy Harvesters: Efficient Power Extraction, Interface Modeling and Loss Analysis*: Springer Netherlands.
- Hiejima, S., & Nomura, T. (1999). Numerical study of the effect of periodic velocity excitation on aerodynamic characteristics of an oscillating circular cylinder. *International Journal of Computational Fluid Dynamics*, 12(3-4), 269-278.
- Ho-Le, K. (1988). Finite element mesh generation methods: a review and classification. *Computer-aided design*, 20(1), 27-38.
- Hobbs, W. B., & Hu, D. L. (2012). Tree-inspired piezoelectric energy harvesting. *Journal of Fluids and Structures*, 28, 103-114.
- Huang, Y. H. (2013). Electromechanical coupling efficiency of transverse vibration in piezoelectric plates according to electrode configuration. *Journal of the Chinese Institute of Engineers*, 36(7), 842-855.
- Huang, Y. H., & Ma, C. C. (2009). Experimental and Numerical Investigations of Vibration Characteristics for Parallel-Type and Series-Type Triple-Layered Piezoceramic Bimorphs. *Ieee Transactions on Ultrasonics Ferroelectrics and Frequency Control*, 56(12), 2598-2611.
- Huang, Y. H., Ma, C. C., & Li, Z. Z. (2014). Investigations on vibration characteristics of two-layered piezoceramic disks. *International Journal of Solids and Structures*, 51(1), 227-251.

- Huera-Huarte, F. J. (2014). On splitter plate coverage for suppression of vortex-induced vibrations of flexible cylinders. *Applied Ocean Research*, 48, 244-249.
- Irwanto, M., Gomesh, N., Mamat, M. R., & Yusoff, Y. M. (2014). Assessment of wind power generation potential in Perlis, Malaysia. *Renewable and Sustainable Energy Reviews*, 38(0), 296-308.
- Ji, C., Xiao, Z., Wang, Y., & Wang, H. (2011). Numerical investigation on vortex-induced vibration of an elastically mounted circular cylinder at low Reynolds number using the fictitious domain method. *International Journal of Computational Fluid Dynamics*, 25(4), 207-221.
- Kärnä, T. (2009). Damping methods to mitigate wind induced vibrations. *Journal of Structural Mechanics*, 42(1), 38-47.
- Khalak, A., & Williamson, C. H. K. (1999). Motions, forces and mode transitions in vortex-induced vibrations at low mass-damping. *Journal of Fluids and Structures*, 13(7-8), 813-851.
- Kinaci, O. K., Lakka, S., Sun, H., & Bernitsas, M. M. (2016). Effect of tip-flow on vortex induced vibration of circular cylinders for $Re = 1.2 \cdot 10^5$. *Ocean Engineering*, 117, 130-142.
- Kondo, N. (2014). Three-dimensional computation for flow-induced vibrations of an upstream circular cylinder in two tandem circular cylinders. *International Journal of Computational Fluid Dynamics*, 28(6-10), 461-476.
- Krushynska, A., Meleshko, V., Ma, C. C., & Huang, Y. H. (2011). Mode Excitation Efficiency for Contour Vibrations of Piezoelectric Resonators. *Ieee Transactions on Ultrasonics Ferroelectrics and Frequency Control*, 58(10), 2222-2238.
- Kuhl, J. M., & DesJardin, P. E. (2012). Power production locality of bluff body flutter mills using fully coupled 2D direct numerical simulation. *Journal of Fluids and Structures*, 28, 456-472.
- Kundu, P. K. (1990). *Fluid Mechanics*. San Diego: Academic Press.
- Launder, B., Reece, G. J., & Rodi, W. (1975). Progress in the development of a Reynolds-stress turbulence closure. *Journal of Fluid Mechanics*, 68(03), 537-566.
- M.R.S Siti, M. N., M. Syafrudin (2011). The Evaluation of Wind Energy Potential in Peninsular Malaysia. *International Journal of Chemical and Environmental Engineering*, 2(4), 284-290.

- Ma, C. C., Lin, Y. C., Huang, Y. H., & Lin, H. Y. (2007). Experimental measurement and numerical analysis on resonant characteristics of cantilever plates for piezoceramic bimorphs. *Ieee Transactions on Ultrasonics Ferroelectrics and Frequency Control*, 54(2), 227-239.
- McCarthy, J. M., Watkins, S., Deivasigamani, A., John, S. J., & Coman, F. (2015). An investigation of fluttering piezoelectric energy harvesters in off-axis and turbulent flows. *Journal of Wind Engineering and Industrial Aerodynamics*, 136, 101-113.
- Meliga, P., Chomaz, J. M., & Gallaire, F. (2011). Extracting energy from a flow: An asymptotic approach using vortex-induced vibrations and feedback control. *Journal of Fluids and Structures*, 27(5-6), 861-874.
- Menter, F. R. (1994). Two-equation eddy-viscosity turbulence models for engineering applications. *Aiaa Journal*, 32(8), 1598-1605.
- Moin, P., & Mahesh, K. (1998). Direct Numerical Simulation: A Tool in Turbulence Research. *Annual Review of Fluid Mechanics*, 30(1), 539-578.
- Munson, B. R., Young, D. F., & Okiishi, T. T. H. (2002). *Fundamentals of fluid mechanics*: John Wiley & Sons Australia, Limited.
- Nishi, Y. (2013). Power extraction from vortex-induced vibration of dual mass system. *Journal of Sound and Vibration*, 332(1), 199-212.
- Nishi, Y., Ueno, Y., Nishio, M., Quadrante, L. A. R., & Kokubun, K. (2014). Power extraction using flow-induced vibration of a circular cylinder placed near another fixed cylinder. *Journal of Sound and Vibration*, 333(10), 2863-2880.
- Oh, T. H., Pang, S. Y., & Chua, S. C. (2010). Energy policy and alternative energy in Malaysia: Issues and challenges for sustainable growth. *Renewable & Sustainable Energy Reviews*, 14(4), 1241-1252.
- Pang, J. H., Zong, Z., Zou, L., & Wang, Z. (2016). Numerical simulation of the flow around two side-by-side circular cylinders by IVCBC vortex method. *Ocean Engineering*, 119, 86-100.
- Parkinson, G. (1989). Phenomena and modelling of flow-induced vibrations of bluff bodies. *Progress in Aerospace Sciences*, 26(2), 169-224.
- Prasanth, T., & Mittal, S. (2008). Free v/s forced vibrations of a cylinder at low Re. *International Journal of Computational Fluid Dynamics*, 22(8), 583-592.

- Raghavan, K., & Bernitsas, M. M. (2011). Experimental investigation of Reynolds number effect on vortex induced vibration of rigid circular cylinder on elastic supports. *Ocean Engineering*, 38(5-6), 719-731.
- Rahman, M. A. A., Leggoe, J., Thiagarajan, K., Mohd, M. H., & Paik, J. K. (2016). Numerical simulations of vortex-induced vibrations on vertical cylindrical structure with different aspect ratios. *Ships and Offshore Structures*, 11(4), 405-423.
- REN21 (Producer). (2014). Renewable Energy Global Status Report 2014.
- Sarpkaya, T. (1979). Vortex-induced oscillations: a selective review. *Journal of applied mechanics*, 46(2), 241-258.
- Sarpkaya, T. (1997). Dynamics of a hydroelastic cylinder with very low mass and damping - Discussion. *Journal of Fluids and Structures*, 11(5), 549-551.
- Schmucker, H., Flemming, F., & Coulson, S. (2010). *Two-way coupled fluid structure interaction simulation of a propeller turbine*. Paper presented at the IOP Conference Series: Earth and Environmental Science.
- Sohankar, A. (2014). A LES study of the flow interference between tandem square cylinder pairs. *Theoretical and Computational Fluid Dynamics*, 28(5), 531-548.
- Tominaga, Y., Mochida, A., Yoshie, R., Kataoka, H., Nozu, T., Yoshikawa, M., & Shirasawa, T. (2008). AIJ guidelines for practical applications of CFD to pedestrian wind environment around buildings. *Journal of Wind Engineering and Industrial Aerodynamics*, 96(10-11), 1749-1761.
- Tropea, C., Jakirlic, S., Heinemann, H. J., Henke, R., & Hönliger, H. (2007). *New Results in Numerical and Experimental Fluid Mechanics VI: Contributions to the 15th STAB/DGLR Symposium Darmstadt, Germany 2006*: Springer Berlin Heidelberg.
- Versteeg, H. K., & Malalasekera, W. (2007). *An Introduction to Computational Fluid Dynamics: The Finite Volume Method*. London: Pearson Education Limited.
- Weickert, M., Teike, G., Schmidt, O., & Sommerfeld, M. (2010). Investigation of the LES WALE turbulence model within the lattice Boltzmann framework. *Computers & Mathematics with Applications*, 59(7), 2200-2214.
- Wen, Q., Schulze, R., Billep, D., Otto, T., & Gessner, T. (2014a). Modeling and Optimization of a Vortex Induced Vibration Fluid Kinetic Energy Harvester. *Procedia Engineering*, 87, 779-782.

- Wen, Q., Schulze, R., Billep, D., Otto, T., & Gessner, T. (2014b). Modeling and Optimization of a Vortex Induced Vibration Fluid Kinetic Energy Harvester. *Procedia Engineering*, 87(0), 779-782.
- Wendt, J. (2008). *Computational Fluid Dynamics: An Introduction*: Springer Berlin Heidelberg.
- Wilcox, D. C. (1988). Reassessment of the scale-determining equation for advanced turbulence models. *Aiaa Journal*, 26(11), 1299-1310.
- Wilcox, D. C. (2004). *Turbulence Modeling for CFD* (2 ed.). California: DCW Industries.
- Wyatt, T. A. (1992). Bridge Aerodynamics 50 Years after Tacoma Narrows .1. The Tacoma Narrows Failure and After. *Journal of Wind Engineering and Industrial Aerodynamics*, 40(3), 317-326.
- Zhao, M., Murphy, J. M., & Kwok, K. (2016). Numerical Simulation of Vortex-Induced Vibration of Two Rigidly Connected Cylinders in Side-by-Side and Tandem Arrangements Using RANS Model. *Journal of Fluids Engineering-Transactions of the Asme*, 138(2).
- Zhiyin, Y. (2015). Large-eddy simulation: Past, present and the future. *Chinese Journal of Aeronautics*, 28(1), 11-24.

APPENDIX B

List of Publications

W.K. Chin, Z.C. Ong, K.K. Kong, S.Y. Khoo, Y-H. Huang, W.T. Chong. (2017) Enhancement of Energy Harvesting Performance by a Coupled Bluff Splitter Body and PVEH Plate through Vortex Induced Vibration near Resonance. *Applied Science*. Published (appls-ci-208345)

W.K. Chin, Z.C. Ong, K.K. Kong, S.Y. Khoo, Y-H. Huang, W.T. Chong. (2017) Numerical Study on Bluff Splitter Body Aspect Ratio towards Amplification of Elastic Plate Vibration Induced by Vortex. *Acta Mechanica Sinica*. Under Review (ams2017-209).

W.K. Chin, Z.C. Ong, K.K. Kong, S.Y. Khoo, Y-H. Huang, W.T. Chong. (2017) Enhancement of Vortex Induced Vibration Effect on Elastic Plate with Different Edge Angle Bluff Splitter Bodies. *Science China Technological Sciences*. Under Review (SCTS-2017-0236).